Fall 12-21-2011

# Plasmon Enhanced Photoconduction in Porphyrin-Gold Nanoparticle Assemblies

David Conklin
*University of Pennsylvania*, conklind@seas.upenn.edu

## Recommended Citation

Conklin, David, "Plasmon Enhanced Photoconduction in Porphyrin-Gold Nanoparticle Assemblies" (2011). *Publicly Accessible Penn Dissertations*. 453.
http://repository.upenn.edu/edissertations/453

# Plasmon Enhanced Photoconduction in Porphyrin-Gold Nanoparticle Assemblies

**Abstract**

This thesis describes a series of experiments to both determine the origins of charge transport and enhanced photoconduction in metal nanoparticle arrays linked with zinc-porphyrin complexes, but to also determine the nucleation and growth mechanisms related to Ferroelectric Nanolithography (FNL) as a platform for hybrid devices. The development of test structures on glass substrates was undertaken to not only allow the study of the mechanisms controlling charge transport but the photoconduction of zinc-porphyrin linked gold nanoparticle (AuNP) arrays. In this study, the dominate charge transport mechanism was determined to be thermally assisted tunneling and the origins of enhanced photoconduction in these systems was attributed to three mechanisms: direct exciton formation in the molecules, hot electrons and a field effect (optical antenna) due to the excitation of surface plasmons. In the hope of developing a platform for hybrid devices, FNL was utilized to systematically vary the parameters that effect the deposition of metal nanoparticles through domain directed deposition on ferroelectric surfaces. The nucleation and growth mechanisms were determined through this work, where thevintegrated photon flux controlled the particle density and the interface between the particle and the ferroelectric surface determined the particles size. Finally, with the ability to control the deposition of AuNPs on a ferroelectric surface, hybrid devices of zinc-porphyrin linked AuNPs were realized with FNL.

**Degree Type**
Dissertation

**Degree Name**
Doctor of Philosophy (PhD)

**Graduate Group**
Materials Science & Engineering

**First Advisor**
Dawn A. Bonnell

**Keywords**
gold nanoparticles, porphyrin, ferroelectric, lithography, optoelectronic device

**Subject Categories**
Materials Science and Engineering

# PLASMON ENHANCED PHOTOCONDUCTION IN PORPHYRIN-GOLD NANOPARTICLE ASSEMBLIES

David J. Conklin

A Dissertation

In

Material Science & Engineering

Presented to the Faculties of the University of Pennsylvania

In Partial Fulfillment of the Requirements for the Degree of Doctor of Philosophy

2011

Dr. Dawn Bonnell, Trustee Professor of Material Science & Engineering
**Supervisor of Dissertation**

Dr. Russell Composto, Professor of Material Science & Engineering
**Graduate Group Chairperson**

**Dissertation Committee**
Dr. Jorge Santiago-Aviles, Associate Professor of Electrical & Systems Engineering
Dr. Ritesh Agarwal, Assistant Professor of Material Science & Engineering
Dr. Alan T. Johnson, Professor of Physics & Astronomy

## Acknowledgements

Trying to remember everybody and everything that has got me to this point seems like a daunting challenge, and this is only a very small subset of everyone and everything that has allowed me to success in this endeavor.

I would like to begin by expressing my gratitude to my advisor, Dawn A. Bonnell. She has been everything I could have wanted in an advisor and provided me with all the support and guidance I could have every wanted. Although I find it repetitious, I would also like to express my gratefulness to my parents. The love and support, through every step in my life, has set the bar very high for whatever the future holds for me. I love both of you very much. I would also like to thank all the friends and family that supported me through this, and especially Russell Messier who set me on the path I followed out of PSU and happy valley.

Of course when it comes to the actual work in this dissertation, (or any dissertation) it is due to all of the discussions, arguments, and late nights in the lab with labmates and friends. I would especially like to thank Maxim Nikiforov, Dongbo Li, Christopher Rankin, and Kendra Kathan. I would also like to thank all of the building staff that helped me and I became friends with from Jim Ferris and Doug Yates to Fred Hellmig, Patricia Overend, and Samantha Fellman.

And of course there have been all the friends that I have made through this, that have been a constant through all the ups and downs. The whole time here has been sprinkled with people that made me the person I became, from David Stein with whom we had one amazing ride while it lasted to Jamie Ford with some of the best advice anybody has

given me on the first day to Michael Hore who convinced me that you can go to the same place 4 times in one day. And there are the people I meant while in Philadelphia from Erin Crowe to Jessica Kim to Jon E. Rico. Thank you all soo much. And I want to also acknowledge the Princeton crew (if that is ok for a Penn dissertation). All the times I had with Greg Nieberg, Alex Kattamis, Patrick Murphy, Candice Tsay, and Nicole Leo have added so much to my life.

# ABSTRACT

## PLASMON ENHANCED PHOTOCONDUCTION IN PORPHYRIN-GOLD NANOPARTICLE ASSEMBLIES

David J. Conklin

Dr. Dawn A. Bonnell

This thesis describes a series of experiments to both determine the origins of charge transport and enhanced photoconduction in metal nanoparticle arrays linked with zinc-porphyrin complexes, but to also determine the nucleation and growth mechanisms related to Ferroelectric Nanolithography (FNL) as a platform for hybrid devices. The development of test structures on glass substrates was undertaken to not only allow the study of the mechanisms controlling charge transport but the photoconduction of zinc-porphyrin linked gold nanoparticle (AuNP) arrays. In this study, the dominate charge transport mechanism was determined to be thermally assisted tunneling and the origins of enhanced photoconduction in these systems was attributed to three mechanisms: direct exciton formation in the molecules, hot electrons and a field effect (optical antenna) due to the excitation of surface plasmons. In the hope of developing a platform for hybrid devices, FNL was utilized to systematically vary the parameters that effect the deposition of metal nanoparticles through domain directed deposition on ferroelectric surfaces. The nucleation and growth mechanisms were determined through this work, where the integrated photon flux controlled the particle density and the interface between the particle and the ferroelectric surface determined the particles size.  Finally, with the ability to control the deposition of AuNPs on a ferroelectric surface, hybrid devices of zinc-porphyrin linked AuNPs were realized with FNL.

## Table of Contents

# List of Tables

# List of Figures

conduction band, $E_f$ the Fermi energy, and $E_v$ the valence band. The surface of the solid is indicted by the perpendicular gray plane.

**Figure 2.23** – Schematic illustration of the crystal structure and associated band structure of PZT. The crystal structure on the left shows the atomic displacement in the ferroelectric tetragonal phase in which the octahedrally coordinated Ti/Zr is off center. The polarization induces charge at the surface causes band bending and the migration of electrons near the surface for use in photo-reduction reactions. The orientation of the polarization into the surface causes the bands to bend down at the surface, in which $E_c$ is the conduction band, $E_f$ the Fermi energy, and $E_v$ the valence band. The surface of the solid is indicted by the perpendicular gray plane.

**Figure 2.24** – The energy band diagram of PZT and $BaTiO_3$ compared to the reduction potential with respect to the standard hydrogen electrode of select metal salts.

**Figure 3.1** – Schematic illustration of the functionalization of a glass substrate with either (3-Aminopropyl)triethoxysilane, 3-aminopropyl(diethoxy)methylsilane or (3-Aminopropyl)trimethoxysilane in anhydrous toluene and the resulting deposition of citrate reduced gold nanoparticles (AuNPs).

**Figure 3.2** – Ferroelectric Nanolithography (a) a biased conductive SPM tip selectively reorients ferroelectric domains. (b) the relation of domain orientation direction and surface potential. (c) the topographic structure of lead zirconate titanate (PZT) surface

(left) is compared to the surface potential (right) after polarization patterning. (d) incident light creates electrons and holes in the PZT that is submerged in a metal salt solution and nanoparticles form on the positively polarized patterns. (e) patterns of metal nanoparticles made in the configuration of capacitance and resistance based devices and integrated into a device.

**Figure 3.3** – (a) Bare thin film substrate. (b) 50 µm thick molybdenum mask was place over the bare substrate to define the separation between the contact pads. (c) gold was evaporated over the whole surface. (d) the molybdenum mask was removed from the surface to reveal contact pads separated by 35µm or 70µm.

**Figure 3.4** – (a) Bare thin film substrate. (b) approximately 1µm of photoresist (Microposit S1813) was spun at 3000RPM for 30 seconds. (c) the sample was subsequently developed in developer (Microposit MF-319) for 30 seconds while agitating. (d) gold was evaporated over the whole surface. (e) the excess gold was lifted-off by placing the samples in acetone to reveal the predefined contact pad configuration. (f) using the contact pads produced in Figure3.4(e) as alignment markers, contact pads produced with a different photomask can be aligned to make contact to the AuNP assembly.

**Figure 3.5** – Gaussian peak fits to UV-Vis spectrum curves. The curves were fit to three, four, five, and six Gaussian peaks to compare the fit. Although the left most peak is used in the fitting process, it is just an artifact from the substrate. (a) fits 3 Gaussian peaks, (b)

fits 4 Gaussian peaks, with the fourth peak approximately placed at 430nm from examining the curve fit in (a). (c) fits five Gaussian peaks and give the best fit. A sixth Gaussian peak does not produce a better fit.

**Figure 4.1** – Synthesized citrate-stabilized AuNPs of (a) 16nm, (b) 32nm, & (c) 46 nm diameter.

**Figure 4.2** – Atomic force microscope (AFM) images of samples with immersion times of (a) 5, (b) 100, (c) 180, & (d) 200 minutes, respectively.

**Figure 4.3** – AFM images of the depositions of 15nm, 20nm, and 30nm commercially available AuNPs on glass substrates functionalized with APTES. The left column is immersion times of 100 minutes and the right column is 200minutes. (a) & (b) show depositions of 15nm diameter AuNPs with areal coverages of 44.1±2% and 77±4%, while (c) & (d) are 20nm with areal coverages of 56.5±2% and 71.8±3% , respectively. (e) & (f) are 30nm diameter AuNPs with areal coverages of 38.6±3% and 52.6±2%, respectively.

**Figure 4.4** – (a - d) show bi-modal depositions of 40nm AuNPs with 40nm, 30nm, 20nm, and 15nm diameter particles, respectively. The initial immersion time in 40nm AuNPs was for 180 minutes in all cases. The subsequent AuNP immersion times of 40nm, 30nm, 20nm, and 15nm diameters were for 25, 60, 15, 25 minutes, respectively.

Fowler-Nordheim tunneling showing a transition voltage of 1.17V ±0.06V. (b - d) show no transition to Fowler-Nordheim tunneling at higher voltages across all temperatures indicating only direct tunneling.

**Figure 4.10** – (a – d) show re-plots of the data in **Figure 4.8(a - d)** as $\ln(I/T^2)$ as a function of 1/kT, respectively. Thermionic emission can be distinguished by a region where $\ln(I/T^2)$ increases linearly with increasing temperature.

**Figure 4.11** – $d\ln(g^{-1})/dT^{-\alpha}$ as a function of temperature for $\alpha=1$, 0.8, and 0.5, of the conductivity data seen in **Figure 4.8(a – d)**, respectively. (a) & (b) have trimer molecules attached to the AuNP arrays and are best fit with $\alpha=1$ and $\alpha=0.88$. **(**c) & (d) represent AuNP arrays linked with dimers and monomers and best fit to $\alpha=1.0$ and $\alpha=0.5$, respectively. The best fit was determined by comparing the linear fit of the data below ~200K for each value of α. The α that resulted in the linear fit slope being closest to zero was defined as the best fit.

**Figure 4.12** – $d\ln(g^{-1})/dT^{-\alpha}$ is plotted for the best fit of α as a function of inverse temperature. (a) for various applied biases from the data in **Figure 4.8(a)**. (b) for trimer linked AuNP arrays that exhibit a linear conductivity response similar to that seen in **Figure 4.8(b)**. (c) & (d) for dimer and monomer linked AuNP arrays that exhibit a linear conductivity response similar to that seen in **Figure 4.8(c)** & **(d)**, respectively.

temperature dependent current enhancements at 1V and 2.5V, respectively. Red for illumination with 655nm, green with 533nm, and blue with 405nm laser diode. (c) & (d) are re-plotted as a function of photon flux per unit area for the 405nm, 533nm, and 655nm laser diodes. The inserts are corrected for the absorption coefficients obtain from the absorption spectra of the trimer molecule in Section 2.7.3 at the relevant wavelength for the photon flux.

**Figure 4.22 -** (a-d) Fowler-Nordheim plots of the conductivity data represented in **Figure 4.21**, for no illumination and illumination with red, green, and blue light, respectively. (a-d) exhibit transition voltages of 1.17V ±0.06V, 1.5V±0.02V, 1.26V±0.01V, and 1.26V±0.04V, respectively.

**Figure 4.23** - Temperature dependent conductivity data represented in **Figure4.21**, for no illumination and illumination with red, green & blue light. (a) & (b) show the conductivity data linearized to a thermionic emission model at 1V and 2.5V, respectively. (c) & (d) show the logarithm of the conductance as a function of inverse temperature (Arrhenius) at 1V and 2.5V, respectively.

**Figure 4.24** - dln(I)/dV as a function of voltage, where **(**a – f) represent the dln(I)/dV plots at 78, 118, 158, 198, 238, and 278K, respectively.

**Figure 4.25** – Optical absorption for the AuNP arrays before and after functionalization with dithiol-$PZn_3$. (a) is the UV-Vis spectra of the 16nm, 32nm, and 46nm samples in

**Figure 4.1(a-c)**, respectively. (b) is the UV-Vis spectra of only the 32nm sample, where the dotted line represents the AuNP's before attaching the dithiol-$PZn_3$ and the solid line denotes after linking the AuNP array, and the blue curve represents the absorption spectra of the dithiol-$PZn_3$ in solution. (c) & (d) are Gaussian peak fits of the 32nm sample before and after attaching the dithiol-$PZn_3$.

**Figure 4.26 –** Comparison of current enhancement for 4 different AuNP arrays linked with monomers that exhibit near-linear conductivity behavior. The figure show current enhancements at temperatures below the transition to metallic-like transport. The inserts show the current enhancements at room temperature, which exhibits metallic-like transport.

**Figure 4.27 –** Current enhancements represented in **Figure 4.26(a-d)**, respectively, as a function of photon flux at various temperatures. The inserts show the photon flux corrected for the absorption coefficient at the relevant wavelength.

**Figure 4.28 –** Logarithm of the conductance as a function of the inverse temperature of the data represented in **Figure 4.26(a-d)**, respectively. The inserts show dln(I)/dV of the data represented in **Figure 4.26(a-d)**, respectively, as a function of temperature.

**Figure 4.29 –** Comparison of the UV-Vis spectra for the AuNP arrays represented in **Figure 4.26**. The blue, dark cyan, black, and red lines are the UV-Vis spectra of the samples represented in **Figure 4.26 (a -d)**, respectively. The insert in the figure shows one of the Gaussian curve fits as described in Section 3.6.2.

# 1. Introduction & motivation

## 1.1. Introduction

Innovations during the last 50 years in micro- and nanotechnology have enabled advances in such diverse fields as integrated circuits, solar cells, photovoltaic cells, cancer treatment and telecommunications.[1-4] Each of these technologies has taken advantage of material properties that can be manipulated at the nano-scale, and in many cases, has reached the physical limits of these materials. Examples include the switch to high-k dielectric films from traditional oxides, such as HfO from $SiO_2$ in transistors and memory, and the integration of nanoparticles into devices to enhance absorption and/or conduction in photovoltaics.[5, 6] Many of these innovations have been focused on pushing the physical limits of traditional top-down fabrication.

One avenue for the development of next generation devices is to use bottom-up methods, such as block copolymers or self-assembled monolayers (SAM's), to take advantage of inherent material properties at a size scale that cannot be attained through top-down techniques.[7-9] The integration of biological systems in device fabrication is being explored to take advantage of the properties of molecules found in nature. Research in molecular electronics has intensified in the past few decades, focusing on electrical conduction in organic molecules modeled on biological systems to enable useful devices.[10-12] Conduction mechanisms and transport properties of single molecule junctions have been determined by characterization of molecules in various test structures, such as break junctions or by scanning probe microscopy (SPM) studies.[13-15]

One of the outstanding challenges is to combine self-assembly of dissimilar components with unique properties with lithographic patterning. Ferroelectric Nanolithography (FNL) offers the potential to assemble dissimilar components but the process to date has not demonstrated the ability to create multi-functional hybrid devices. Several outstanding fundamental issues are the control of nanoparticle size, separation, and density. Determination of the mechanisms controlling nucleation and growth of nanoparticles as a function of substrate orientation, texture, and optical power is necessary in order to develop a platform for multi-component nanostructures. Hybrid devices with multiple components raise issues of transport and photoconduction mechanisms that dominate the device performance. Transport in nanoparticle assemblies and molecular electronics has been shown to be complex and ambiguous in many cases.

The goal of this research is to develop a controlled process necessary to fabricate devices with FNL, determine the nanoparticle deposition mechanisms operating in FNL, and determine the transport mechanisms in molecular linked nanoparticle arrays. In order to address these issues, gold nanoparticle (AuNP) assemblies that vary particle size, spacing, density, and molecular linkers were fabricated and the voltage, temperature, and wavelength dependencies of the conductance were determined. From this, the dominate transport mechanisms, barriers to transport, and the origins of enhanced photoconduction were determined. Results from hybrid devices fabricated on two substrates were compared to determine the effects of the substrate on transport and photoconduction mechanisms. Hybrid devices on glass substrates were used to determine the transport mechanisms that dominate the porphyrin linked AuNP assemblies. Ferroelectric substrates were used to pattern AuNP arrays using ferroelectric nanolithography (FNL) to develop a platform for multi-component hybrid devices. In this case, the mechanisms controlling the nucleation and growth of NP's as a function of the ferroelectric domain orientation, crystallographic orientation, photon flux, optical power and electrolyte solution were determined. Hybrid devices were demonstrated based on fabrication with FNL.

The following chapter will summarize the current state of research and understanding of transport through metal and functionalized metal nanoparticle arrays, as well as the surface reactivity of ferroelectrics for photo-deposition of metal nanoparticles. Sections 2.1.2. and 2.1.3. will provide a survey of transport properties in similar systems that will provide insight into the possible mechanisms that may be influencing transport in these hybrid nanostructures, along with current interpretations of transport analyses. Section 2.1.4. will review the optical response of nanoparticle assemblies, followed by a summary of the influence of NP functionalization on the electrical and optical properties in Section 2.2. The potential of fabricating functional multi-component hybrid devices on ferroelectric surfaces will be reviewed in Section 2.3.

Chapter 3 will review the experimental procedures for fabrication and characterization of device structures on glass and ferroelectric substrates. The cleaning procedure, surface functionalization and AuNP synthesis will be reviewed for deposition of AuNP arrays on glass substrates, while patterning of ferroelectric domains inherent in FNL and the photoreduction of metal salts will be summarized. The various device test structures and configurations will be reviewed, along with the conditions for linking the AuNP arrays with zinc-porphyrin molecules. The rest of the chapter will summarize microscopy utilized to characterize the nanostructures, along with the optical & electrical characterization techniques used to determine the transport and photoconduction mechanisms.

Chapter 4 will discuss the properties of hybrid AuNP nanostructures on glass substrates. Transport mechanisms are determined by varying the AuNP size, spacing, distribution, and surface coverage along with varying the length of the molecular linker to analyze the voltage, temperature and wavelength dependent conductance. Comparisons of the dark conductivity with wavelength dependent conductivity allow the determination of the origins of the enhanced photoconduction and understanding a new phenomenon referred to as plasmon enhanced photoconduction.

Chapter 5 will present the kinetics of the photoreduction of AuNPs on a ferroelectric surface as a platform for hybrid multi-functional devices. Hybrid multi-component devices were developed by controlling the size, spacing, and density of metal nanoparticles on a ferroelectric surface employing FNL. Systematic variation of the domain orientation, crystal orientation, photon flux, optical power and electrolyte solution were used to determine the nucleation and growth mechanism of nanoparticles. AuNP arrays linked with various length porphyrin molecules created hybrid multi-component devices in which the transport mechanisms were determined by examining the voltage, temperature and wavelength dependent conductivity. This fabrication of a patterned hybrid nanostructure and demonstration of optoelectronic properties represents the first demonstration that ferroelectric lithography can be used to produce devices. Furthermore, this approach can now be generalized to an extensive array of device configurations utilizing organic as well as inorganic compounds, on thin films, single crystals, and polycrystalline substrates, producing a variety of molecule-nanoparticle combinations with unique and novel properties. And finally, Chapter 6 summarizes the major conclusions and outlines suggestions for extensions of this research.

# 2. Background principles: Previous research

## 2.1. Transport in metal nanoparticles arrays

### 2.1.1. Introduction

Metals have been exploited in numerous applications due to intrinsic properties such as high electrical and thermal conductivity, and the manipulation of noble metals has been of specific technological importance due to unique chemical and optical properties. Transport through nanoparticles, from highly ordered systems such as colloidal crystals to random arrays created by drop-casting on surfaces, has been shown to be complex and ambiguous.[16-18] Electronic systems such as granular metallic films and colloidal metal particle arrays can be model systems when trying to understand the transport mechanisms. The effects of disorder and quantum confinement contribute to the electronic properties, and can be quantified by fitting with tunneling conductance, charging energies, mean level spacing between particles and charge lifetimes.[19]

### 2.1.2. Transport mechanisms

In general, charge transport in metal nanoparticle arrays falls within three regimes: insulating in which there is weak coupling between electronic states, metallic in which classical theory of conduction dominates, and finally a transition regime in which the coupling is low due to large intraparticle separations. Granular metals and colloidal metal nanoparticle arrays can be used as model systems, in which conduction is a function of the intrinsic properties of the nanoparticles and the intraparticle coupling, which is a function of spacing between particles. The size and material of individual nanoparticles affects the transport within the particles and can be affected by charging and quantum confinement.[19] Within the array, the particle spacing, disorder, and charging can determine the effects on tunneling, hopping, varying wave function overlap, percolation effects and scattering.[18]

*Metallic regime*

When the particles are sufficiently large that quantum considerations can be neglected and the particles are highly coupled to each other, the films exhibit metallic behavior. At the theoretic limit, these films can be thought of as a bulk thin film and can be modeled by classical transport theory. According to the Drude theory of metals, the conductance of a metal follows the form of Equation (1), where *n* is the density of conduction electrons, *e* is the electron charge, τ is the mean free time, and *m* is the mass of a electron.[20]

$$\sigma = \frac{ne^2\tau}{m} \tag{1}$$

In disordered metals, the mean free time is related to the effects of scattering through the film and, hence, can be affected by either elastic or inelastic scattering events. The conductance, σ, can be re-written as Equation (2), where $\sigma_o$ represents elastic and σ(T) is the inelastic scattering.[18] Elastic scattering arises from impurities and defects and is independent of temperature, while inelastic scattering arises from electron-electron or electron-phonon interactions and has a logarithmic dependence on temperature.

$$(\sigma)^{-1} = (\sigma_0)^{-1} + (\sigma(T))^{-1} \tag{2}$$

At low temperatures the transport is dominated by elastic scattering since it is temperature independent, while inelastic scattering dominates the transport mechanism at high temperatures. The low temperature regime exhibits complex temperature dependence beyond the effects of inelastic scattering events. Investigations of granular metallic films have shown that structural dependent corrections, such as grain size and dimensionality, must be considered when modeling the transport at low temperatures.[19] Assuming that inelastic scattering increase with temperature, the metallic conductivity as a function of $1/k_BT$ decreases and the resistivity increases linearly with temperature.[18] These examples of conduction mechanisms and temperature corrections demonstrate the complexity in modeling real systems with competing charge transport processes.

### *Insulating regime*

In the insulating regime, in which the volume fraction of grains is small and hence weakly coupled, transport is more affected by disorder and other irregularities present in the system in contrast to the metallic regime. An important charge transport mechanism is tunneling, where tunneling enables charge to flow between weakly coupled sites. Tunneling is an elastic process (temperature independent) where the charge transport is a function of particle separation. Charge transport is mediated in weakly coupled metallic granular films by hopping from grain to grain. Weakly coupled periodic granular array can be modeled as a Mott insulator at low temperatures.[19] In this model, due to the energy associated with an electron leaving and entering adjacent grains, the transport is blocked at low temperatures by a Coulomb gap, $\Delta M$. At very small tunneling conductance, the gap is simply the Coulomb charging energy of the grain, $\Delta M = E_c$.[19]

This gap leads to an activation dependence (Arrhenius) of the conductivity as a function of temperature as seen in Equation (5), where the Mott gap is a function of the tunneling conductance between adjacent grains or particles.[19] The finite-temperature conductivity is due to electrons and holes present in the system, and results in the exponential dependence of the conductivity seen in Equation (5).

$$\sigma \propto e^{(-\Delta M/T)} \tag{5}$$

$$\sigma \sim \exp\left(-\sqrt{{T_0}/{T}}\right) \tag{6}$$

However, experimentally observed conductance deviates from this activation behavior at low temperatures and follows Equation (6), which resembles the Efros-Shkolovskii law derived for doped semiconductors as seen in **Figure 2.1**. [19] This phenomenon of non-Arrhenius behavior is observed in both granular and metal nanoparticle thin films and implies that disorder plays a crucial role in low-temperature conductivity in the insulating regime. This electrostatic disorder is unrelated to the grain size variation but is influenced by the charged defects in the insulating medium.

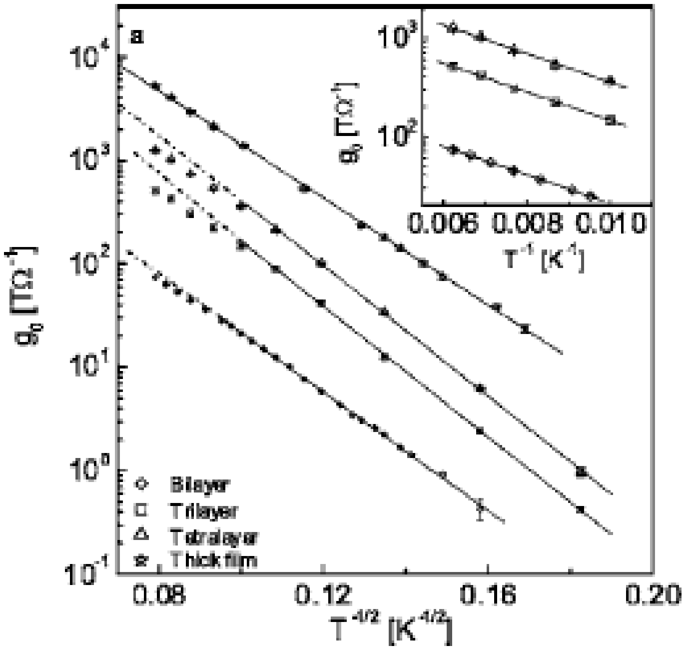

**Figure 2.1** – The inverse square root temperature dependence ($T^{-1/2}$) of the conductance ($g_0$) for periodic granular multilayers and thick films. The insert shows the high temperature range where the conductance ($g_0$)is re-plotted as a function of the inverse temperature ($T^{-1}$), indicating Arrhenius behavior.[19]

*Hopping conductivity*

Hopping involves a finite probability for tunneling to spatially remote states close to the Fermi level. Therefore, a hopping theory should consider the origin of a finite density of states near the Fermi level and a quantitative understanding of the mechanism of tunneling over long distances through a dense array of metallic grains or nanoparticles. Equations (5) and (6) usually imply a hopping mechanism, in which the model assumes that the charge carriers are localized but hop to adjacent sites via thermal energy.[19] Hopping is a complex transport mechanism that is a combination of tunneling probabilities between the nearest neighbor and the lowest energy state available.

Hopping to the closest available site is not always the most energetically favorable process since there is a greater probability that there is a lower energy site further away. This competes with the fact that there is a smaller probability of tunneling to the further site. The optimization of these two probabilities controls the transport characteristics.

The electrical properties of one, two, and three-dimensional (1D, 2D, and 3D) assemblies of metal nanoparticles functionalized with organic ligands have been extensively studied by dc and ac measurements.[21, 22] As in the previous section, a common feature at several tens of Kelvins below room temperature is the observation of an activated process, modeled by an Arrhenius-like relationship. The activation energy becomes temperature-dependent at lower temperature and, therefore, the conductivity follows a variable-range hopping model proposed by Mott seen in Equation (7).

$$\sigma(T) \sim \exp\left(^{-T_0}/_T\right)^{\gamma} \tag{7}$$

In this model $T_0$ is associated with the interparticle hopping energy and $\gamma=1/(X+1)$, where X is related to the dimensionality of the assembly. For 3D nanoparticle assemblies, a $\gamma=1/4$ might be expected but $\gamma=1/2$ is predominantly observed experimentally. The temperature range in which the transition from nearest-neighbor hopping to variable-range hopping appears, depends on the particle size and on the degree of disorder, reflecting the distribution in site energies of the individual nanoparticles in the assemble.[21] Studies have also shown intermediate values for the temperature dependence, in which neither $\gamma=1$ or $\gamma=1/2$ provides an adequate description of the conductance. Values of $\gamma$ between 0.67 and 0.84 have been found in gold nanoparticle arrays functionalized with alkanedithiol linkers.[23, 24] Furthermore, it has been observed that the temperature dependence varies with the size of the nanoparticles, but little variation with the linker length is found.[23]

These somewhat idealized model systems demonstrate that the transport mechanisms in these systems are complex and careful analysis is required to understand the competing mechanisms contributing to the overall conductance. The transition between highly coupled, metallic films and weakly coupled insulating films, generally referred to as the metal-insulator transition (MIT) regime, is where competing charge transport mechanisms can occur with interesting electrical characteristics that are not fully understood. Within this regime, the competing processes translate into, not only temperature dependences, but applied electric field and disorder parameter dependences. An example of this is the percolation effects on generally disordered metal nanoparticle assemblies. NP assemblies must cross a percolation threshold to exhibit overall metallic conduction. Although at or above the transition, the NP assemblies may be dominated by nonmetallic conduction mechanisms, as the number of pathways increases, the nonmetallic pathways become less dominate. Dhirani and others have studied the transport and optical properties of random arrays of gold nanoparticle films.[18, 24-30] **Figure 2.2** shows temperature dependent conductivity as a function of the number of AuNP layers on a glass substrate.[28] The figure shows a transition in the transport mechanism from a thermally activated regime to metallic behavior as a function of the number of AuNP layers, which is consistent with percolation-driven MIT..

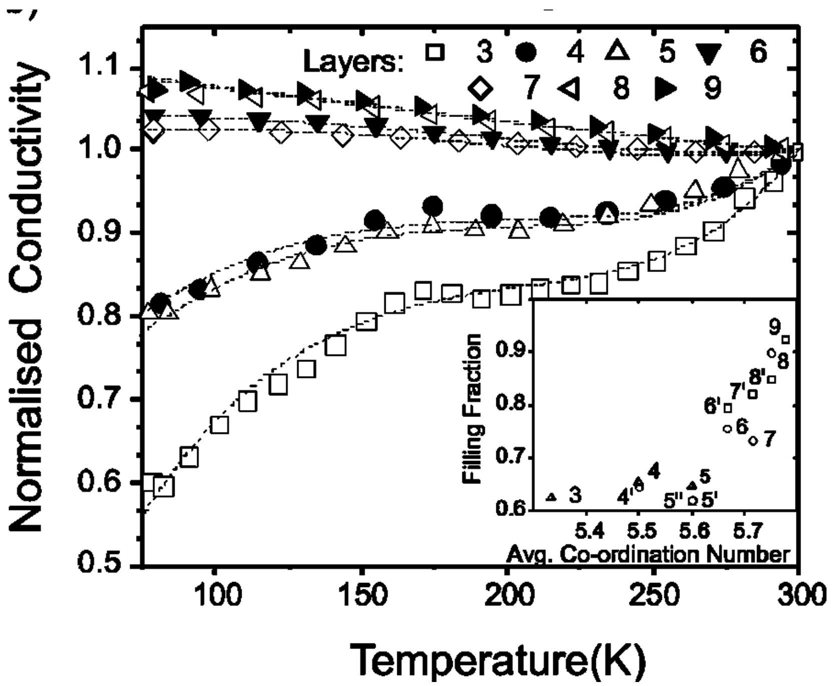

**Figure 2.2** – The temperature dependence of the normalized conductivity for 1,4-butanedithiolate-linked AuNP multilayer films with 3-9 layers. The dashed lines are fits to an effective-medium approximation model.[18]

**Figure 2.2** shows that the percolation threshold in this system is not reached until after the addition of the 6th AuNP layer. This system was modeled using an effective medium approximation, where the solution of Equation (8) provides the effective conductance of the system, where $g_{eff}$ is the effective conductance, $g_{\alpha}$ is the conductance of each individual particle, and $f(g_{\propto}, p)$ is a probability distribution, described in Equation (9).[28]

$$\sum_{\propto} \frac{f(g_{\propto}, p)(g_{eff} - g_{\propto})}{g_{\propto} + g_{eff}(^{z}/_{2} - 1)} = 0 \tag{8}$$

$$f(g_{\propto}, p) = p^2 g_m + 2p(1-p)g_t + (1-p)^2 g_i \tag{9}$$

Equation (9) represents the probability, p, that the bonding between the particles is; metallic, $g_m$, tunneling, $g_t$, or insulating, $g_i$. This is an analogous model to Kirchoff's Law for ordered networks of random valued conductances and demonstrates the competing charge transport mechanisms and percolation phenomena. As the discussion above demonstrates, these systems exhibit multiple transport mechanisms that require careful analysis, but these studies also show the potential of these systems to have tunable properties with novel transport properties.

### 2.1.3. Analysis of charge transport

The dominant charge transport mechanism in metal nanoparticle assemblies is complex and ambiguous in most cases. Analysis of charge transport has been investigated in other systems, such as wide-bandgap semiconductors and nearly insulating materials. These studies provide a template for charge transport analysis in materials that exhibit low conductivities and high disorder. Difficulties in interpretation arise from the large number of unknown parameters required to model the transport data. The effective contact area, dielectric structure between the particles, and electron mobility are all variables that need to be approximated but many of them are unknown. Here we will consider direct tunneling, along with field and thermionic emission models to understand the functional form for the charge transport. A review of the general forms of the transport models will be given, while comparing the voltage and temperature dependencies that can determine the potential barrier height.

A direct tunneling model based on the physical geometry of the system can be used to obtain a description of the barrier to transport. To first order, the conduction can be modeled by a semi-classical approximation, where quantum effects are incorporated into a classical framework. Applying the Wentzel-Kramers-Brillouin (WKB) approximation to a rectangular barrier at low bias results in an analytical expression that requires an understanding of the emission area, *A*, barrier width, *d*, and the barrier height, Φ. The tunneling current equation can be reduced (by using Simmons approximation) to Equation (10), where $k_1$ and $k_2$ are constants , $X=\sqrt{\Phi - \frac{V}{2}}$ ,and $Y=\sqrt{\Phi + \frac{V}{2}}$ .[31]

$$I = \frac{k_1 A}{d^2}\left[X^2 \exp(-k_2 dX) - Y^2 \exp(-k_2 dY)\right] \tag{10}$$

The model assumes that the potential is spatially averaged and varies linearly with space and applied bias. Unfortunately, applying this model requires accurate knowledge of both the cross-sectional tunneling area and the gap separation. The number of unknown variables needed to fit the transport data to the tunneling model makes it almost impossible to extract meaningful barrier height in disordered media.

Another method for estimating the barrier height in the framework of a tunneling model involves plotting the conductance in a Fowler-Nordheim plot.[32] This analysis is based on a transition from direct tunneling to field emission, where the rectangular potential barrier at low applied bias becomes triangular at higher biases.  The direct tunneling regime at low biases is described by logarithmic growth of ln(I/V$^2$) as a function of 1/V. In Fowler-Nordheim tunneling (field emission), in which the applied bias exceeds the barrier height, the logarithmic growth transitions to a negative linear relation of ln(I/V$^2$) as a function of 1/V.  The advantage of this approach is that the barrier height is extracted directly from the plot and therefore does not require approximation of the fit parameters. Equation (11) describes Fowler-Nordheim tunneling, where $I$ is the current, E is the applied electric field, $m^*$ is the effective mass, $q$ is the electron charge, and Φ is the barrier height.

$$I \propto E^2 \exp\left(-\frac{4\sqrt{2m^*}(q\emptyset)^{3/2}}{3qhE}\right) \tag{11}$$

A linear fit of the data in the high bias regime of a Fowler-Nordheim plot, related to field emission, allows the barrier height to be extracted from the slope.  Equation (12) shows the barrier height as a function of the slope of the linear fit of the data, where Φ is the barrier height, $q$ is the electron charge, $m^*$ is the effective mass, $d$ is the barrier width and $b$ is the slope of the linear fit in the high bias regime.

$$\emptyset = \frac{1}{q}\left(\frac{3q\hbar b}{4d\sqrt{2m^*}}\right)^{2/3} \tag{12}$$

Noting that direct tunneling and Fowler-Nordheim (field emission) have nominal temperature dependence, the possibility that electrons are thermally excited over the barrier instead of tunneling directly through the potential barrier is examined. The temperature dependence of a thermionic emission (Schottky) model is seen in Equation (13), where T is the temperature, $A$ is the tunneling emission area, $A^{**}$ is the effective Richardson constant and ϕ is the barrier height.

$$\mathrm{I} \propto AA^{**}T^2 \exp\left(-\frac{q}{kT}\left(\phi - \sqrt{E}\right)\right) \tag{13}$$

Plotting the data as $\ln(\mathrm{I}/\mathrm{T}^2)$ as a function of 1/T allows the barrier height to be determined by obtaining the slope through a linear fit of the data Unfortunately, the thermionic emission current model does not take into account other conduction mechanisms that could be contributing simultaneously. For example, thermally-assisted tunneling could contribute, where electrons are excited toward the top of the potential barrier which may be thinner allowing those electrons to tunnel through more easily. As a result, the distinction between tunneling conduction from thermionic emission is not well-defined for small gap separations.

The following section summarizes the functional forms in the case where there is a limited barrier to transport through the functionalized AuNPs. The electronic transport mechanisms can be limited to temperature-independent charge transport models, such as Fowler-Nordheim tunneling, and temperature-dependent models, such as thermionic emission, low-field migration, Poole-Frenkel hopping, and thermally assisted tunneling.

The functional forms of these transport mechanisms are seen in Equations (14)-(18), respectively, where E is the applied electric field, $E_i^O$ is the trap ionization energy, *e* is the electron charge, *k* is the Boltzmann constant, $\varepsilon$ is the dielectric constant, $\varepsilon_0$ is the permittivity of vacuum, $\phi_B$ is the barrier height, $\mu$ is the electron mobility, $A_{eff}$ is the effective transport area, *h* is Planck's constant, *m* is the effective mass, and t & $\Theta$ are elliptical functions.

$$I = A_{eff} \frac{e^3 m}{8\pi h m \emptyset_B} E^2 \exp\left(-\frac{8\pi\sqrt{2m}}{3he}\frac{\emptyset_B^{\frac{3}{2}}}{E}\right) \tag{14}$$

$$I = A_{eff} A^{**} T^2 \exp\left(-\frac{e}{kT}\left(\emptyset_B - \sqrt{\frac{eE}{4\pi\varepsilon_0\varepsilon}}\right)\right) \tag{15}$$

$$I = e\mu n E \exp\left(-\frac{E_f}{kT}\right) \tag{16}$$

$$I = e\mu n E \exp\left(-\frac{e}{kT}\left(E_i^0 - \sqrt{\frac{eF}{4\pi\varepsilon_0\varepsilon}}\right)\right) \tag{17}$$

$$I = \frac{E}{2\pi}\left(\frac{kTt}{2\pi}\right)^{1/2} exp\left(-\frac{\emptyset}{kT} + \frac{E^2\Theta}{24(kT)^3}\right) \tag{18}$$

In most analyses (Section 2.1.2.), the I-V plots are linearized to the normalized coordinates that correspond to the respective mechanisms. But with systems with multiple transport mechanisms in various regimes, the conventional analysis is ambiguous regarding the dominate conduction mechanism when fitting either the bias-dependent and/or temperature-dependent conductance data. This issue can be addressed by using current-normalized differential conductance, which simplifies the transport equations to provide a more rigorous examination of competing mechanisms.[33] The advantages of this analysis is that dln(I)/dV is independent, as seen in Equations (19)-(23), of many of the unknown variables present in the transport equations above.

$$\frac{dlnI}{dV} = \frac{1}{V} + \frac{4\pi}{3he}\sqrt{2m}\frac{\emptyset_B^{3/2}}{(V)^2} \tag{19}$$

$$\frac{dlnI}{dV} = \frac{e}{4kT}\left(\frac{e}{\pi\varepsilon_0\varepsilon}\right)^{\frac{1}{2}}(V)^{-1/2} \tag{20}$$

$$\frac{dlnI}{dE} = E^{-1} \tag{21}$$

$$\frac{dlnI}{dE} = \frac{1}{E} + \frac{1}{kT}\sqrt{\frac{e^3}{4\pi\varepsilon_0\varepsilon}}E^{-0.5} \tag{22}$$

$$\frac{dlnI}{dE} = E^{-1} + \left(\frac{E\Theta}{12(kT)^3}\right) \tag{23}$$

The bias and temperature-dependences of dln(I)/dV provide a robust analysis of transport mechanisms, especially when trying to fit trends where multiple conductance mechanisms exist and are transitions from one regime to another.

The discussion above has shown that different models are required to describe the conduction mechanism dominating each device. While the inherent complexities of the presence of multiple transport mechanisms in these systems presents issues in determining the specific dominate mechanism controlling transport, it also allows the opportunity for complex device structures and the ability to create multi-functional platforms.

### 2.1.4. Optical properties

The optical properties of noble metals have been exploited for hundreds of years. These properties can be observed in paints with gold nanoparticles that produce a different color in transmission and reflection or using various sized gold nanoparticles in solution to vary the color from red to violet.[34, 35] The plasmon frequency of most metals lies in the UV, but noble metals d-d electronic bands provide the optical transition levels that correspond to the visible region. As the size of the nanoparticle becomes comparable to the wavelength of the incident light, the light can interact with the particle. The surface plasmon resonance in metal nanoparticles is the coherent excitation of the conduction electrons which leads to an in-phase oscillation, as illustrated in **Figure 2.3.**[35]

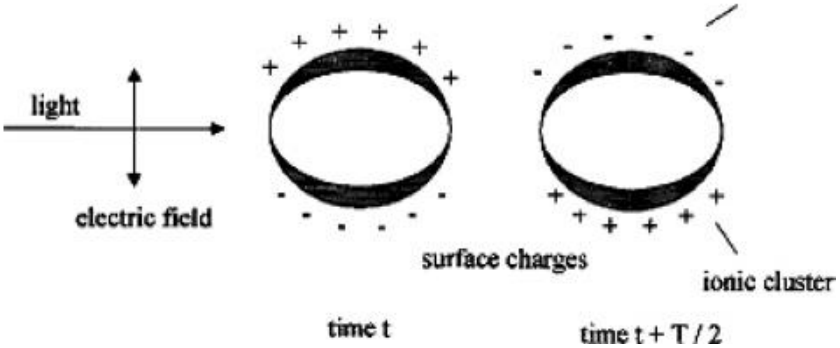

**Figure 2.3** – Schematic presentation of the function of surface plasmons in metallic nanoparticles due to the interaction of electromagnetic radiation with the metal sphere. A dipole is induced, which oscillates in phase with the electric field of the incident light. [35]

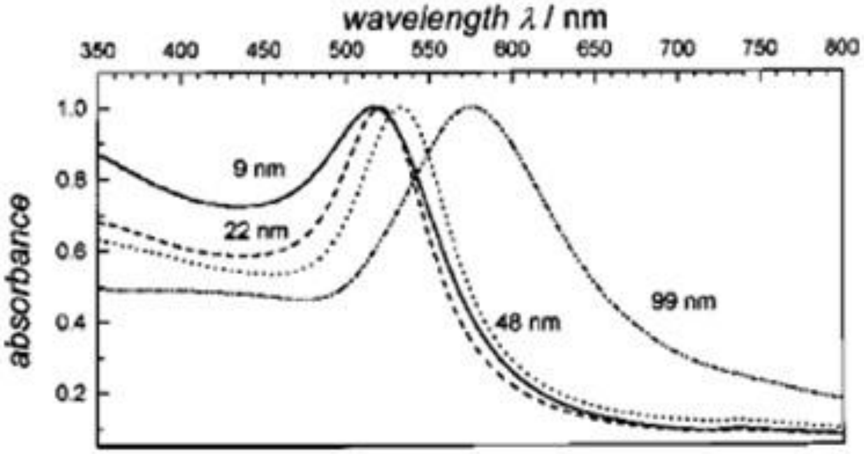

**Figure 2.4** – Experimentally measured surface plasmon resonances of 22, 48, and 99nm spherical gold nanoparticles.[18]

The effect of size on the surface plasmon resonance can be seen in the absorption spectra of **Figure 2.4**.[35] The plasmon resonance is not only a function of the size of the nanoparticle, but the shape, composition, crystallinity, and structure, all of which affect the optical properties. Mie theory has been used to describe the optical properties of metal nanoparticles using a dipole approximation. This approximation describes the extinction cross-section of a single metal nanoparticle, which is a function of the energy loss in the particle due to absorption and scattering. The extinction cross-section is described by the dielectric function of the metal and a resonance condition occurs when Equation (24) is minimized, which occurs when $\varepsilon_m = -2\varepsilon_s$., where $\varepsilon_1$, $\varepsilon_2$, $\varepsilon_m$,and $\varepsilon_m$ are the dielectric constants of the real component, the imaginary component, and the medium, respectively, and ω is frequency.[35]

$$[\varepsilon_1(\omega) + 2\varepsilon_m]^2 + [\varepsilon_2(\omega)]^2 = minimum \qquad (24)$$

The dipole approximation of Mie theory models the absorption spectra of small nanoparticles very well, but there are limitations. As the particle size increases, the dipole approximation is no longer valid since the incident light cannot be assumed to homogeneously polarize the nanoparticles and higher order modes must now be considered. This can be seen in **Figure 2.4** where, as the particle size increases, the absorption peak shifts to higher wavelengths and broadens due to the presence of higher order modes at lower energies.[35] Another effect on the plasmon resonance that is clear from inspection of Equation (24) is that the wavelength is also dependent on the surrounding medium.

As has been shown above, the peak shape, size and position are a function of the dielectric properties of metal and the surrounding media. Modeling these systems is based on assumptions that the particles are in the dilute regime, hence non-interacting, and that the medium is homogeneous. While nanoparticles in this regime can be described by the intrinsic properties of the metal nanoparticles, as the system deviates from these assumptions, the aggregated nanoparticles are characterized by the correlation length of the spatial order, filling factor, and structure. Densely packed nanoparticle assemblies affect the absorption spectrum and can be modeled by an effective-medium theory. Ghosh et al theoretically modeled the optical spectra dependence on the size, spacing, and aggregate size of nanoparticle assemblies.[35] **Figure 2.5** shows that size variation, while the spacing of the nanoparticles is kept constant, shifts and splits the absorption spectra.[35] As the particle size increases, the dipole approximation is no longer valid and a second longitudal peak is observed. In the case that the particles are kept the same size but the spacing is varied, as seen in **Figure 2.6**, when the particles have 0nm spacing, the particles act like a single metal nanoparticle of twice the size.[35] But as the spacing increases, the surface plasmon peaks shift until the spectrum is that of isolated metal nanoparticles expected in the dilute regime. The optical spectra are not only dependent on size and spacing, but the number of particles that agglomerate together. **Figure 2.7** models the absorbance as a function of the aggregate size and shows the peak shift to lower energies as the number of aggregate nanoparticles increases.[35]

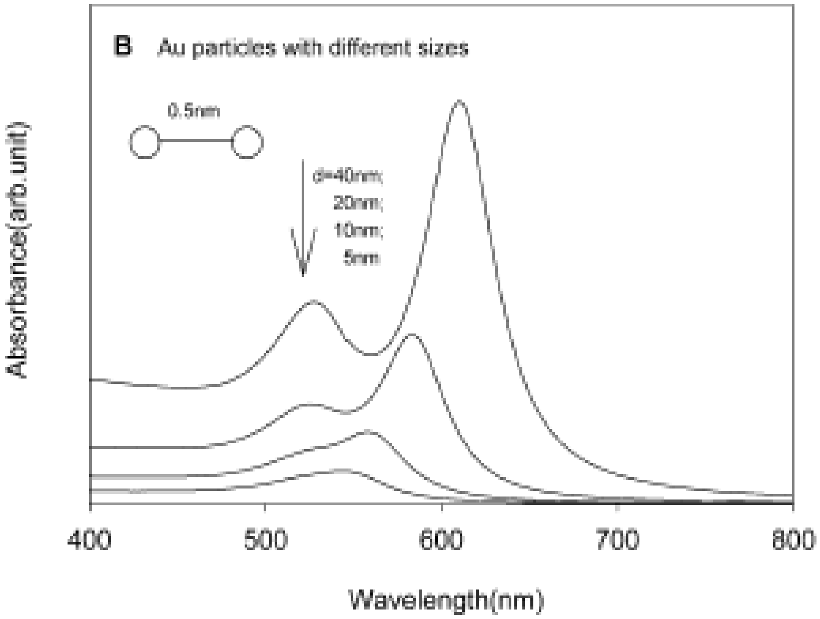

**Figure 2.5** – Electrodynamic modeling calculations for Au nanoparticles. Influence of gold nanoparticle diameter (d) on the extinction spectra at fixed (0.5nm) interparticle diameter.[18]

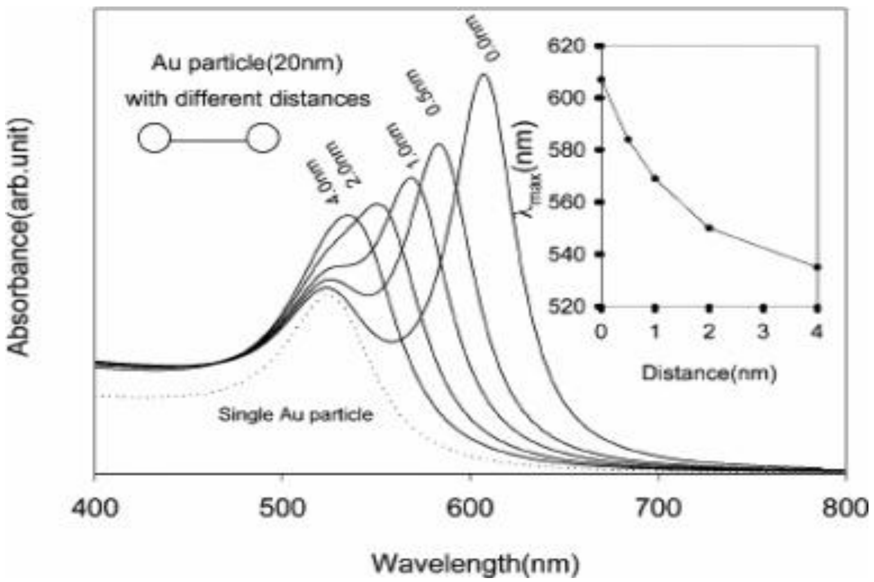

**Figure 2.6** – Electrodynamic modeling calculations for gold nanoparticles. Change of extinction spectra for 20nm diameter particles with interparticle distance (s). The insert is the peak shift as a function of interparticle distance.[18]

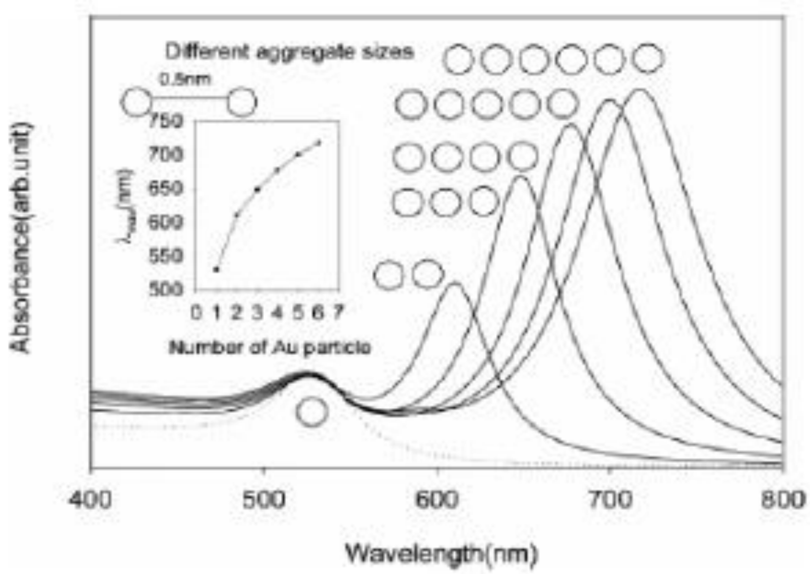

**Figure 2.7** – Electrodynamic modeling calculations for gold nanoparticles. Extinction spectra of "line aggregates" of varying number (d=40nm, s=0.5nm). The insert is the peak shift as a function of the number of gold particles in the line aggregate.[18]

A diverse range of collective behavior can be obtained by adjusting the spatial arrangement of the nanoparticles as well as the intrinsic properties of the individual nanoparticles. While **Figures 2.5-2.7** model the coupling of individual particles or the linear aggregation of nanoparticles, other studies have shown that the transition behavior from isolated to collective modes in nanoparticle assemblies has a strong relationship on the size and position of the individual nanoparticle within the collective.[36] The role of individual nanoparticles has been studied through plasmonic oligomers, where precise control of the size, spacing, and number of particles can be achieved through nanofabrication. Hentschel et al have shown in **Figure 2.8** that large spectral shifts can be obtained through not only the configuration of the nanoparticles as seen in the left panel, but by displacing an individual nanoparticle in the assembly, as in the center panel. These reveal how individual nanoparticles effect on the collective response and the size of the resulting spectral shift.[36]

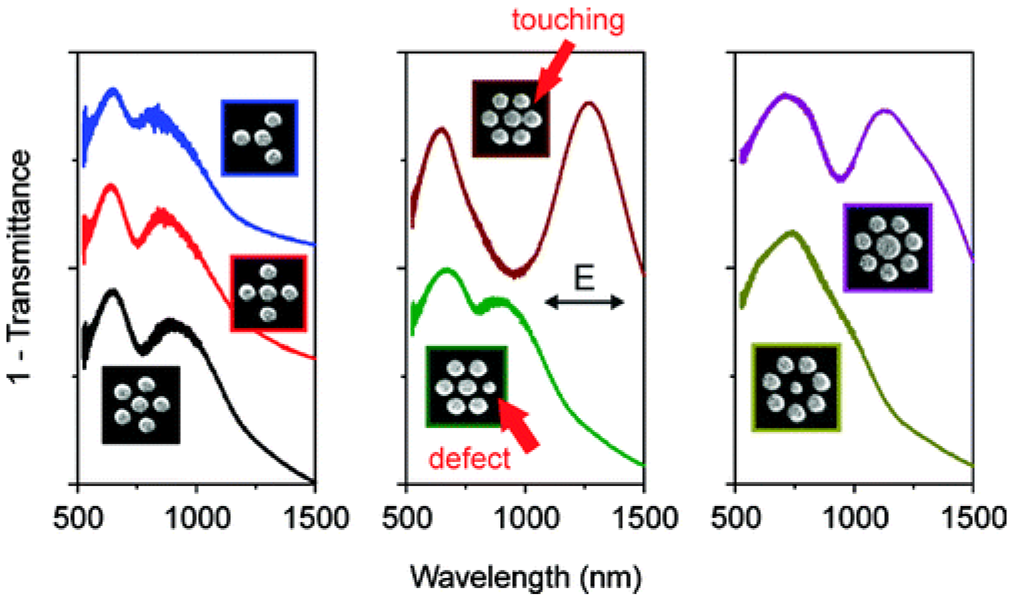

**Figure 2.8** – The effect of particle configuration and separation on the plasmonic properties. Both the constitution and configuration of plasmonic oligomers have a large influence on their resonant behavior.[36]

Whereas the discussion has been limited to investigating near-spherical particles and a homogenous medium, the shape and medium on which the particles interact is just as important.  Studies have shown that the substrate dielectric constant can have an effect on the absorption spectrum.[37, 38]  **Figure 2.9** shows how the optical response of silver nanoparticles is affected by the shape of the nanoparticle.[37]  The surface plasmon resonance (SPR) shifts from the protypical optical response for spherical particles represented by the purple curve to the complex optical response from a cubic nanoparticle represented by the black curve in **Figure 2.9**.

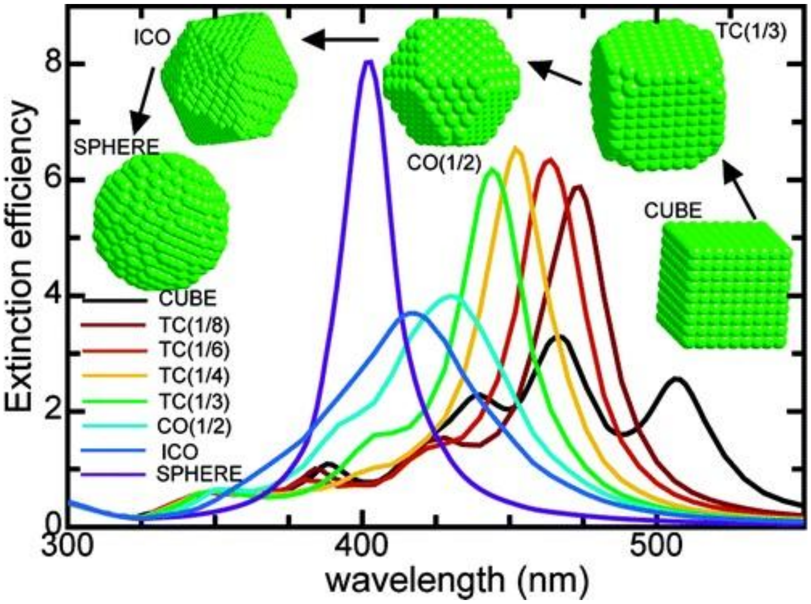

**Figure 2.9** – The incident wavelength dependence of the extinction efficiencies on a silver cube, different truncated cubes, and a spherical nanoparticle.[37]

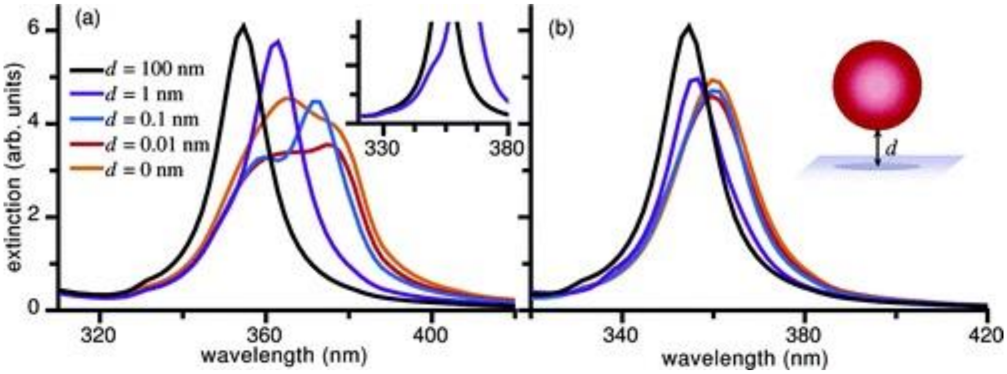

**Figure 2.10** – Extinction efficiency of silver spherical NPs located above the substrate by a distance d, for an external field (a) normal and (b) parallel to the substrate.[37]

**Figure 2.10** shows the effect on the optical response as a function of the distance of the nanoparticle above the substrate. As the nanoparticle is brought from 100nm above the surface to the surface, the optical absorption broadens and red shifts for both the normal (left panel) and parallel (right panel) applied electric field to the substrate.

As can be seen from the discussion above, the mechanisms and characterization of these systems are complex and not completely understood. There is much to be done to understand the mechanisms controlling charge transport and optical absorption, but there are also great opportunities to manipulate and exploit these unique phenomena for device applications.

## 2.2. Molecular electronics

### 2.2.1. Introduction

Interesting and unique opportunities arise from developing a platform for the assembly of multi-component systems with the ability to integrate organic compounds with an enhanced and diverse property set. The ability to assemble metal nanoparticles is not only interesting as a template for devices, but as a possible platform for understanding the processes that nature provides in light absorption and harvesting, and reproduce those effects using synthetic molecules.  The previous section summarized the complex relationship between the size, array disorder, and dielectric constants which affected the transport mechanisms and optical responses of AuNP arrays.  The insertion of electrical and optically active molecules into metal nanoparticle arrays has been shown to result in novel and/or enhanced device properties.[39, 40]  Recent studies have explored the relationship between the molecular linker length, bonding, effective dielectric constant, degree of conjugation, and absorption cross-section on transport properties and photoconduction.[21, 41, 42]  Conductivity studies on single molecule, self-assembled monolayers (SAMs), and metal nanoparticle assemblies have provided a wealth of information on the transport mechanisms through various molecular junctions and the effects of bonding and length.  The results have been obtained from scanning tunneling microscopy (STM), scanning tunneling spectroscopy (STS) and the fabrication of various electrode devices including break junctions and layered structures.

### 2.2.2. Transport through functional molecules

Understanding transport mechanisms in organic molecules is of interest due to their potential applications in nanometer scale electronics.  One of the molecular systems that have been extensively studied is alkanethiol due to the formation of robust SAMs on gold surfaces.  The conduction properties of these materials can be chemically tuned by means of bifunctional spacer molecules with defined lengths.  Studies have shown that if the particle size is kept constant and only the particle spacing is increased by the spacer molecule, that the activation energy increases linearly with increasing linker length.[21] This relationship is valid as long as the spacer molecule is not covalently bound to the particle and the molecular orbitals are not delocalized. If the linker molecule is covalently bound with delocalized π-electrons, the activation energy decreases depending on the electronic structure and length of the molecule.[21] These results reflect that the charge transport is dependent on the particle size, spacing and the electronic structure of the functionalizing molecule. Temperature-dependent conductivity measurements have shown temperature-independent electron transport, implying that tunneling is the dominant conduction mechanism through alkanethiols.[41] These systems also exhibit an exponential dependence of tunneling current on the molecular length.[41] Although the electrically insulting nature of σ-bonded alkanethiols make an excellent structure for exploring the transport through nanoparticle arrays and use as a spacer molecule, there are other classes of molecular wires that are of greater interest for device applications.

Organic π-conjugated oligomers have been studied for use as molecular-scale interconnects for reasons of diversity and chemical tunability. Two classes of molecular wires oligo(phenylene ethynylene) (OPE) and oligo(phenylene vinylene) (OPV) have been of great interest. The π-conjugation along the molecular backbones of these molecules produces enhanced electron and hole transport along the molecular length. Transport studies to determine the relative barrier heights in the electronic junction have shown that the barrier height is a function of the molecular length in these systems.[32] In contrast to alkanes, the HOMO-LUMO gap of π-conjugated molecules is known to decrease with increasing conjugation length.[43] The effective barrier height is constant across the alkane molecules and decreases with the extent of the electron delocalization across the π-conjugated molecules.[32] The bond-length alternation also has been shown to play an important role in determining the conductance of molecular wires. [39] Charge transport across organic molecules as a function of molecular structure and the degree of bond-length alternation needs to be considered to fully understand the differences in charge transport across π-conjugated molecular wires. Other work has shown that inelastic processes and heat dissipation play a role in controlling charge transport through molecular junctions.[42]

### 2.2.3. Photoconduction mechanisms

In traditional photoconductors, the incident light generates mobile charge carriers, which in turn cause an increase in conductivity. Spatial resolution at the atomic scale has been achieved in the coupling of light to single molecules absorbed on a surface. Electron transfer to a single molecule induced by green to near-infrared light in the junction of a STM exhibited spatially varying probability that is confined within the molecule.[44] The mechanism involves photo-induced resonant tunneling in which a photoexcited electron in the STM tip is transferred to the molecule.[44]

Photoconductive gain effects observed in 2-D arrays of gold nanoparticles in which alkane molecules are inserted are strongly enhanced at the frequency of the surface plasmon resonance.[40] It has also been reported that the conductivity can either increase or decrease on irradiation with visible light of wavelengths close to the particles surface plasmon resonance. The sign of the conductivity change and the nature of the electron transport between the nanoparticles depends on the molecules comprising the self-assembled monolayers stabilizing the nanoparticles.[45] SAMs with electrically neutral molecules exhibit an increase in conductivity upon illumination. On the other hand, SAMs containing electrically charged groups exhibit a decrease in conductivity. The observations can be understood in terms of light-induced creation of mobile charge carriers whose transport through the charged SAM is inhibited by carrier trapping in transient polaron-like states.[45]

### 2.2.4. Zinc-porphyrin complexes

Another class of molecular wires, zinc porphyrin-based systems, has been studied due to high charge mobilities along the molecule. Porphyrin complexes are found in a variety of natural systems from heme in red blood cells to chlorophyl in plants. These types of complexes are found in nature and are responsible for light harvesting and energy conversion. The general theory of chemical synthesis of porphyrin complexes is discussed at great length in other sources and, hence, will not be discussed in depth here.[46] A wide variety of porphyrin complexes exist but the basic structure consists of four modified pyrrole rings connected by methane bridges. Porphyrins are aromatic, heterocyclic macrocycles, which typically have intense absorption maximum in the visible regime. The absorption properties can be controlled by the insertion of a metal ion to complex to the macromolecule. Zn based porphyrins will be the specific class of molecules that is the focus in this work. Other studies of these molecules have found that the charge transport mechanism in these systems can be described by small polaron hopping.[47] The transport along the molecular wire is extremely sensitive to disorder (within the wire and in its environment). [47]

### 2.2.5. Structure & absorbance

These molecules were synthesized by the Therien group to have very specific physical, electrical and optical properties that make them interesting for possible light harvesting applications[46, 48-53]. **Figures 2.11 - 2.14** show the structure of various α-ω dithiol-terminated meso-ethynebridged porphyrin supermolecules. The length of the monomer, dimer, trimer, and tetramer are 2.15nm, 2.41nm, 4.59nm, and 5.68nm, respectively. These molecules were chosen for the substantial polaron delocalization lengths, impressive dark conductivities, and unusually large polarizabilities.[50] These molecules also have thiol complexes at both ends to provide a linkage to gold.

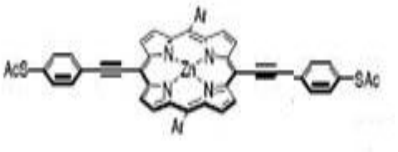

**Figure 2.11** - α-ω dithiol-terminated meso-ethynebridged (porphinato)zinc(II) oligomer supermolecule consisting of one porphyrin ring. The monomer complex has a total length of 2.15nm from the ends of thiol groups.[50]

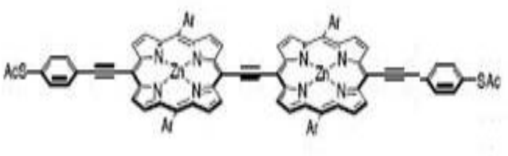

**Figure 2.12** - α-ω dithiol-terminated meso-ethynebridged (porphinato)zinc(II) oligomer supermolecule consisting of two porphyrin rings. The dimer complex has a total length of 2.41nm from the ends of thiol groups.[50]

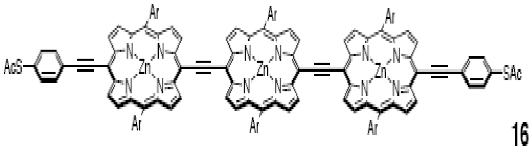

16

**Figure 2.13** - α-ω dithiol-terminated meso-ethynebridged (porphinato)zinc(II) oligomer supermolecule consisting of three porphyrin rings. The trimer complex has a total length of 4.59nm from the ends of thiol groups. [50]

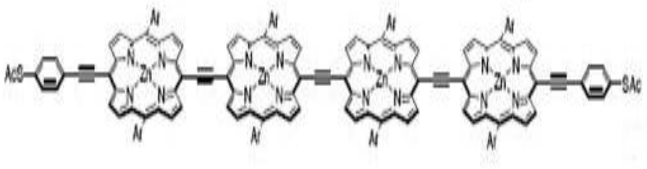

**Figure 2.14** - α-ω dithiol-terminated meso-ethynebridged (porphinato)zinc(II) oligomer supermolecule consisting of four porphyrin rings. The tetramer complex has a total length of 5.68nm from the ends of thiol groups.[50]

These molecules were also selected because of the structures low-energy, high-oscillator strength π-π* absorptions polarized along the length of molecular axis. This results in large absorption cross-section in the visible range, as seen in **Figure 2.15**. **Figure 2.15** shows the absorption spectra for the monomer, dimer, trimer, and tetramer in solution. The unique features seen in **Figure 2.15** are the absorption band edge at approximately 400nm, and the splitting of the absorption peak with addition of porphyrin rings.

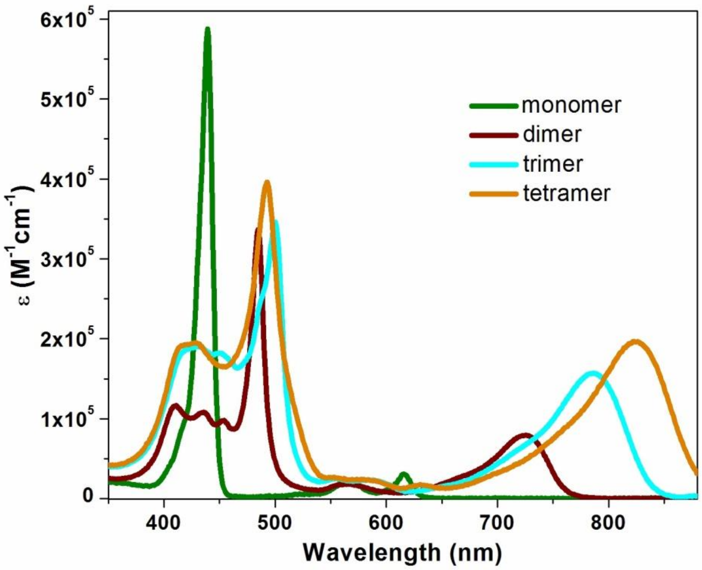

**Figure 2.15** – Room-temperature electronic absorption spectra of monomer, dimer, trimer, and tetramer α-ω dithiol-terminated meso-ethynebridged (porphinato)zinc(II) oligomer supermolecules.[54]

It is also notable that in the IR, the addition of porphyrin rings to the chain pushed the absorption peak at 700nm deeper into the IR. Although the excitation in the near-UV excites electrons to a higher excited state, the lifetimes of these states are in the femto second range, whereas the lowest excited state, to which all wavelengths relax, has an excited state lifetime in the nanosecond range. These porphyrin complexes provide a novel linker group to vary the optical properties of the nanoparticle assemblies in hopes to create a hybrid structure with enhanced opto-electrical properties for device applications.

## 2.3. Ferroelectric surfaces

### 2.3.1 Introduction

A technique that we have developed to assemble multi-component devices in a "bottom-up" approach is referred to as Ferroelectric nanolithography (FNL). Ferroelectric materials are the basis of technologies for the traditional passive electronics industry, including recent high density information storage and for use as novel chemical sensors and catalysis processes.[55-57] These properties and the ability to be integrated into current device applications make the study of these processes of great interest.

### 2.3.2. Structure

Ferroelectric materials are characterized by an intrinsic electric dipole. For the case of perovskite compounds, which have the form $ABO_3$ seen in **Figure 2.16**, the electric dipole results from the off-centering of the B site cation within an oxygen octahedral and the displacement of the octahedron with respect to the A-site lattice.

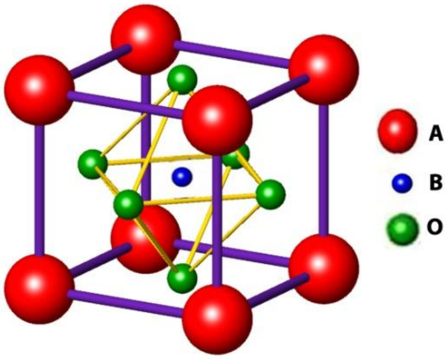

**Figure 2.16** – Crystal structure of a perovskite compound, which has the form $ABO_3$, and a cubic structure above the Curie temperature.

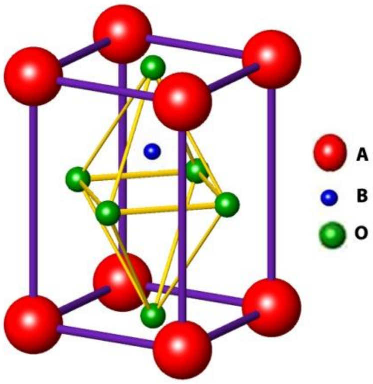

**Figure 2.17** - Crystal structure of a perovskite compound, in which an electric dipole results from the off-centering of the B site cation within an oxygen octahedron and the displacement of the octahedron with respect to the A-site lattice.

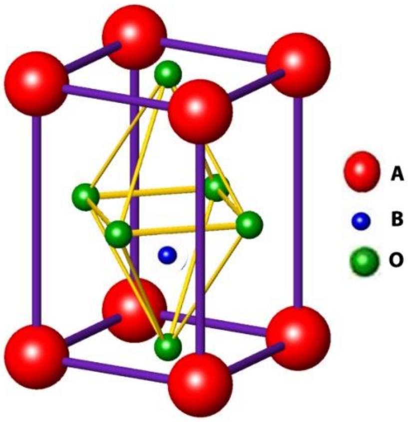

**Figure 2.18** - Crystal structure of a perovskite compound, in which an electric dipole results from the off-centering of the B site cation within an oxygen octahedron and the displacement of the octahedron with respect to the A-site lattice.

In tetragonal compound such as the prototypical barium titanate ($BaTiO_3$), a (100) termination contains in-plane and out-of-plane domain orientations, in which the intrinsic structural dipoles are aligned in parallel. When polarization vectors are pointing out of the surfaces, as in **Figure 2.17**, domains are referred to as “up” or “$c^{+}$”, and in the opposite case (**Figure 2.18**) the domains are “down” or “$c^{-}$”. In compounds with lower symmetry, such as lead zirconate titanate (PZT), the domain geometry is more complex, but still has a component of the vector describing the polarization which terminates at the surface.

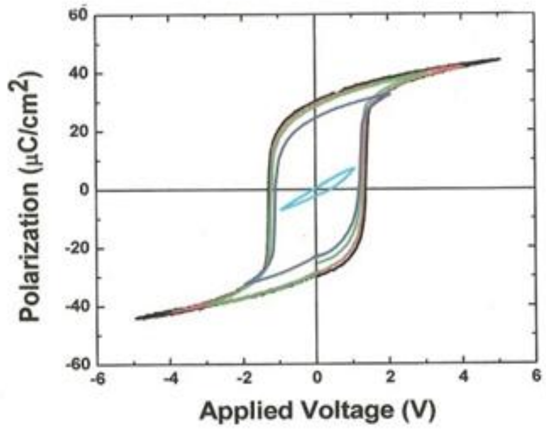

**Figure 2.19** – The applied bias dependence of the polarization for Pb($Zr_{0.7}Ti_{0.3}$)$O_3$,which exhibits typical hysteresis behavior.

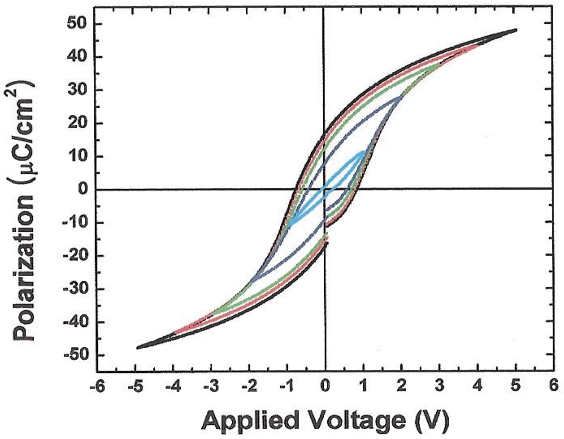

**Figure 2.20** - The applied bias dependence of the polarization for Pb($Zr_{0.52}$ $Ti_{0.48}$)$O_3$, which exhibits typical hysteresis behavior.

Due to the symmetry requirements of ferroelectric structures, they also show piezoelectric properties. This phenomenon is that a crystal can be polarized by the application of a mechanical stress and, conversely, an applied electric field will cause the material to expand or contract. Application of pressure to a piezoelectric material will result in the flow of charge in one direction. The sign of the piezoelectric charge or direction of strain is the same as the direction of the applied mechanical and electrical fields, respectively. Much work has been done to understand both the ferroelectric and piezoelectric properties of materials such as $BaTiO_3$, $SrTiO_3$ and PZT. PZT has been one of the most important materials for devices since the variation in the (Zr/Ti) raito can produce crystal structures from rhombohedral (Zr rich) to tetragonal (Ti rich) and shows a morphological phase boundary (MPB) at 52/48 (Zr/Ti) at which the piezoelectric coefficient is at a maximum. This has made PZT an excellent choice for applications from memory at the Ti rich side due to large polarizations and square hysteresis curves seen in **Figure 2.19,** to actuators and filters with compositions near the MPB due to the large piezoelectric coefficients.[58-60] The magnitude of the piezoelectric effect is related to the direction of the dipole. This effect is the bases of piezo-force microscopy (PFM).

Besides the presence of a stable intrinsic dipole, ferroelectric compounds are also described by the ability to switch domain orientation by application of an external electric field that is greater than the coercive field. Hysteresis curves of the applied bias dependence of the polarization shown in **Figures 2.19 & 2.20**, characterize the fields necessary to switch the polarization. Studies have demonstrated that a variety of techniques can be used to reorient ferroelectric domains. Scanning probe microscopy (SPM), scanning electron microscopy (SEM), and stamping have all been shown to be able to selectively reorient ferroelectric domains.[61, 62] All of these techniques are based on creating an electric field across the ferroelectric that is greater than the coercive field, but understanding the switching mechanisms is necessary to understand the surface properties.

### 2.3.3. Domains

Ferroelectric crystals form regions with uniformly oriented dipoles that are referred to as ferroelectric domains. The domains form as a result of the large energy required to create a crystal with a single domain. Instead, separate domains are formed so that the total energy, including the domain wall energy and depolarizing energy of the domain is minimized. Domains with orientation vectors pointing out of the surface are generally referred to as ($c^+$) domain, while vectors pointing into the crystal are called ($c^-$) domains and in-plane are referred to as (a) domains. The boundaries between (a)-(c) domains are referred to as $90^\circ$ boundaries while ($c^+$)-($c^-$) are called $180^\circ$ boundaries. The formation of $180^\circ$ and $90^\circ$ boundaries minimizes the depolarization fields by compensating for the surface charge in an unpoled ferroelectric. The motion and interaction of domain walls affects the piezoelectric properties of the structure. Extensive studies have focused on understanding and characterizing the formation and static properties of domain structure and motion.[63-66] The advent of various SPM techniques allowed nanometer resolution of domain related structure and electrostatic properties to be probed.[67, 68]

The development of multiple modulation SPM techniques has allowed the systematic study of the domain structure and the resulting surface properties of ferroelectrics. Two of the techniques that have been the most instrumental in developing theory for domain nucleation and growth along with surface band structure and screening mechanisms have been piezo-force microscopy (PFM) and scanning surface potential microscopy (SSPM). Both techniques employ a conductive tip with an applied voltage (ac signal with a dc offset), while PFM is a contact mode technique and SSPM is an intermittent mode technique. The result is a map of the local surface properties, which can be a complex function of surface reconstructions, bound charges, and band bending.

### 2.3.4. Ferroelectric surfaces

The intrinsic dipole in ferroelectric materials results in bound charge at the surface of the ferroelectric. The polarization induces a surface charge that is proportional to the polarization vector. This induced surface charge may be compensated by two possible screening processes at the surface. The first arises from the free charge carriers and defects in the bulk resulting in internal screening process. The second process involves the surface adsorption of charged molecules on oppositely signed domains giving rise to an external screening. Both of these phenomena need to be taken into consideration when discussing the surface state of ferroelectrics, since they will affect the topography, chemical reactivity, electronic, and optical properties.[69] The electronic surface properties are thus determined by the orientation of the polarization, which determines the sign of the polarization bound charge and the internal and external screening charges. A surface with a positive domain will result in a positive bound charge which is compensated by the absorption of negatively charge ions from the ambient, free electrons, or negative defects in the bulk.[70] The opposite charges will be the case for a surface with a negative domain present.

This bound surface charge is always screened at equilibrium and in any environment that is not high vacuum. A variety of mechanisms contribute to a screening charge that is equal and opposite in polarity to the density of surface charges. The surface can either be completely unscreened, partially screened, completely screened or over-screened.[67] A completely unscreened surface is energetically unfavorable, and can only be observed under high vacuum. Over-screened surface are usually observed during domain switching or under illumination, but are not typically observed at equilibrium.[71] Surfaces in ambient conditions are usually found to be either partially screened or fully screened. The state of the screening charge on the surface is not only a function of the polarization, but the shape and size of the space charge region is dependent on variations in the density of states and defects. The internal and external screening processes can modify the electronic surface structure. While the surface dipole induced by the external screening can give rise to a variation in the surface electron affinity, the internal screening leads to band bending at the surface.

In terms of the classic description of semiconductors, the charge at the surface that is a consequence of the polarization causes band bending.[70, 72, 73] Without an intrinsic dipole, the flat band condition exists as seen in **Figure 2.21**. At a negative domain the bands bend up (**Figure 2.22**) and at the positive domains the bands are flat or bending down (**Figure 2.23**).

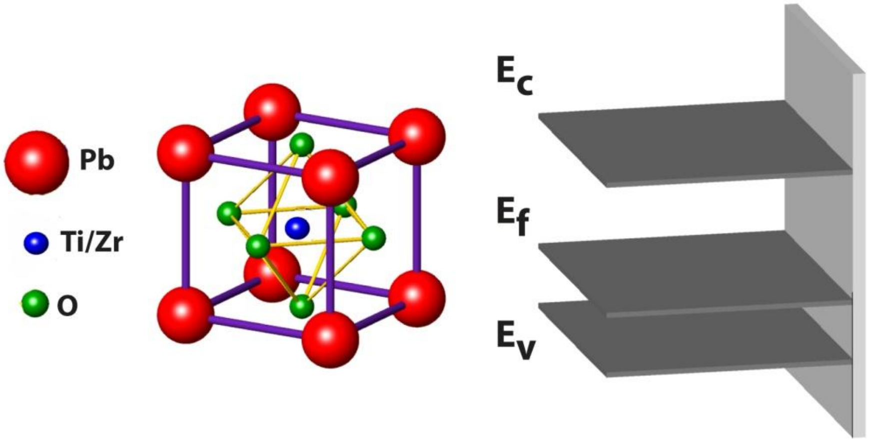

**Figure 2.21** – Schematic illustration of the crystal structure and associated band structure of PZT. The cubic phase perovskite structure is shown without an intrinsic dipole and the resulting flat band condition exist at the surface, in which $E_c$ is the conduction band, $E_f$ the Fermi energy, and $E_v$ the valence band. The surface of the solid is indicted by the perpendicular gray plane.

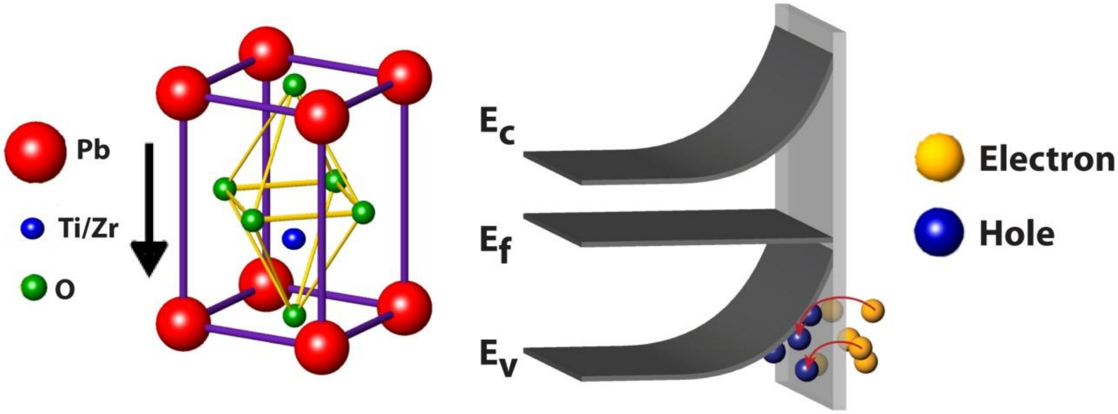

**Figure 2.22** – Schematic illustration of the crystal structure and associated band structure of PZT. The crystal structure on the left shows the atomic displacement in the ferroelectric tetragonal phase in which the octahedrally coordinated Ti/Zr is off center. The polarization induces charge at the surface causes band bending and the migration of holes near the surface for use in photo-oxidation reactions. The orientation of the polarization into the surface causes the bands to bend up at the surface, in which $E_c$ is the conduction band, $E_f$ the Fermi energy, and $E_v$ the valence band. The surface of the solid is indicted by the perpendicular gray plane.

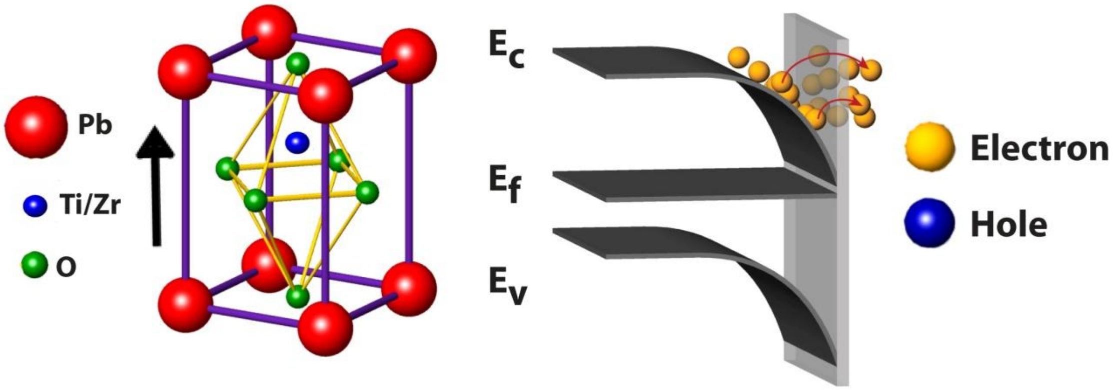

**Figure 2.23** – Schematic illustration of the crystal structure and associated band structure of PZT. The crystal structure on the left shows the atomic displacement in the ferroelectric tetragonal phase in which the octahedrally coordinated Ti/Zr is off center. The polarization induces charge at the surface causes band bending and the migration of electrons near the surface for use in photo-reduction reactions. The orientation of the polarization into the surface causes the bands to bend down at the surface, in which $E_c$ is the conduction band, $E_f$ the Fermi energy, and $E_v$ the valence band. The surface of the solid is indicted by the perpendicular gray plane.

Unlike traditional semiconductors, the band bending in ferroelectrics is generated by the need to screen the spontaneous depolarization field. The internal screening gives rise to an internal electric field which causes band bending, resulting in an accumulation layer near the surface for up domains, and a depletion layer at down domains. Shao et al have demonstrated the under illumination, electrons and holes separate at positively and negatively poled domains surfaces, respectively, and are available for local reactions.[74, 75] This variation in the energy levels at the surface dramatically influences chemical reactions for both molecular adsorption and oxidation/reduction in liquids.

### 2.3.5. Surface reactivity

The surface reactivity of ferroelectrics is complex due to the various screening processes at the surface and the interaction of the resulting near surface layers. The chemical reactivity of the surface may be favorable to drive a reaction at the surface but as discussed above, the development of a screening layer that is of opposite charge compared to the charges required for the reaction implies that any chemistry must involve local tunneling or disruption of the screening layer. A wide range of chemistries have been studied on ferroelectric surfaces, from absorption of various gas species, to the deposition of various metals salts.[76-78] Garra et al and Li et al have shown the selective absorption of various gas species on poled surfaces of $LiNbO_3$ and demonstrated the ability to selectively reorient ferroelectric domains on $BaTiO_3$ to control the absorption of various gas species.[79, 80] Much like the screening processes described in the previous section, the absorption is controlled by the internal screening process at the surface of the ferroelectric and characteristics of the absorbing species. The interaction of various molecules ($CH_3OH$, $CO_2$, $H_2O$, $NH_3$, $CH_5N$, and $C_5H_5N$) on single crystal $BaTiO_3$ was studied by temperature programmed desorption (TPD).[80, 81] TPD showed that the amount of absorbed methanol was greater on reduced surfaces compared to oxidized surface, which indicts that the methanol absorbs and reacts at oxygen vacancies. This work provides insight into the molecular adsorption sites and greater understanding of the mechanisms that control polarization affected surface chemical reactivity.

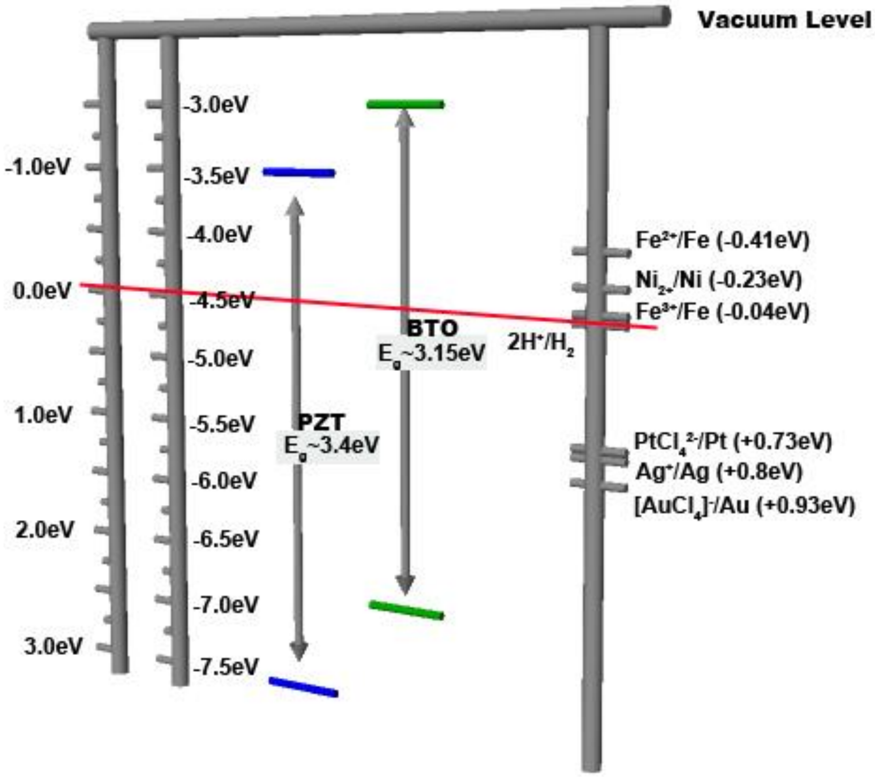

**Figure 2.24** - The energy band diagram of PZT and $BaTiO_3$ compared to the reduction potential with respect to the standard hydrogen electrode of select metal salts.

Several groups have demonstrated the ability to use photo-reduction/oxidation reaction at the surface to deposit metal on ferroelectric surfaces.[82-86] These reactions have been shown to be domain specific, as in the case of absorption of gas species. Lei et al has demonstrated the ability to deposit a variety of metals from aqueous metal-salt solutions on ferroelectric surfaces, including the photo-reduction of Ag, Au, and Pt along with the photo-oxidation of metals such as Co, Ni, and Fe.[87] The reduction chemistry is controlled by the band structure of the ferroelectric (which can be considered a wide-bandgap semiconductor), the Stern layer at the surface and the reduction potential of the electrolyte solution. The energy band diagram of PZT and $BaTiO_3$ compared to the reduction potential with respect to the standard hydrogen electrode of select metal salts are shown in **Figure 2.24**. The Stern layer is a double layer structure that is composed of the layer of accumulated surface charges from the ferroelectric surface and the resulting layer of oppositely charge ions from the electrolyte solution. In the case of a "$c^+$" domain, where the bands bend down at the surface, a layer of negatively charge ions from the electrolyte solution are Coulombically attracted to the positively charge surface. This means that electrons must tunnel through this layer to participate in the reduction reaction. The opposite case of a "$c^-$" domain, where the bands bend up at the surface, a layer of positively charge ions from the electrolyte solution are Coulombically attracted to the negatively charge surface. Multiple types of metal nanoparticles can be deposited sequentially and/or simultaneously and it was shown that super-bandgap energy is required to excite carriers from the surface to participate in the reaction with the metal ions in solution.[88]

Roherer et al and others have studied the reaction of various metal species on various ferroelectric surfaces and heterostructures.[84, 86, 89] The mechanism of the spatially selective reactivity varies with the phase along with the surface orientation and film thickness. Thin films of varying thicknesses of $TiO_2$ were grown on $BaTiO_3$ and the reactivity was studied by photoreduction of Ag on the surface. It was shown that the carriers generated in the ferroelectric pass through the $TiO_2$ thin film and react above the domains on which they would have been reduced on the $BaTiO_3$ bare substrate.[73] This indicates that the reactivity of the $TiO_2$ thin film is insensitive to the phase and orientation of the $TiO_2$ and more influenced by the underlying $BaTiO_3$. Once the $TiO_2$ is thick enough to exhibit bulk properties, the deposition began to be influenced by the phase and orientation of the $TiO_2$ but in some cases the reactivity was enhanced on the $TiO_2$ with the underlying ferroelectric substrate than on an isolated $TiO_2$ film.  The structure and therefore the site specific reactivity is still being studied and although it has been shown that domain oriented deposition of metal nanoparticles is possible, it has not been shown how to control the size, density, and spacing of the nanoparticle assembly for further applications as a platform for hybrid device applications.

# 3. Experimental procedures

## 3.1. Introduction

This chapter will discuss the experimental parameters and procedures to create a test structure to determine the transport mechanisms controlling the opto-electrical response of hybrid AuNP nanostructures. Citrate reduced AuNP's will be deposited on a functionalized glass substrate, with varying particle size and spacing to allow linking of the AuNP arrays with various α-ω dithiol-terminated *meso*-to-*meso* ethynebridged porphyrin supermolecules. The characterization and control of a ferroelectric surface with Ferroelectric Nanolithography (FNL) allows the parameters controlling the growth mechanisms to be determined while utilizing the metal nanoparticle arrays to understand the transport in these hybrid nanostructures linked with the same porphyrin supermolecules. The protocols for property characterization are described for the structure of AuNP's on glass and PZT substrates, and the opto-electrical response of hybrid assemblies.

## 3.2. Fabrication of nanoparticle arrays on glass substrates

### 3.2.1. Surface functionalization

Glass samples were cleaned in a fresh piranha (3:1 $H_2SO_4$:$H_2O_2$) solution for 30 minutes. Samples were rinsed in deionized water then cleaned in concentrated KOH at 75$^{o}$C for 1 minute followed by another rinse in deionized water and dried with nitrogen. Samples were further cleaned in a UV-ozone cleaner for 1-2 hours, then directly placed in a dry nitrogen glove box. Glass samples were submerged in a 5% solution of either (3-Aminopropyl)triethoxysilane, 3-aminopropyl(diethoxy)methylsilane or (3-

Aminopropyl)trimethoxysilane in anhydrous toluene for 1 hour – 48 hours to fully functionalize the surface. Samples were removed from the glove box, rinsed in toluene, dried with nitrogen, and placed in a drying oven at $30^{o}$C for 48 to 60 hours.

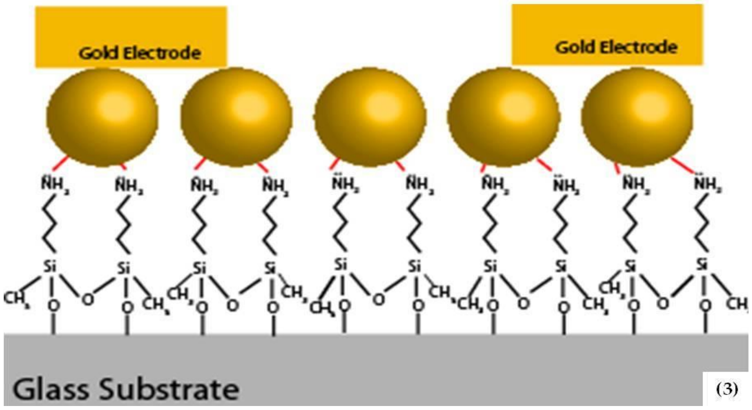

**Figure 3.1** – Schematic illustration of the functionalization of a glass substrate with either (3-Aminopropyl)triethoxysilane, 3-aminopropyl(diethoxy)methylsilane or (3-Aminopropyl)trimethoxysilane in anhydrous toluene and the resulting deposition of citrate reduced gold nanoparticles (AuNPs).

Immersion of the modified substrates in a citrate stabilized AuNP aqueous solution leads to the protonation of the amino groups on the surface. The positively charged surface electrostatically attracts the negatively charged citrate stabilized AuNP. A representation of the general structure can be seen in **Figure 3.1**. The use of all three amino-silanes was employed to determine if the specific functionalizing group affected the density of the resulting AuNP arrays. It was found that the functional group did not appreciably affect the final particle density, so the amino-silanes were used interchangeably in functionalizing the surface.

### 3.2.2. Synthesis of gold nanoparticles

Gold nanoparticles (AuNP) were synthesized through a standard citrate reduction method and obtained through commercially available sources (Ted Pella). In the case of commercially available citrate reduced AuNP, the sizes of the particles varied from 5nm to 40nm with approximately a 10% variation in particle sizes. AuNP of 16nm, 32nm, and 46nm were produced through a standard citrate reduction, where combining hydrogen tetrachloroaurate ($HAuCl_4$) with sodium citrate ($Na_3Ct$) produces AuNPs. The size of AuNPs is controlled by the ratio of $HAuCl_4$ and $Na_3Ct$ in the solution and was determine that a ratio ($HauCl_4$:$Na_3Ct$) of 0.1, 0.5, and 1 produced 16nm, 32nm, and 46nm AuNP, respectively.

### 3.2.3. Deposition on glass

The final AuNP density was controlled by immersion time of the amine-functionalized glass substrates in the appropriate citrate stabilized AuNP solution. Deposition times varied from 5 minutes to 96 hours. Deposition of multiple sized AuNPs was done in consecutive (not concurrent) deposition steps. It was found that as the size of the AuNPs increased, so did the deposition time to achieve a saturated surface. Therefore, when depositing bimodal distributed AuNP assemblies, the larger sized AuNPs were deposited first, then the smaller sized AuNP were deposited on the surface.

## 3.3. Fabrication of nanoparticle arrays on ferroelectric substrates

### 3.3.1. Thin film properties

Lead zirconate titanate (PZT) was obtained from Inostek with the following layer stack.

*PZT (150nm) / platinum(150nm) / titanium(10nm) / silicon dioxide(300nm) / silicon*

The sol-gel thin film was grown with two composition ratios of Zr/Ti (30/70) and (52/48). The texture of the Pt layer was controlled to produce either the (111), or (100) crystal orientation. Annealing was done in an excess of 10% PbO to assure that the desired composition ratios.

### 3.3.2. Photo-reduction of metal salts

The PZT wafers were cleaved into approximately 5mm$^2$ pieces and placed in an atomic force microscope (AFM) (Veeco Dimension 3100NS-IV). The deposition of metal nanoparticles on the PZT surface is realized using Ferroelectric Nanolithography (FNL). The lithographic process is illustrated in **Figure 3.2**. The reorientation (poling) of the ferroelectric domains was accomplished by applying a bias to a Pt/Ir coated tip (resonant frequency 70kHz, 1.4N/m force constant) while scanning the surface in contact mode. **Figure 3.2(a)** demonstrates the physical geometry, where the bottom Pt electrode is grounded to the sample plate, while a positive or negative 10 volts is applied to the conductive tip. The patterning was accomplished by using either a computer programmable controlled bias for complex patterns or by manually switching the bias while scanning for simple patterns, such as lines or squares. The computer programmable software employed a scheme where each bit of a scan line was assigned a positive or negative voltage. This allowed the system to scan over the surface and selectively reorient domains to create complex patterns. This is illustrated in the scanning surface potential microscopy (SSPM) image in **Figure3.2(c)**, where the left image is the topography and the right image is the surface potential. When manually poling the surface, the process began by first applying a positive voltage to the tip while scanning the area of interest (back-poling). After the whole area has been switched, the aspect ratio is changed to 10:1 or 8:1 and the surface is rescanned with a negative voltage is applied to the tip. This method can create simple patterns on the surface such as lines of variable width and length on the surface. **Figure 3.2(b)** shows an SSPM image of simple lines and illustrates the relationship to the underlying domain orientation.

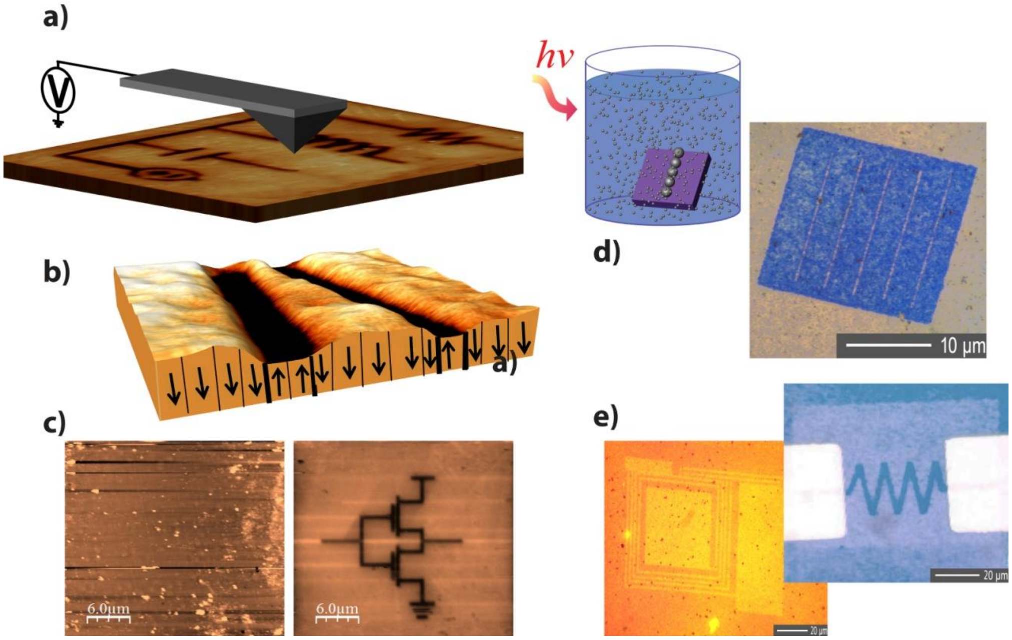

**Figure 3.2** – Ferroelectric Nanolithography (a) a biased conductive SPM tip selectively reorients ferroelectric domains. (b) the relation of domain orientation direction and surface potential. (c) the topographic structure of lead zirconate titanate (PZT) surface (left) is compared to the surface potential (right) after polarization patterning. (d) incident light creates electrons and holes in the PZT that is submerged in a metal salt solution and nanoparticles form on the positively polarized patterns. (e) patterns of metal nanoparticles made in the configuration of capacitance and resistance based devices and integrated into a device.

The patterned substrates were submerged in the aqueous solution, illuminated, and reduced metal nucleates and grows on the substrate, as shown in **Figure3.2(d)**. Millique water and reagents (99.9% silver nitrate, 99.999% hydrogen tetrachloroaurate and 99.999% ammonium tetrachloroaurate) were used to prepare solutions. The patterned surfaces were submerged into metal-salt solutions varying in concentration ranged from 1µM to 10mM. Irradiation from a Newport/Oriel arc lamp with a 200WHg(Xe) bulb was directed at the surface at room temperature. The incident power and intensity were controlled with 250nm and 270nm optical band-pass filters, and a 450nm short-pass filters. The deposition times were varied from 5 minutes to 3 hours. The samples are rinsed in deionized water and dried with nitrogen. **Figure 3.2(d)** & **(e)** are examples of domain induced production of silver and gold nanoparticles on a patterned PZT surface. **Figure 3.2(e)** demonstrates how the combination of patterning and localized reactions can yield complex geometries typical of devices.

## 3.4. Device test structure

### 3.4.1. Deposition of metal contacts

Gold contact pads were deposited on the surface by way of a thermal evaporator (Thermonics). Thin films between 30nm and 100nm of gold were evaporated on the surface. The system was allowed to pump down to between $10^{-6}$ and $10^{-7}$ torr before starting the evaporation. The thickness was measured with a quartz thickness monitor and deposition rates were kept between 1Å/sec to 5Å/sec.

### 3.4.2. Device configuration

The size and configuration of the device area was defined by employing a physical masking technique or photolithography. The physical masking technique was accomplished with shadow masks, which created devices with 35µm and/or 70µm gap separation. **Figure 3.3** illustrates the processing steps for depositing the gold contact pads. Beginning with a bare thin film substrate in **Figure 3.3(a)**, a 50 µm thick molybdenum mask was place over the bare substrate, as shown in **Figure 3.4(b)**.

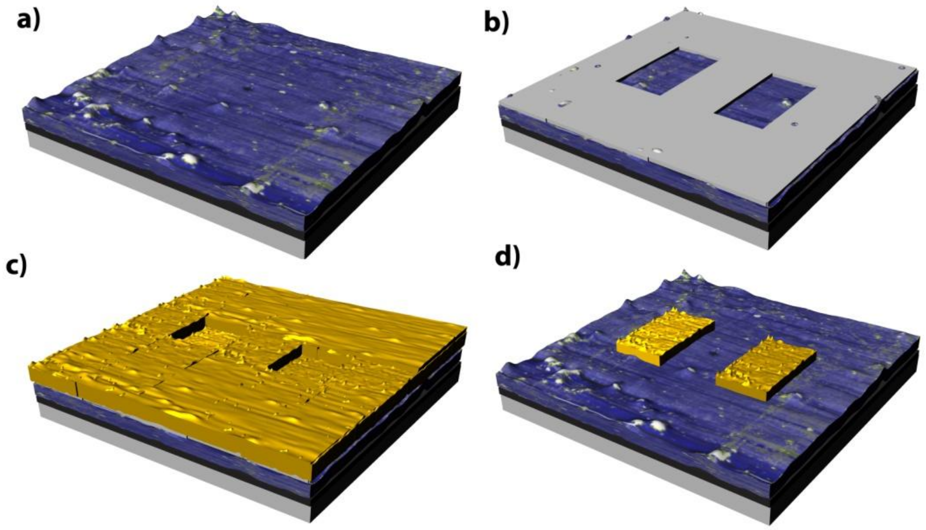

**Figure 3.3** – (a) Bare thin film substrate. (b) 50 µm thick molybdenum mask was place over the bare substrate to define the separation between the contact pads. (c) gold was evaporated over the whole surface. (d) the molybdenum mask was removed from the surface to reveal contact pads separated by 35µm or 70µm.

Gold was evaporated over the whole surface (**Figure 3.3(c)**), then the shadow mask was removed to reveal gold pads with a predefined gap between them, as seen in **Figure 3.3(d)**. Each shadow mask was used independently to create gaps between the contact pads of respective sizes or were used together to create an alignment system. In the latter case, gold was evaporated through a 70μm gap shadow mask to create alignment markers then processed in the steps illustrated in **Figure 3.2** to create the AuNP nanostructures. The sample was placed back in the evaporator with a 35μm gap shadow mask and gold contacts were deposited to connect the nanostructures for device testing.

Photolithography utilizes the same principles as the process with the shadow masks but employs photoresist as the masking layer instead of the molybdenum sheet. Beginning with a bare thin film substrate again (**Figure 3.4(a)**), the sample had photoresist (Microposit S1813) spun onto the PZT samples at 3000RPM for 30 seconds to produce the structure seen in **Figure 3.4(b)**. Samples were placed in a mask aligner (Karl Suss MA4), exposed for 12 seconds, and subsequently developed in developer (Microposit MF-319) for 30 seconds while agitating. The resulting masking structure can be seen in **Figure 3.4(c)**. Samples were rinsed in deionized water and dried with nitrogen. After evaporation of gold over the whole sample, as seen in **Figure 3.4(d)**, the excess gold was lifted-off by placing the samples in acetone. After the lift-off, the samples were rinsed in IPA and deionized water, and dried with nitrogen to reveal the device structure in **Figure 3.4(e).** The structure in **Figure 3.4(e)** was also used as alignment markers, where AuNPs were subsequently deposited using FNL, between the gold pads produced in **Figure 3.4(e)**. The processing steps illustrated in **Figure 3.4(b-d)** were repeated except employing a different photomask that was aligned to the previous photolithography step, but produced the contact pads seen in **Figure 3.4(f)**.

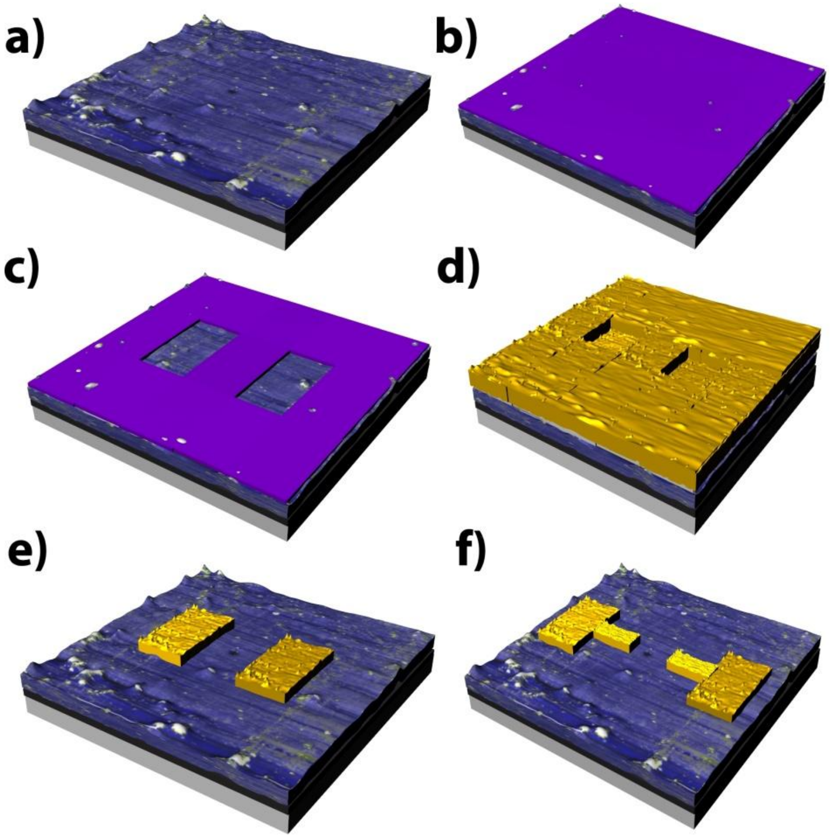

**Figure 3.4** – (a) Bare thin film substrate. (b) approximately 1μm of photoresist (Microposit S1813) was spun at 3000RPM for 30 seconds. (c) the sample was subsequently developed in developer (Microposit MF-319) for 30 seconds while agitating. (d) gold was evaporated over the whole surface. (e) the excess gold was lifted-off by placing the samples in acetone to reveal the predefined contact pad configuration. (f) using the contact pads produced in **Figure3.4(e)** as alignment markers, contact pads produced with a different photomask can be aligned to make contact to the AuNP assembly.

## 3.5. Molecule functionalization

Adsorption of dithiol-PZn$_x$ onto the AuNP arrays was performed under a nitrogen (ultrahigh purity grade) atmosphere in a glovebox (PlasLabs). The solvent tetrahydrofuran (THF, HPLC grade, Fisher) was distilled with sodium under nitrogen and collected into a vacuum-sealed flask (Chemglass) and subjected to repeated freeze – pump-thaw-degas cycles. For these studies, the THF solvent was subject to multiple (up to eight) freeze-pump-thaw-degas cycles as this step was found to be critical in promoting successful dithiol-PZn$_x$ attachment to the AuNPs. To an acetyl-protected dithiol-PZn$_x$ solution (1µM in THF), 4 µL/mL of $NH_4OH$ was added to unmask the thiolate functionality. The substrates with surface-bound AuNPs were then immersed into adsorption vials (Wheaton) containing this solution and set aside for 1-24 h. The substrates were rinsed with THF and dried under a stream of $N_2$.

## 3.6. Characterization

### 3.6.1. Microscopy

Samples were inspected to verify the particle size and distribution by employing a Veeco 3100 atomic force microscopy (AFM) with an IVa controller and scanning electron microscope (SEM). AFM images were acquired using tapping mode, which is an intermediate contact method as not to disturb the placement of the particles on the surface. Images were obtained using 70kHz (1.4N/m) silicon tip.

The switching behavior of the ferroelectric domains was inspected by using piezo-force microscopy (PFM) and/or scanning surface potential microscopy (SSPM). While PFM is a direct measure of the orientation of the dipole, SSPM is an indirect measure of dipole direction by measuring the difference in surface potential creates by the electrical field produced from the underlying dipole. PFM and SSPM images were obtained using a Pt/Ir coated tip (70kHz, 1.4N/m).

PFM is the direct measure of the direction of the orientation of the ferroelectric domain. When the tip is in contact with the surface and with the bias being applied, the local piezoelectric response is being detected as the first harmonic component of the tip deflection. For $c^-$ domains (where the polarization vector is pointing into the surface), the application of a positive tip bias results in the expansion of the material, and the surface oscillations are in phase with the tip voltage. The opposite response occurs on $c^+$ domains, where the material will shrink and the surface oscillations are 180° out-of-phase with the applied bias. The phase of the first harmonic signal yields the information on the polarization direction, and more specifically the component vector perpendicular to the surface. To obtain the complete vector magnitude and direction, the vertical PFM signal described above would have to be combined with the lateral signal to quantify the total vector.

On the other hand, SSPM measures the surface potential due to the underlying domain orientation. This imaging technique is similar to electrostatic-force microscopy (EFM), but where EFM detection is based on the frequency shift or amplitude change, SSPM is a nulling technique. This has many advantages over EFM with the greatest enhancement being the decreased sensitivity to topographic artifacts. SSPM is a dual pass imaging technique where the first scan obtains the topography information, then the second scan retraces the topographic structure over the same line to obtain the local surface potential. When the biased tip is over the surface, the cantilever experiences a force when the potential at the surface is different from the tip. The surface potential can be ascertained by varying the applied dc voltage until the first harmonic of the signal, resulting from force exerted on the tip, is zero. The result is a map of the local surface potential which can be a complex function of surface reconstructions, bound charges, and band bending.

### 3.6.2. UV-Vis spectroscopy

The samples were characterized by UV-Vis spectroscopy using a Varian 5100 spectrometer. The samples were examined using a dual-beam setup with the reference being a functionalized glass substrate with no gold particles. The scanning range was from 250nm-800nm and each sample was zeroed before each scan to facilitate comparison of spectra. Analyses of the spectra were performed by curve fitting with multiple Gaussian peaks in Origin (OriginLab 7.5). Determination of the best fit was performed by fitting the UV-Vis spectra with increasing numbers of Gaussian peaks. First order examination of the UV-Vis spectra (black curve) seen in **Figure 3.5(a)**, shows maxima located at approximately 650nm, 525nm, and below 350nm. Although the left most Gaussian peak (green curve) is used in the fitting process, it is just an artifact from the substrate. Protocols within the Origin software allow assigning peak locations at below 350nm and at approximately 525nm and 650nm. The green, blue and magenta curves in **Figure 3.5(a)** represent the three Gaussian curves that comprise the best fit curve (red curve) of the UV-Vis spectra. A comparison of the UV-Vis spectra (black curve) with the best fit curve (red curve) in **Figure 3.5(a)** shows that the curve fit deviates from the UV-Vis spectra below 500nm, while providing a good fit for the data above 500nm. Examination of the spectra and the deviation in the curve fitting indicates the possible presence of an additional peak located around 425nm. This peak location can be assigned to the absorption maximum located near the same wavelength of the porphyrin molecules, as seen in **Figure 2.15**.

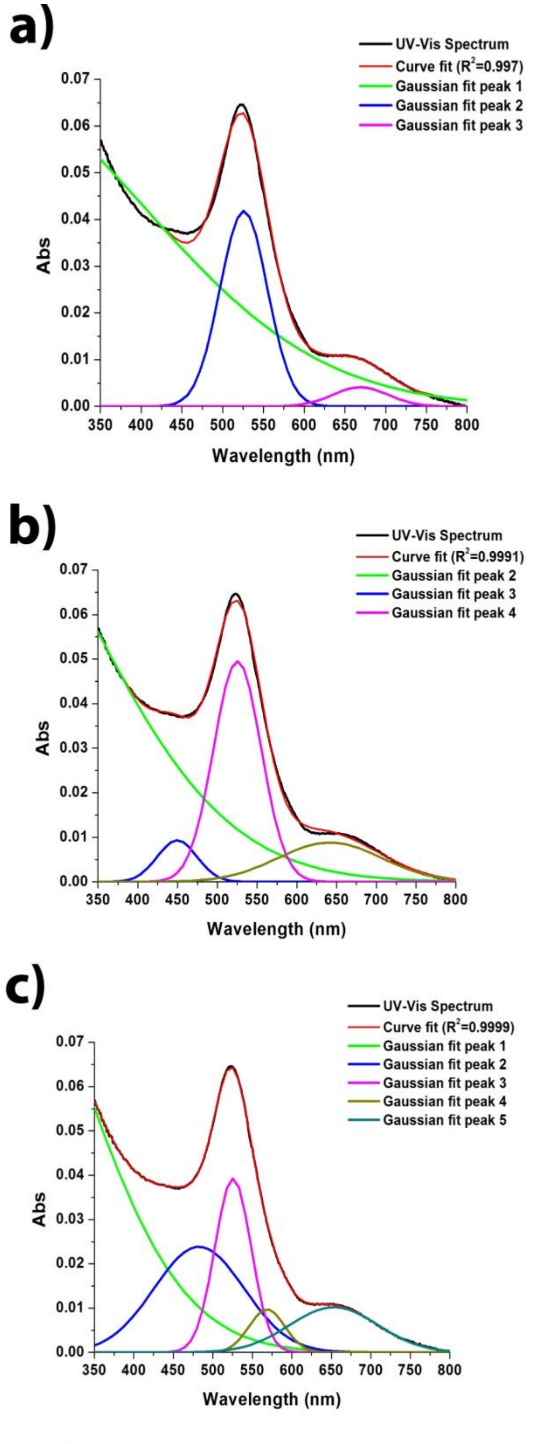

**Figure 3.5** – Gaussian peak fits to UV-Vis spectrum curves. The curves were fit to three, four, five, and six Gaussian peaks to compare the fit. Although the left most peak is used in the fitting process, it is just an artifact from the substrate. (a) fits 3 Gaussian peaks, (b) fits 4 Gaussian peaks, with the fourth peak approximately placed at 430nm from examining the curve fit in (a). (c) fits five Gaussian peaks and give the best fit. A sixth Gaussian peak does not produce a better fit.

Assigning another Gaussian peak at approximately 425nm results in the curve fit (red curve) seen in **Figure 3.5(b)**. The resulting curve fit for four Gaussian peaks exhibits a better fitting parameter ($R^2$~0.9991) than in the previous case of three Gaussian curves ($R^2$~0.997). Although the additional fourth peak exhibits a better fit below 500nm, it also results in a worse fit at longer wavelengths. Further examination of the porphyrin molecular absorption spectrum indicts another smaller absorption maximum around 580nm. The addition of a fifth Gaussian peak at approximately 580nm, results in the red curve fit seen in **Figure 3.5(c)**. This curve fit is in excellent agreement ($R^2$~0.9999) with the UV-Vis spectra. The spectra was further fit to six Gaussian peaks but exhibited no further enhancement of the fit. Therefore, since the best fit was given by peaks associated with expected physical interactions, UV-Vis spectra in this work were fit to five Gaussian peaks, with the peak locations at approximately 650nm, 580nm, 525nm, 425nm, and below 350nm.

### 3.6.3. Opto-electrical characterization

All samples were characterized by a Lakeshore Desert Cryogenics probe station. Temperature dependent studies were done from 80K-300K and photoconductivity measurements were performed using a blue (405nm, 5mW), green (533nm, 3mW), and red (655nm, 5mW) laser diode. The photon flux was calculated by measuring the output power of the laser with a power meter (Newport 1935-C) and dividing the power by the energy of the incident wavelength of light. The photon flux per unit area was then obtained by dividing the photon flux by the area of the spot size for each laser which was determined by optical inspection.  The measured power and spot size for the 405nm, 533nm, and 655nm laser diodes were as follows:

*405nm laser diode: 1.55mW, 0.8mm diameter*

*533nm laser diode:  1.73mW, 1.1mm diameter*

*655nm laser diode:  2.0mW, 1.75mm diameter*

The contact area of the device was determined by optical inspection as well.  Probes tips were made of CuBe and the system had less than an ohm resistance throughout.  The electrical characterization was performed with a electrometer (Keithley 6417A) with 10fA resolution. Open circuit and 10GΩ test resistor measurements confirmed proper calibration of the system before each electrical test with a noise floor of 100fA. Measurements were conducted in ambient and vacuum conditions.

# 4. Properties of hybrid AuNP nanostructures on glass

## 4.1. Introduction

In order to understand transport through porphyrin linked AuNP assemblies, a simple model system consisting of AuNP arrays on a glass substrate was employed. This control allows particle size, density, separation, and molecular length to be systematically varied to examine the transport mechanisms and the opto-electrical response of hybrid AuNP devices.

## 4.2. Nanoparticle array fabrication

As discussed in Chapter 3, various surface functionalizations (APDES, APTES, and APTMS), particle sizes and distributions were used to create systematic test structures. Both synthesized citrate reduced AuNPs and citrate stabilized AuNPs from commercial sources were used to create the hybrid nanostructures. The AuNP arrays in **Figure 4.1** are examples of glass substrates functionalized with 5% solution of 3-Aminopropyl(diethoxy)methylsilane (APDES) in toluene. The APDES functionalized glass substrates were immersed in aqueous solutions of citrate stabilized AuNPs where the surface coverage and the particle size distribution of the AuNPs were established using scanning electron microscopy (SEM). Citrate-stabilized AuNPs of diameters 16, 32, and 46 nm were synthesized according to a previously published methodology (also described in detail above in Section 2.3.2.) and are seen in **Figure 4.1(a-c)**, respectively.[90] It was found that to produce saturated particle densities on the surface required an immersion time of approximately 96 hours; sample-to-sample variations in measured particle densities were 10%. The areal coverage of the particles in these samples was 52 ± 3%, 54 ± 3%, and 46 ± 2%, respectively. The size of the nanoparticle is less important than the particle separation, and it was found that smaller particles would pack closer together, while larger particles would not be close enough to be linked with the porphyrin molecules.

The images in **Figure 4.2** are glass substrates functionalized with (3-Aminopropyl) triethoxysilane (APTES) and immersed in a commercial available gold colloid solution of 30nm diameter particles. **Figure 4.2(a-d)** are atomic force microscope (AFM) images of samples with immersion times of 5, 100, 180, and 200 minute, respectively. The areal coverage of the particles in these samples is 2.6±4%, 38.6±3%, 48.5±3%, 52.6±2%, respectively. The images show an increase in particle density with immersion time and it was found that after approximately 200 minutes of immersion, the particle densities did not increase further, as seen in **Figure 4.2(d)**.

**Figure 4.3(a – f)** are AFM images of the depositions of 15nm, 20nm, and 30nm commercially available AuNPs on glass substrates functionalized with APTES. The left column is immersion times of 100 minutes and the right column is 200minutes. **Figure (a)** & **(b)** show depositions of 15nm diameter AuNPs with areal coverages of 44.1±2% and 77±4%, while **Figure (c)** & **(d)** are 20nm diameter AuNPs with areal coverages of 56.5±2% and 71.8±3% , respectively. **Figure (e)** & **(f)** are 30nm diameter AuNPs with areal coverages of 38.6±3% and 52.6±2%, respectively. These images show that the deposition reaction is faster for smaller particles then for larger particles. Keeping the immersion time constant, but decreasing the AuNP diameter, results in a higher surface coverage, as seen in comparing **Figure (a)** & **(e)**.

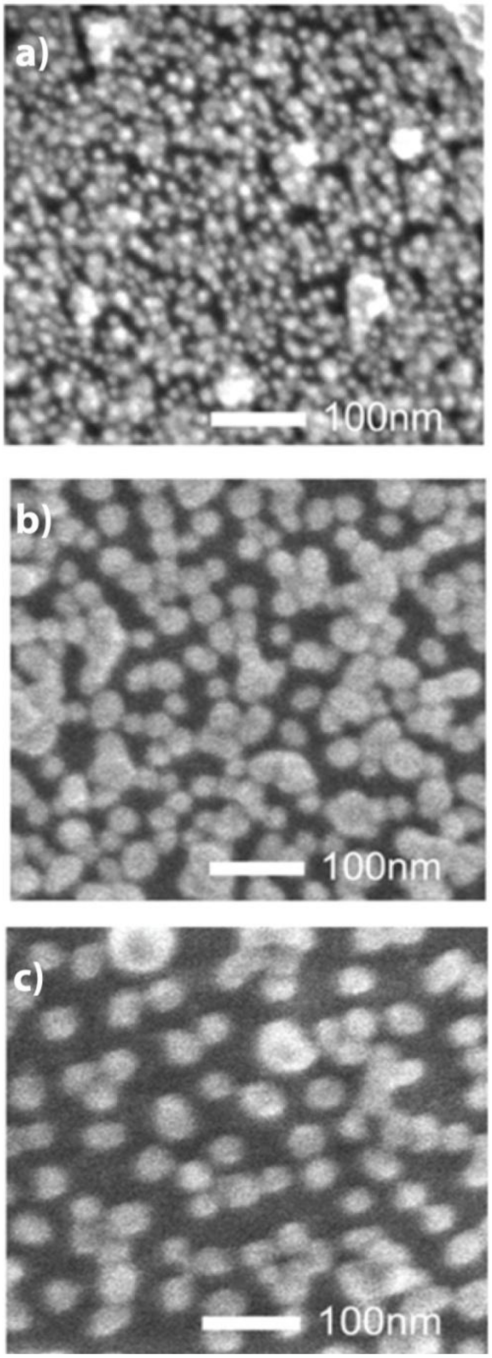

**Figure 4.1** – Synthesized citrate-stabilized AuNPs of (a) 16nm, (b) 32nm, & (c) 46 nm diameter.

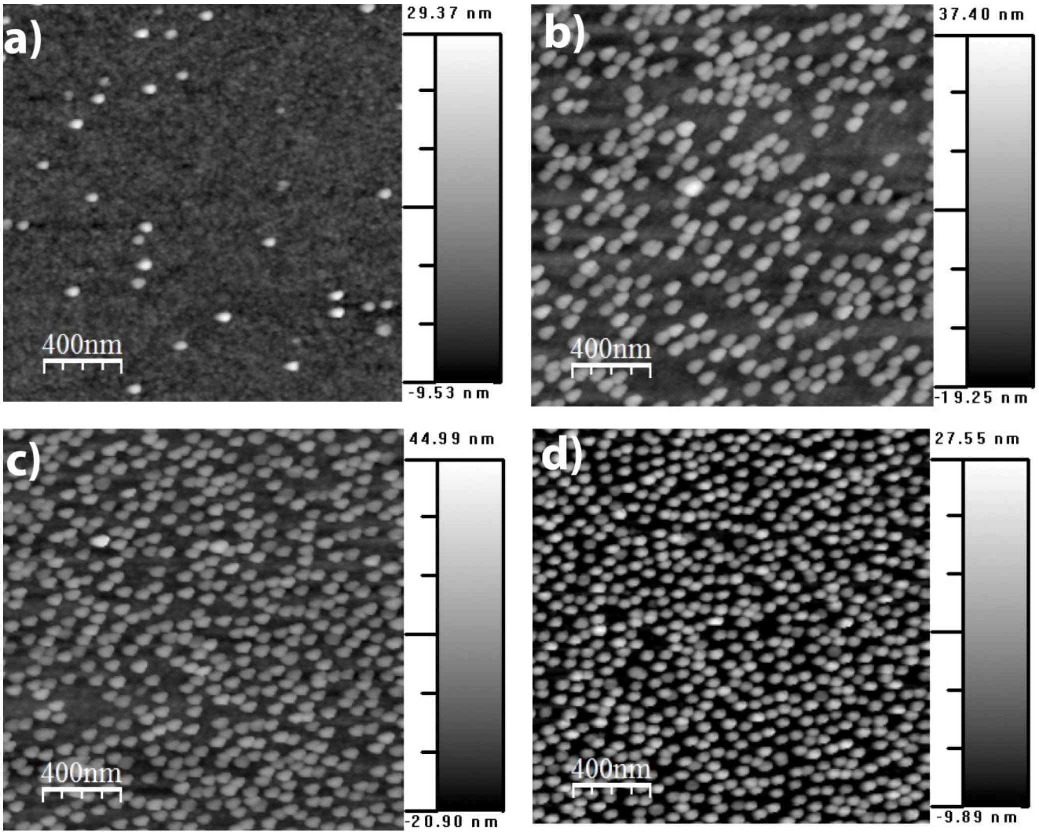

**Figure 4.2** - Atomic force microscope (AFM) images of samples with immersion times of (a) 5, (b) 100, (c) 180, & (d) 200 minutes, respectively.

**Figure 4.4** shows AFM images of bimodal distributions of AuNPs from commercial available sources on APTES functionalized glass substrates. Because of the AuNP size dependence on the deposition rates, the bi-modal arrays were deposited by consecutive deposition steps. The larger sized particles were deposited on the substrate first since it had a longer deposition time and hence was easier to control. The smaller sized particles were subsequently deposited after determining the surface coverage of the larger particles. **Figure 4.4(a-d)** show AFM micrographs of bi-modal depositions of 40nm AuNPs with 40nm, 30nm, 20nm, and 15nm diameter particles, respectively. The initial immersion time in 40nm AuNPs was for 180 minutes in all cases. The subsequent AuNP immersion times of 40nm, 30nm, 20nm, and 15nm diameters were for 25, 60, 15, 25 minutes, respectively. The areal coverage of the particles in these samples are 31.2±2%,44.9±3%, 70.4±4%, and 74.2±3%, respectively.

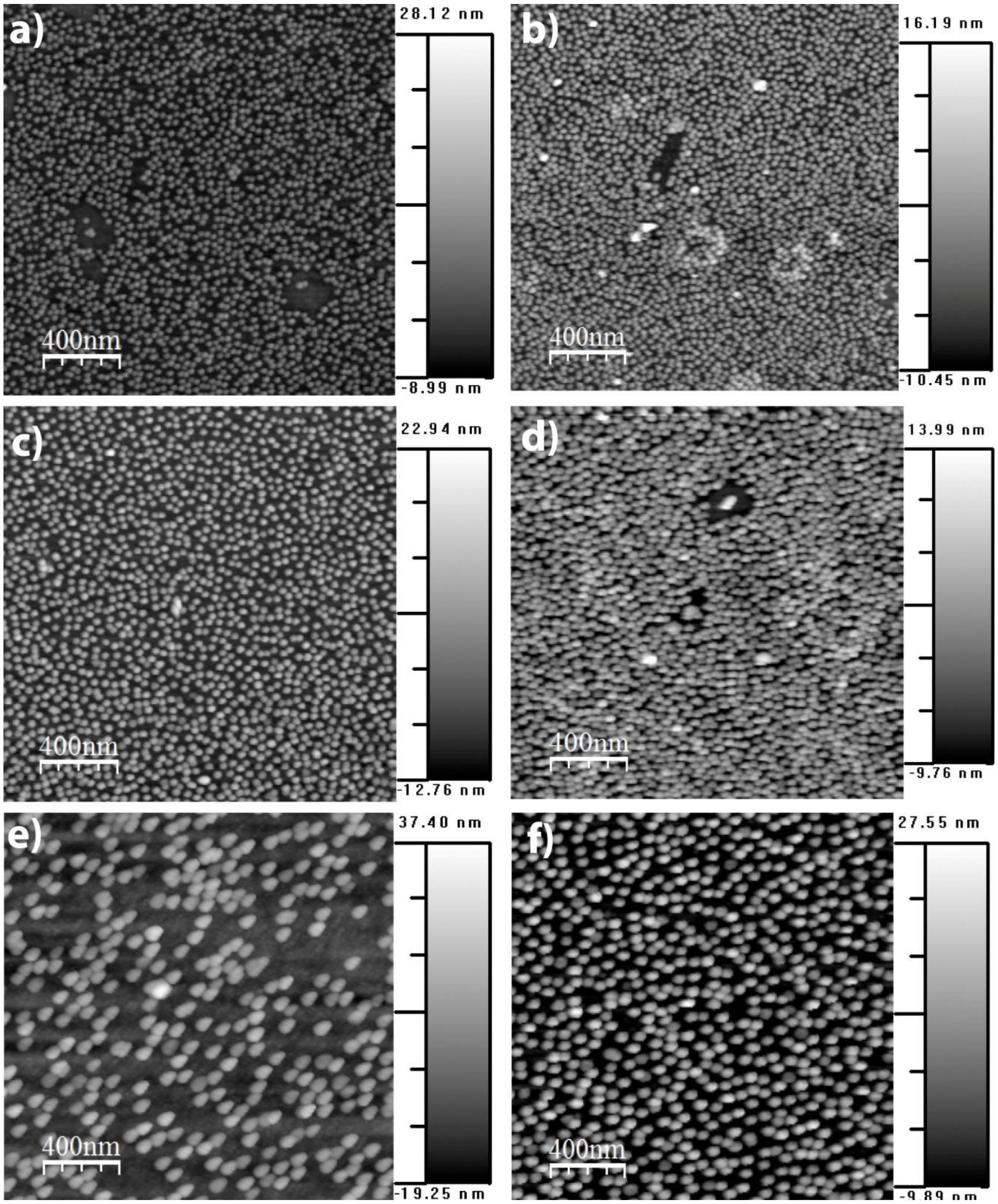

**Figure 4.3** - AFM images of the depositions of 15nm, 20nm, and 30nm commercially available AuNPs on glass substrates functionalized with APTES. The left column is immersion times of 100 minutes and the right column is 200minutes. (a) & (b) show depositions of 15nm diameter AuNPs with areal coverages of 44.1±2% and 77±4%, while (c) & (d) are 20nm with areal coverages of 56.5±2% and 71.8±3% , respectively. (e) & (f) are 30nm diameter AuNPs with areal coverages of 38.6±3% and 52.6±2%, respectively.

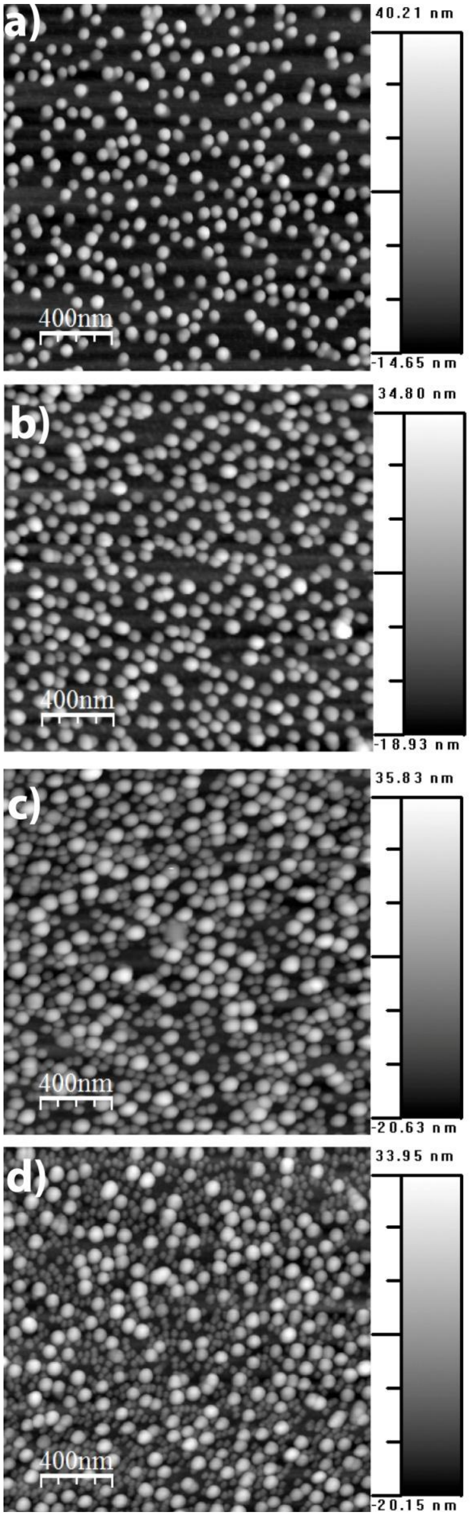

**Figure 4.4** –(a - d) show bi-modal depositions of 40nm AuNPs with 40nm, 30nm, 20nm, and 15nm diameter particles, respectively. The initial immersion time in 40nm AuNPs was for 180 minutes in all cases. The subsequent AuNP immersion times of 40nm, 30nm, 20nm, and 15nm diameters were for 25, 60, 15, 25 minutes, respectively.

The deposition rate and saturation coverage are related to the quality of the surface functionalization. Although great effort was placed on sample preparation to produce reproducible structures, variations occurred. This manifests as a lack of deposition or defect areas in the array with a different surface coverage in the surrounding area. Although the deposition rate is a semi-linear relation with immersion time, the quality of the functionalization affects this rate and hence variable surface coverage can result. Sufficient control was developed so that greater than 90% of the samples produced desirable particle coverage. The process was found to be very robust and provides an excellent platform to determine the transport mechanisms through the zinc-porphyrin supermolecules.

| Functionalization | Particle size | Immersion time | % coverage |
|---|---|---|---|
| **APDES** | 30nm | 5-220min | 3.1-54.3% |
| | 20nm | 5-220min | 15.2-75.35% |
| | 15nm | 5-220min | 32.1-89.7% |
| **APTES** | 30nm | 5-220min | 2.6-52.6% |
| | 20nm | 5-220min | 29.2-88.2% |
| | 15nm | 5-220min | 63.8-92.1% |
| **APTMS** | 30nm | 5-220min | 2.9%-51.4% |
| | 20nm | 5-220min | 45.6%-86.4% |
| | 15nm | 5-220min | 58.2-93.2% |

**Table 4.1** –Processing variables to produce single sized AuNP arrays of 15nm, 20nm and 30nm diameter AuNP nanoparticles and resulting surface coverage.

| Functionalization | Particle size | Immersion time | Particle size | Immersion time | % coverage |
|---|---|---|---|---|---|
| APTES | 40nm | 120min | 30nm | 45-75min | 17-37.4% |
| | | | 20nm | 15-45min | 50-88.4% |
| | | | 15nm | 15-45min | 73.5-94% |
| | 40nm | 180min | 30nm | 60-120min | 20-53% |
| | | | 20nm | 5-30min | 49.4-69.5% |
| | | | 15nm | 5-25min | 61-83.6% |

**Table 4.2** –Processing variables to produce bi-modal distributions of AuNP arrays and resulting surface coverage as a function of surface functionalization, particle sizes and immersion time.

**Tables 4.1** and **4.2** summarize the AuNP deposition parameters. The resulting surface coverage as a function of surface functionalization, particle size/sizes, and immersion times are given. **Table 4.1** provides the processing variables for single sized AuNP arrays, while **Table 4.2** lists the processing variables to develop arrays with a bimodal distribution. In most cases, the processing conditions were such that the interparticle spacing was not optimal to create a device. The particles were either spaced further apart then the length of the zinc-porphyrin molecule intended to link adjacent nanoparticles or a nanoparticle percolation pathway between electrodes resulted in conduction before the deposition of the molecules.

## 4.3. Optical properties of AuNP arrays

These AuNP arrays are a platform to study photocurrent, therefore it is important to consider the interaction of light with the nanoparticles. As mentioned in Section 2.1.4., the absorbance due to the plasmons in AuNP arrays is dependent on the particle size and coupling. Since surface plasmons may affect opto-electronic properties, the optical properties of the AuNP array were characterized. Immersion times provide empirical control of the surface coverage and the optical absorption confirms the degree of coupling in the nanoparticle arrays. The actual coupling will depend, not only on the size and particle separation, but also on the degree of aggregation, which can be inhomogeneous. The optical response of the AuNP arrays was determined by UV-Vis spectroscopy.

**Figure 4.5** compares the effects of particle size, distribution, separation, and aggregation. Although the general trend of increasing immersion time results in an increase in surface coverage and resulting shift of the UV-Vis spectra, it is not a linear relationship. **Figure 4.5(a)** shows the UV-Vis spectra as a function of immersion time for a 30nm AuNP sample. The deposition time was varied from 5 minutes to 200 minutes. The increase in immersion time increases the surface coverage, as seen in **Figure 4.2**, which is observed in the UV-Vis spectra as an increase in the amplitude of the primary peak located at 520nm. The coupling (particle separation and aggregation) between AuNP’s manifests itself in the appearance of a peak located at approximately 650nm. The peak increases in amplitude and red shifts as the surface coverage increases, as theoretically shown in Section 2.1.4. .

**Figure 4.5(a)** also features an example of the limitation of this deposition process. As seen by comparing **Figures 4.2** & **4.5(a)**, increasing immersion time causes increased surface coverage, but the growth of the coupling peak at 650nm does not always scale with immersion time. Comparing the UV-Vis spectra for the 110 minutes with the 120 minute AuNP arrays in **Figure 4.5(a)**, shows that while the primary peak located at ~525nm is approximately the same, the secondary coupling peak at ~640nm has a larger amplitude and is more red shifted for the array immersed 110 minutes. This indicates greater coupling between the particles at a lower surface coverage, which implies the aggregating of particles. This discrepancy between the surface coverage and the UV-Vis spectra could be due to incomplete functionalization of the surface before the deposition of AuNP's or aggregation in solution during the deposition process. In either case, the variation in the optical response of the AuNP assemblies needs to be taken into consideration when interpreting photoconductivity mechanisms in hybrid devices.

**Figure 4.5(b)** show the effects of areal coverage on the UV-Vis spectra for a sample with a bimodal particle distribution of 40nm and 30nm particles. The increase in the amplitude of the primary peak at 525nm and the coupling peak at 675nm is the result of the increase in coverage of the 30nm particles. Both samples were immersed in a 40nm AuNP solution for 120 minutes, while the sample with a surface coverage 16.9% was immersed in a solution of 30nm AuNP particles for 45 minutes, while the sample with a surface coverage of 44% was immersed for 100 minutes.

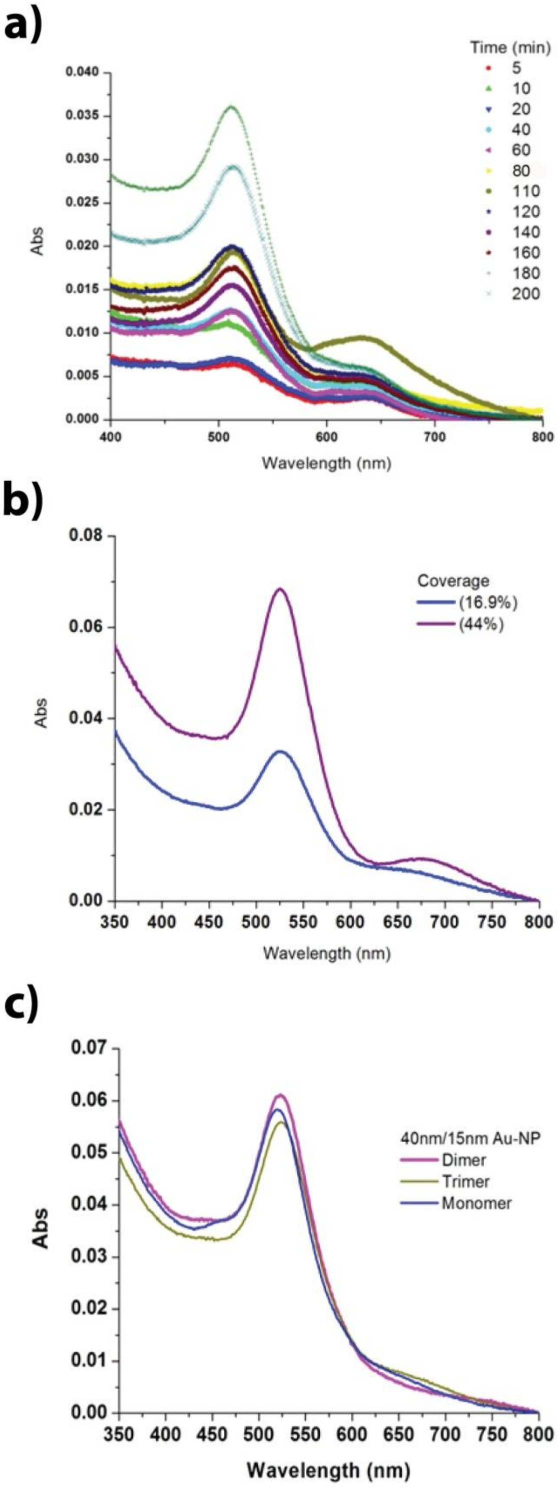

**Figure 4.5** – UV-Vis spectra of AuNP arrays (a) as a function of immersion time from 5 to 200 minutes in a 30nm AuNP solution, (b) as a function of surface coverage from 16.9% to 44% and (c) as a function of a bimodal distribution of 40nm and 30nm AnNP linked with monomer, dimer, and trimer molecules.

The effects of the molecular linker group can be observed in the UV-Vis spectra in **Figure 4.5(c)**. The UV-Vis spectra represent a bimodal distribution of 40nm and 15nm AuNP arrays with similar surface coverage. The appearance of a peak at approximately 460nm indicates the successful attachment of the molecular linker group to the AuNP arrays. The larger intensity of this peak for an attached monomer molecule can be understood by referencing the absorption spectrum of the porphyrin complexes seen in **Figure 2.15**. The monomer has a main peak that is centered at approximately 440nm and is 33% larger than the largest peak for the dimer or trimer, which has peaks located at 490nm and 415nm. Therefore, the primary absorption peak of the monomer is more visible in the UV-Vis spectra of the linked AuNP assembly because the peak is further from the primary peak for the AuNP array. The variation in the optical response of the AuNP arrays needs to be taken into account when designing the hybrid device structure.

## 4.4. Temperature dependent dark conductivity

### 4.4.1. Temperature dependent conductance

The device structure was fabricated as described in Section 3.4. The conductivity data in **Figure 4.6** illustrate the conductance of the high density 16 nm, 32nm and 46nm arrays, seen in **Figure 4.1(a – c)**, respectively, before (dotted line) and after (solid line) molecule attachment. Note again that it is not the size of the particles that is important but the separation between the nanoparticles. As shown above, the smaller the particle diameter, the smaller the particle separation for these samples.

As seen in **Figure 4.6**, before the molecular deposition, the nanoparticle arrays exhibit a wide range of conductance. In both the 32nm and 46nm samples, the conductivity was minimal, falling within the noise of the electrometer indicating that the AuNP array density were below the percolation threshold. After molecular deposition, the 46nm sample still had almost zero conductance, while the increase in conductivity of the 32nm sample indicates that the sample had the optimal interparticle spacing to link the dithiol-$PZn_3$ to adjacent nanoparticles and create a full conductive path between the electrodes. The 16nm AuNP array was conducting before the molecular deposition, and the conductance increased with molecular attachment.

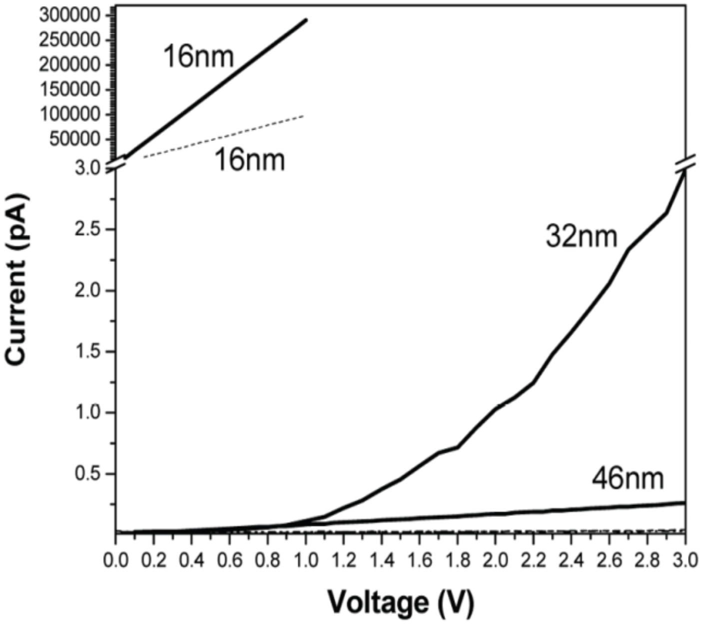

**Figure 4.6** – The conductance of the high density 16 nm, 32nm and 46nm arrays, seen in **Figure 4.1(a – c)**, respectively. The conductivity before (dotted line) and after (solid line) molecular attachment are compared.

Note that while this conductivity is 7 orders of magnitude higher than that of the substrate leakage, it is much lower than that for metal films, indicating that only a fraction of the particles provide conducting pathways. The addition of linker molecules increases the conductivity by increasing the number of current pathways in the array. Subsequently, only the 16nm and 32nm samples were examined to determine the charge transport mechanisms. **Figure 4.7** compares the temperature dependent conductivity at one volt for the 32nm and 16nm AuNP arrays. In one, the conduction decreases with increasing temperature as expected for a metallic array (red dotted), while in the other, conductivity increases with increasing temperature (black dotted) indicating a thermally activated conduction process. Sample 1 in **Figure 4.7** is the 32nm AuNP array in which the conductance exhibits temperature independence below 150K and an increasing conductance with temperature above 150K. This comparison of the 32nm and 16nm samples demonstrates that a metal–insulator transition occurs at a critical particle density.

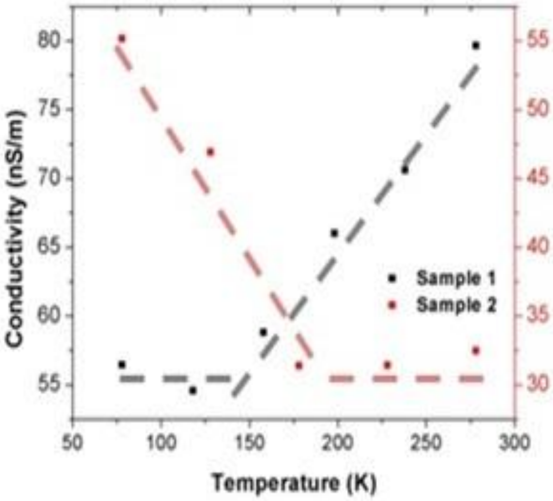

**Figure 4.7** - The temperature dependent conductivity at one volt for the 32nm (Sample 1) and 16nm (Sample 2) AuNP arrays with 52% and 54% coverages, respectively. In one, the conduction decreases with increasing temperature as expected for a metallic array (red dotted), while in another, conductivity increases with increasing temperature (black dotted) showing a thermally activated conduction process.

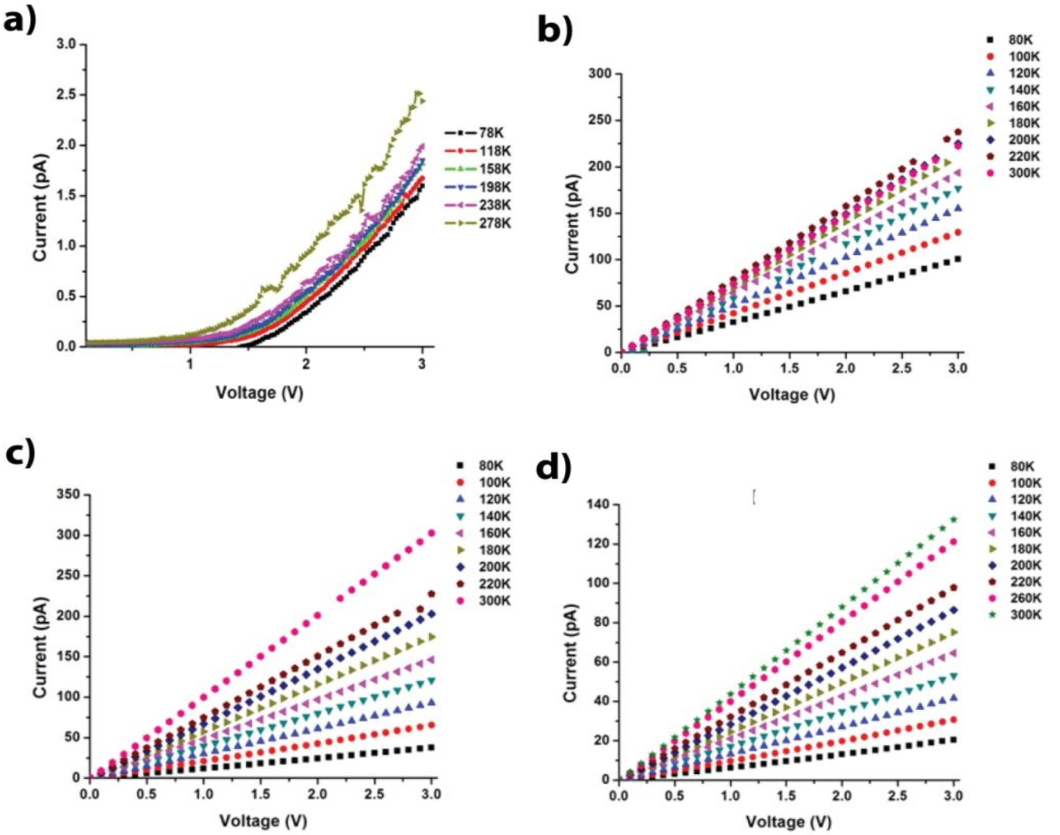

**Figure 4.8** –(a) & (b) show temperature dependent conduction of a 32nm AuNP array and 40nm/15nm bi-modal AuNP array linked with trimer molecules. (c) & (d) are temperature dependent conduction of 40nm/15nm bi-modal AuNP arrays linked with dimer and monomer molecules, respectively.

In order to isolate the properties of the hybrid devices, the AuNP arrays should not exhibit any transport in the absence of molecular linkers. The analysis will now be limited to samples that empirically were found to exhibit no current before molecular attachment; therefore, AuNP arrays similar to the 16nm sample will not be discussed further. Investigating the possible conduction mechanisms controlling the transport through the linked AuNP arrays requires a systematic protocol to determine the voltage and temperature dependencies. **Figure 4.8(a – d)** illustrates that the temperature dependence of the current depends on the specific molecule linked to the AuNP array. **Figure (a)** & **(b)** compare the conduction properties of a 32nm AuNP array and 40nm/15nm bi-modal AuNP array linked with trimer molecules with surface coverages of 54% and 70%, respectively. **Figure (b- d)** compare the conduction properties of 40nm/15nm bi-modal AuNP arrays linked with trimer, dimer and monomer molecules, respectively, and surface coverages of 70%, 61% and 63.7%, respectively. A protocol was developed to analyze the temperature and voltage dependent conductivity to determine if multiple mechanisms contribute to conduction. The voltage dependence was examined with transition voltage spectroscopy where an observed transition from direct to Fowler-Nordheim tunneling gives an approximation of the barrier height. The temperature dependent conductivity was analyzed to determine if the transport can be fit to a thermionic emission model or an activated process. If an activated process was present, the form of the temperature dependence was determined by examining the temperature dependence of the logarithmic derivative of the inverse conductance with respect to $T^{\alpha}$, where $\alpha$ was varied. The apparent activation energy was determined by a linear fit of the logarithm of the conductance as a function of inverse temperature. In addition to conventional fitting of the temperature dependent conductivity, the voltage and temperature dependence of the current-normalized differential conductance was examined to determine if multiple transport mechanisms are present.

### 4.4.2. Analysis of charge transport

**Figure 4.8** illustrates both linear (**Figure 4.8(b – d)**) and non-linear (**Figure 4.8(a)**) voltage dependencies and the temperature dependence indicates an activated behavior in all samples. Analysis of the conductivity data in **Figure 4.8** requires the examination of the voltage and temperature dependencies to determine if multiple mechanisms are present. **Figure 4.8(a)** shows a clear voltage threshold for conduction, while **Figure 4.8(b – d)** shows a near linear response. Based on studies on similar AuNP systems, the tunneling mechanisms can be categorized into either direct or Fowler-Nordheim tunneling.[32] These two mechanisms can be distinguished by a change in voltage dependencies observed with transition voltage spectroscopy.[32]

**Figure 4.9(a – d)** compares the Fowler-Nordheim plots of the conductivity data in **Figure 4.8(a – d)**, respectively. **Figure (b- d)** show no transition to Fowler-Nordheim tunneling at higher voltages across all temperatures, while **Figure (a)** exhibits a transition to Fowler-Nordheim from direct tunneling. The insert in **Figure (a)** shows the linear fits on either side of the transition. The intersection of the fit lines corresponds to the transition voltage from direct tunneling to Fowler-Nordheim tunneling. A transition voltage of 1.17V ±0.06V was found across the full temperature range. Transition voltage spectroscopy does not take into account temperature dependence, but the conductivity data in **Figure 4.8** shows that an activated transport process co-exists with tunneling. The exact nature of the temperature dependence needs to be determined.

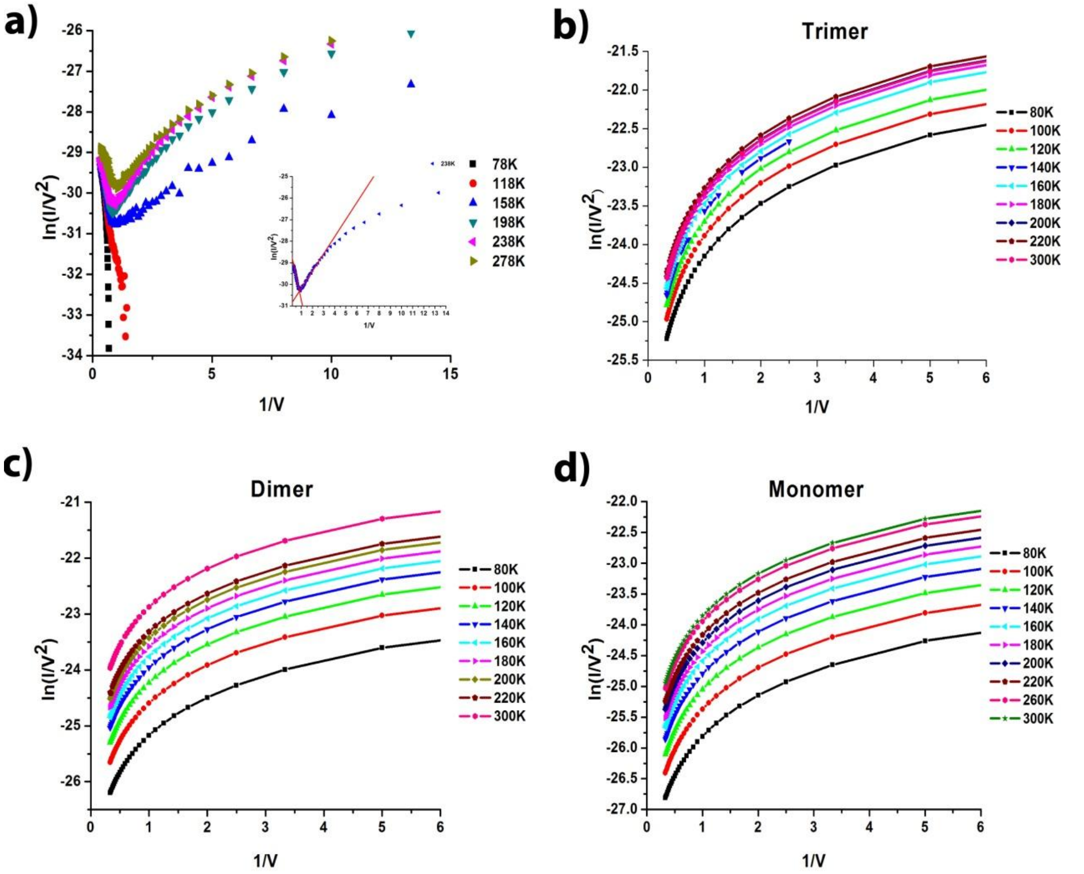

**Figure 4.9** - Fowler-Nordheim plots of the conductivity data seen in **Figure 4.8(a – d)**, respectively. (a) exhibits a transition to Fowler-Nordheim from direct tunneling. The insert of (a) shows the linear fits on either side of the transition from direct tunneling to Fowler-Nordheim tunneling showing a transition voltage of 1.17V ±0.06V. (b - d) show no transition to Fowler-Nordheim tunneling at higher voltages across all temperatures indicating only direct tunneling.

**Figure 4.10(a-d)** compares the temperature dependent conductivities of the samples in **Figure 4.8(a-d)**, respectively, to determine if the temperature dependence follows a thermionic emission model for transport. Thermionic emission can be distinguished by linearizing the conductivity data as ln(I/T$^2$) as a function of 1/kT. The slope of the relationship is proportional to the barrier height. None of the data in **Figure 4.10** exhibit a transition where ln(I/T$^2$) increases linearly with increasing temperature, hence thermionic emission is not the temperature dependent conduction mechanism. Although thermionic emission is not clearly responsible for the temperature dependence, the data still indicates an activated process.

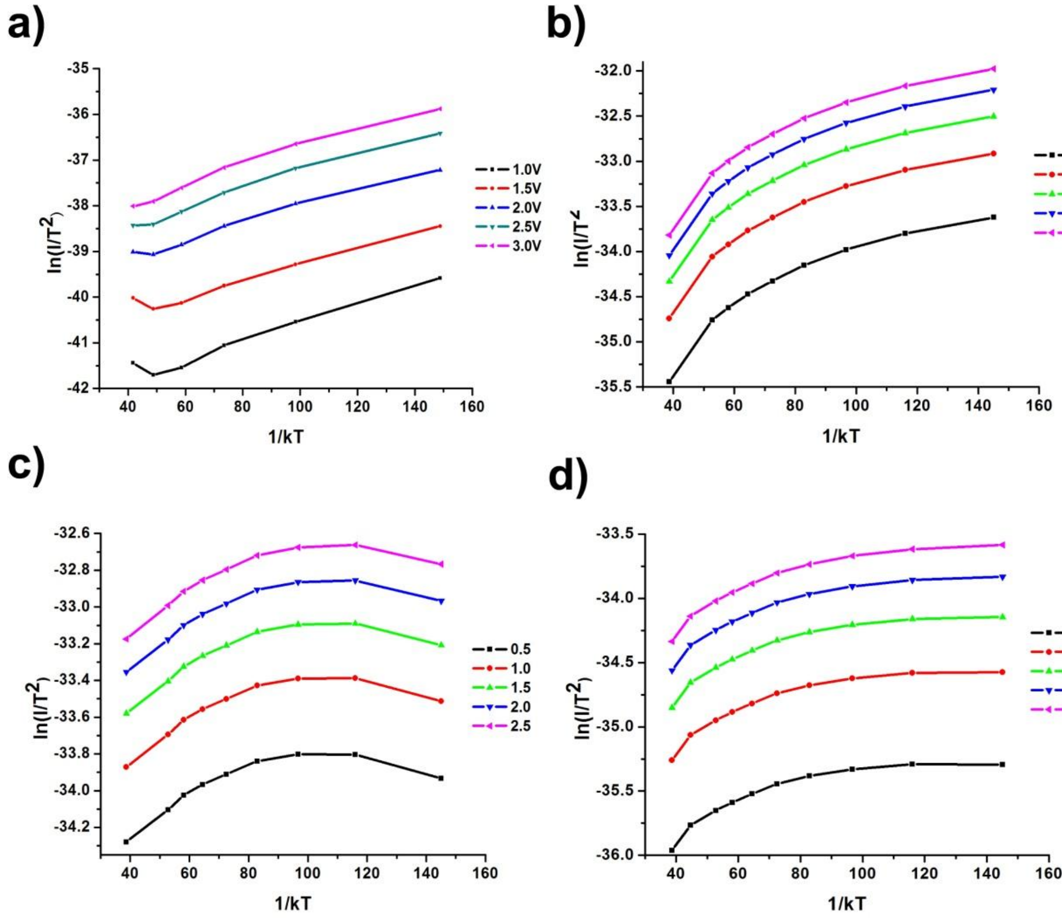

**Figure 4.10** – (a – d) show re-plots of the data in **Figure 4.8(a - d)** as ln(I/T$^2$) as a function of 1/kT, respectively. Thermionic emission can be distinguished by a region where ln(I/T$^2$) increases linearly with increasing temperature.

The current as a function of voltage in **Figure 4.8(b – d)** exhibits a finite resistance at zero bias along with thermally activated conduction. To account for this, it can be assumed that the conductance follows a simple Arrhenius law, Equation (25),

$$g = g_0 \exp\left(-{}^{\Phi}/_{kT}\right) \tag{25}$$

where $g_0$ is a prefactor, Φ is the activation energy required for transport over the potential barrier, k is the Boltzmann constant, and T is the temperature. The slope of the logarithm of the conductance, ln(g), as a function of inverse temperature, 1/kT, is the activation energy, Φ. Unfortunately, plotting the natural log of the conductance as a function of 1/T, $1/T^{0.5}$ or $1/T^{0.25}$ provides an inconclusive solution at best since the fitting of the temperature dependence to any form requires an assumption about the transport mechanisms. Heath el al have shown that the temperature dependence of the conductance for NP films exhibits a crossover from Arrhenius-like behavior with $T^{-1}$ dependence to a low-temperature variable range hopping (VRH) regime with a $T^{-1/2}$ dependence at lower temperatures. Herrmann et al and others have reported an intermediate temperature dependence that does not fit well to either the $T^{-1}$ or $T^{-1/2}$ dependence and is related to disorder in the array. To determine if the systems examined here exhibit such a crossover and/or the temperature dependence, a differential analysis of the natural log of the conductance can provide a robust description of the temperature dependence.[23] Therefore, the temperature dependence of the logarithmic derivative of $g^{-1}(T)$ with respect to $T^{-\alpha}$ was examined to demonstrate the functional form controlling the temperature dependence.

If the temperature dependent conductance follows Equation (26) over a specific temperature range, then $d\ln(g^{-1})/dT^{-\alpha}$ should be constant in that region. **Figure 4.11(a –**

**d)** show dln($g^{-1}$)/d$T^{-\alpha}$ as a function of temperature for α=1, 0.8, and 0.5, of the conductivity data in **Figure 4.8(a –d)**, respectively. **Figure 4.11(a)** & **(b)** which have trimer molecules attached to the AuNP arrays show the best fit with α=1 and α=0.88, respectively. **Figure (c)** & **(d)** represents AuNP arrays linked with dimers and monomers and fit to α=1.0 and α=0.5, respectively.

$$g(T) = g^{*}\exp\ -(T^{*}/T)^{\alpha} \tag{26}$$

**Figure 4.12** shows dln($g^{-1}$)/d$T^{-\alpha}$ as a function of temperature for a variety of AuNP assemblies. **Figure 4.12(a)** plots dln($g^{-1}$)/d$T^{-1}$ as a function of temperature of the conductivity data in **Figure 4.8(a)** for various applied voltages. **Figure 4.12(b)** shows several trimer linked AuNP arrays that exhibit a linear conductivity response similar to that seen in **Figure 4.8(b)**. Each AuNP array is plotted for the best fit of α as a function of inverse temperature with α found to range from -1 to -0.75. The figure also indicates a transition region from 160-200K, regardless of the temperature dependence, that indicates a transition from the activated region at lower temperature to metallic-like transport above the transition region.

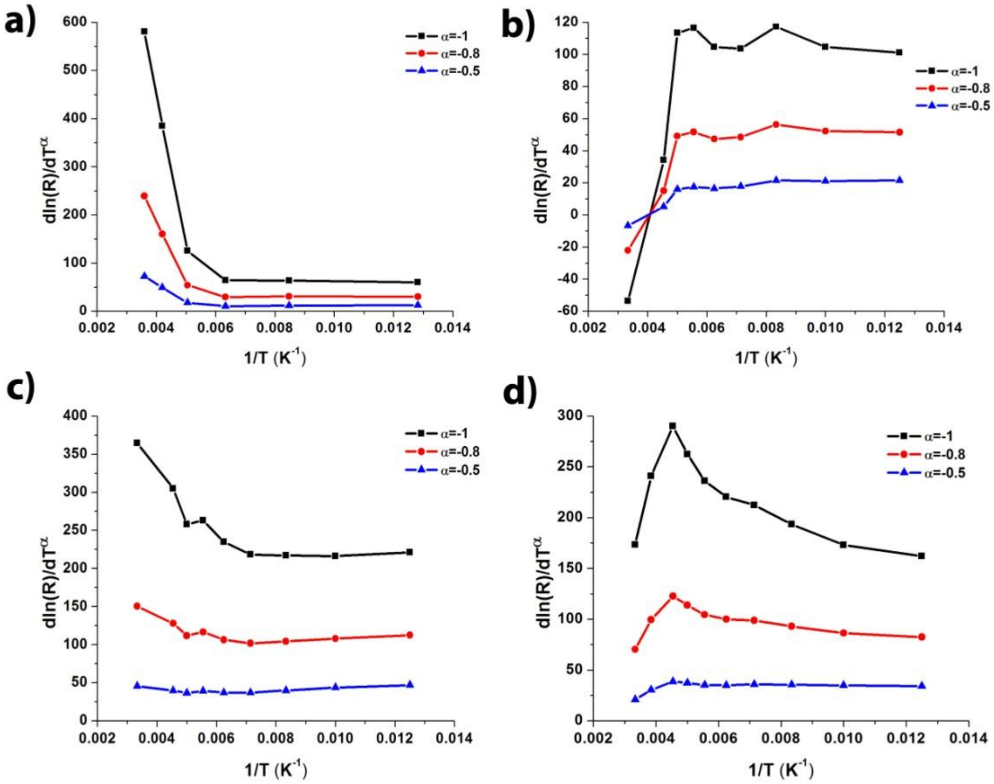

**Figure 4.11** - $d\ln(g^{-1})/dT^{-\alpha}$ as a function of temperature for $\alpha$=1, 0.8, and 0.5, of the conductivity data seen in **Figure 4.8(a – d)**, respectively. (a) & (b) have trimer molecules attached to the AuNP arrays and are best fit with $\alpha$=1 and $\alpha$=0.88. **(**c) & (d) represent AuNP arrays linked with dimers and monomers and best fit to $\alpha$=1.0 and $\alpha$=0.5, respectively. The best fit was determined by comparing the linear fit of the data below ~200K for each value of $\alpha$. The $\alpha$ that results in the linear fit slope being closest to zero was defined as the best fit.

**Figure 4.12(c)** & **(d)** show several dimer and monomer linked AuNP arrays that exhibit linear conductivity similar to that seen in **Figure 4.8(c)** & **(d)**, respectively. As in **Figure 4.12(b)**, $d\ln(g^{-1})/dT^{-\alpha}$ is plotted for the best fit of $\alpha$ as a function of inverse temperature with $\alpha$ found to ranges from -1 to -0.5 and from -0.85 to -0.5 for the dimer and monomer, respectively. The temperature dependence of AuNP arrays linked with dimer molecules are found to exhibit either a $T^{-1}$ or $T^{-0.5}$ dependence, and do not exhibit an extended temperature range in which one dependence can describe the transport. The majority of monomer linked AuNP arrays fit best to $T^{-0.8}$. The dimer and monomer linked AuNP arrays show a similar transition region between approximately 150K and 200K from an activated process at lower temperature to another mechanism at higher temperatures. This variability in the temperature dependence could be an indication of the degree of disorder and/or charging in the AuNP arrays, as has been shown in other more highly ordered systems.[91, 92] For this study, we will assume that $T^{-1}$ describes the transport with any variation arising from the degree of disorder.

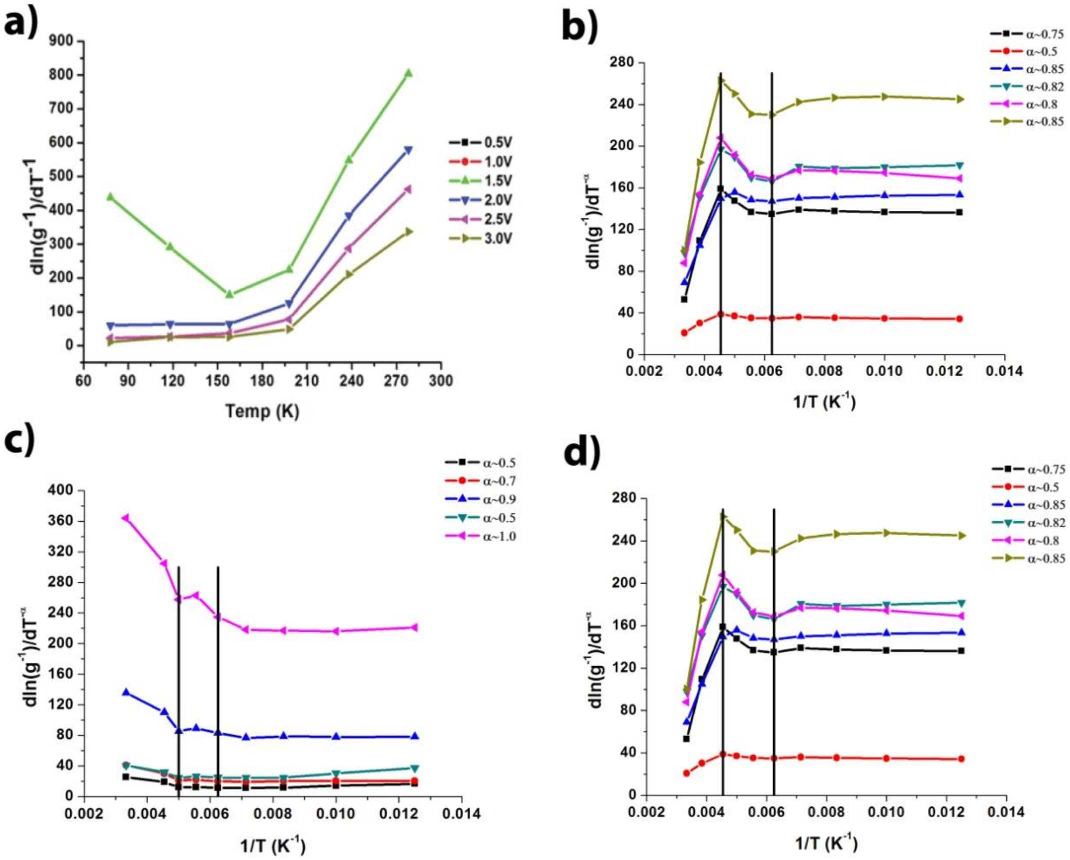

**Figure 4.12** - $d\ln(g^{-1})/dT^{-\alpha}$ is plotted for the best fit of α as a function of inverse temperature. (a) for various applied biases from the data in **Figure 4.8(a)**. (b) for trimer linked AuNP arrays that exhibit a linear conductivity response similar to that seen in **Figure 4.8(b)**. (c) & (d) for dimer and monomer linked AuNP arrays that exhibit a linear conductivity response similar to that seen in **Figure 4.8(c)** & **(d)**, respectively.

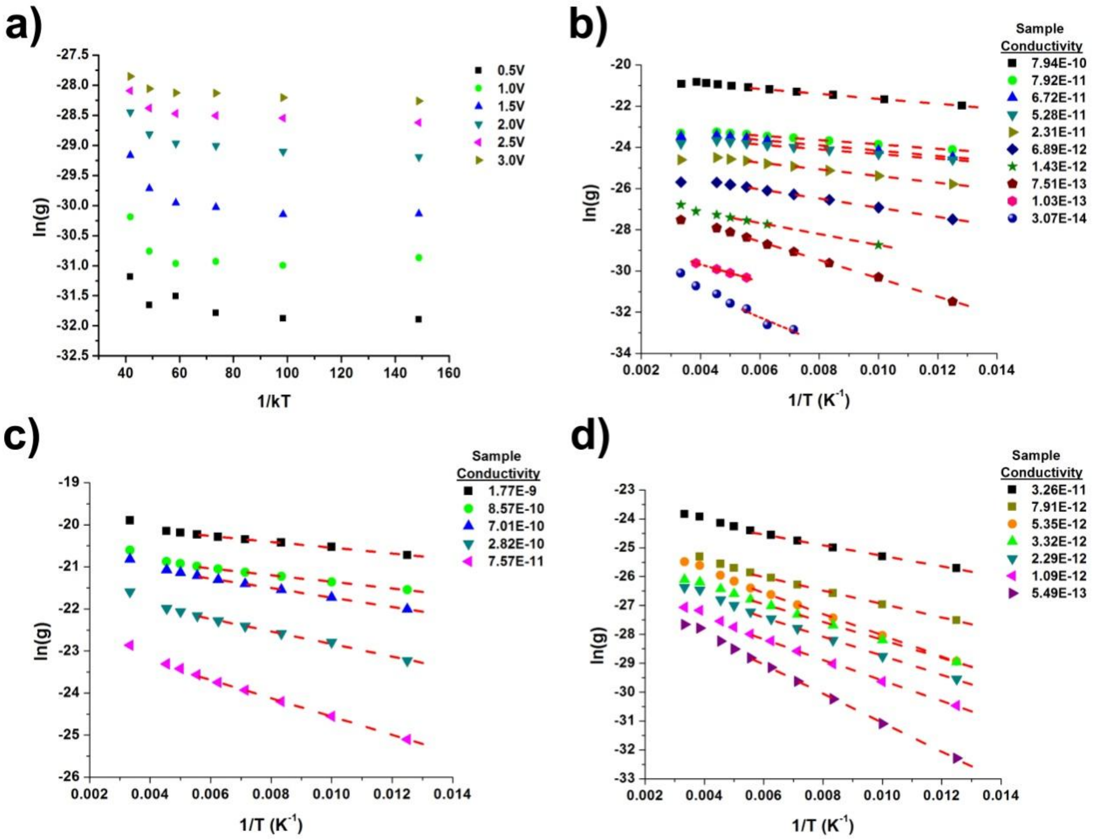

**Figure 4.13** – Natural logarithm of the conductance as a function of the inverse temperature. (a) the temperature dependent conductivity data in **Figure 4.8(a).** (b - d) are for various AuNP arrays linked with trimer, dimer and monomer molecules, respectively, that exhibit a near linear conductivity response similar to **Figure 4.8(b-d)**, respectively. The red dotted lines are linear fits of the data below 200K.

With the temperature dependence determined to be independent of the molecular attachment and particle size distribution, the natural log of the conductance can be plotted as a function of the inverse temperature to obtain an apparent activation energy for the arrays represented in **Figure 4.12**. **Figure 4.13(a)** is an Arrhenius plot of the data in **Figure 4.8(a)**, which exhibits temperature independent conductance below 200K and a voltage dependence with a transition between 1V and 1.5V above 200K. Below 1V, the data exhibits a larger apparent activation energy then above 1V. **Figure 4.13(b)** & **(d)** show that the transport exhibits activated behavior below 250K and a transition to metallic like transport above 250K, where the conductance decreases with increasing temperature. **Figure 4.13(c)** shows that the transport exhibits activated behavior through the whole temperature range for samples with dimer linkers.

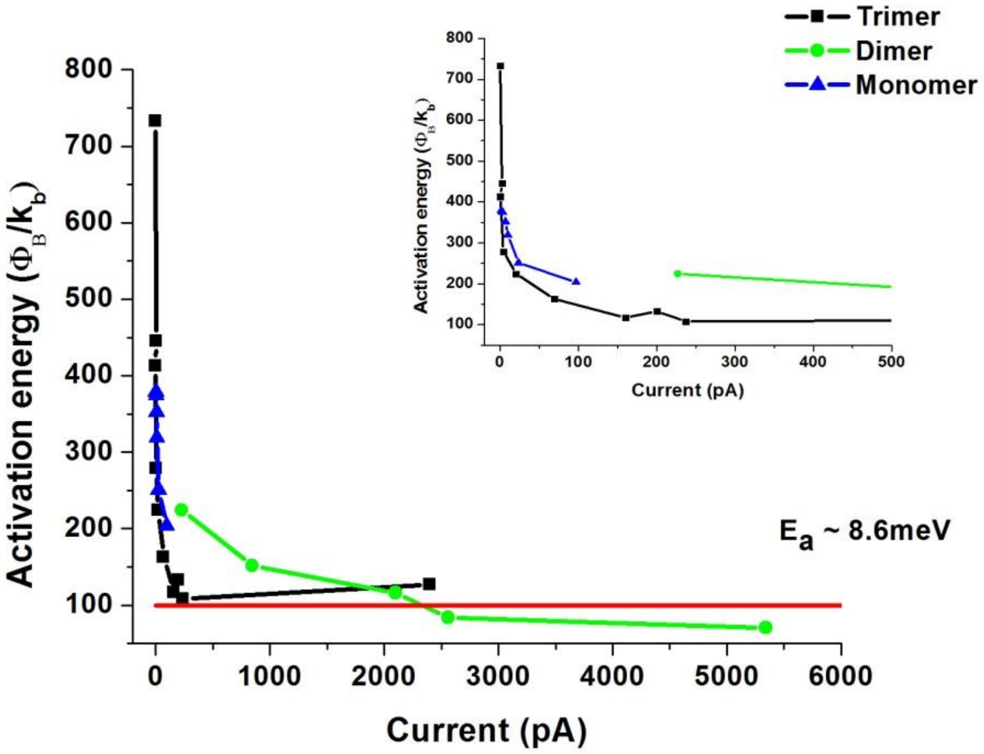

**Figure 4.14** – The activation energies as a function of the current at 220K for AuNP linked with trimer (black), dimer (green), and monomer (blue) molecules. All samples, regardless of linker molecule or AuNP size distribution, exhibit a decrease in activation energy with increasing conductance until it reaches a threshold value, approximately at 8.6 meV.

A linear fit of the activated regime (below 200K) in **Figure 4.13** allows the apparent activation energies (proportional to the slope) of the barrier to transport to be determined. The samples in **Figures 4.13** are plotted in the order of decreasing conductance and exhibit a change in activation energy as a function of conductivity, which can be seen more clearly in **Figures 4.14,** where the slopes of the linear fits in **Figure 4.13** are plotted as a function of current at 220K. This temperature was chosen to compare apparent activation energies since it was the highest temperature at which all samples showed activated transport. **Figure 4.14** shows that the activation energies decreases with increasing conductivity and saturates after reaching a threshold, independent of the linker molecule. The activation energy for the trimer, dimer and monomer linked arrays appears to be approximately 8.6meV ± 3.6meV (red line), with the inset showing a zoomed in view of the data below 500pA.

Murray et al have studied of transport through metal nanoparticle assemblies and shown that the general form of the conductance is Equation (27), where the first term is related to tunneling between particle and the second term describes the activated transport describe above.[93, 94]

$$g(T) = g^o \exp(-\beta l) \exp\ -(T^o/T)^\alpha \tag{27}$$

In Equation (27), $g^o$ is a prefactor, while the second term is a tunneling component to the transport, where $\beta$ is a decay constant and $l$ is the tunneling distance between particles and the last term is related to an activated hopping process, with $T^o$ being a constant, $T$ is the temperature and $\alpha$ is the exponent related to the temperature dependence.[91, 93] The tunneling component should exhibit nominal temperature dependence, but the pre-exponential factor is shown to have a correlation with $T^o$ for a large number of organic semiconductors.[95, 96] A differential analysis of the log of the current can provide an understanding of the voltage dependence and any temperature dependence that is not independent of the applied voltage. Plotting dln(I)/dV as a function of T will reveal any change in the temperature dependence as a function of voltage.

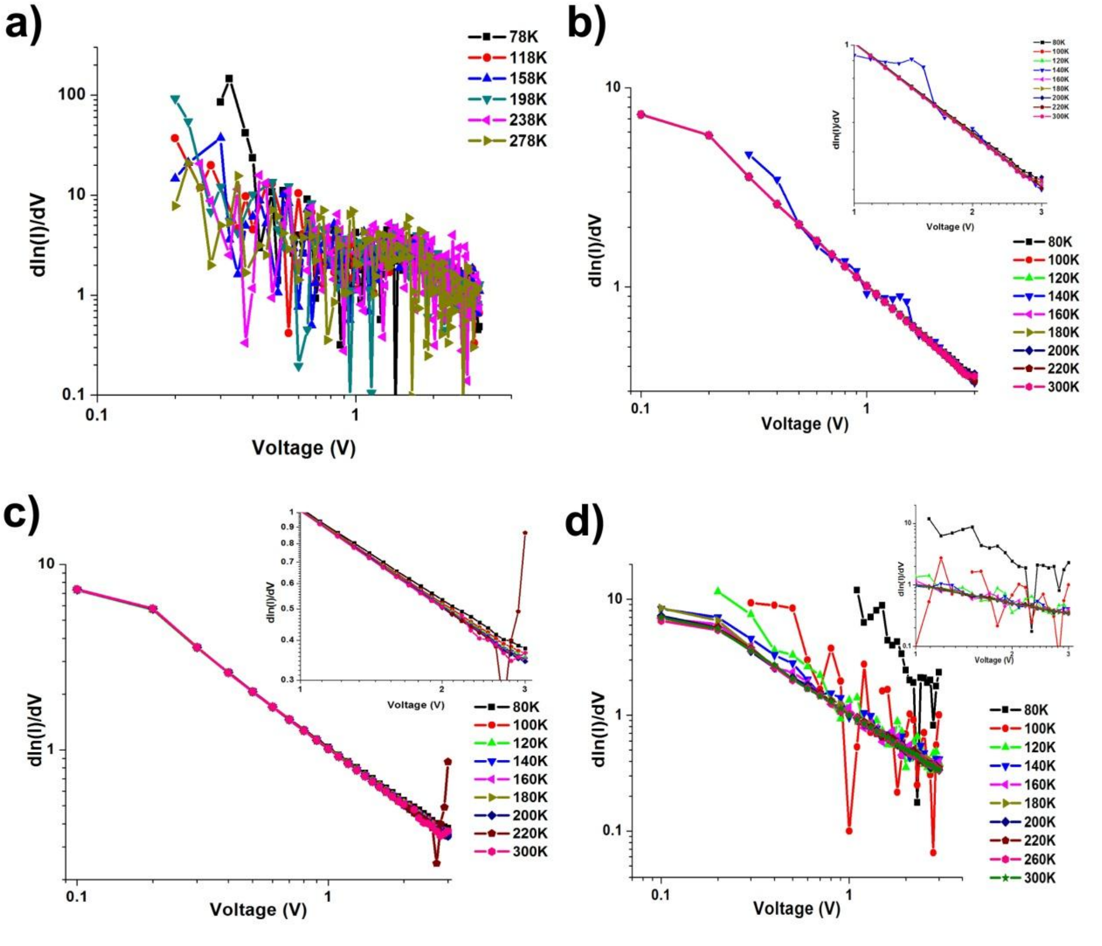

**Figure 4.15 -** (a –d) show the temperature dependent dlog(I)/dV as a function of voltage for the conductivity data in **Figure 4.8(a – d)**, respectively. The inserts in (b – d) show plots of the data above 1V.

**Figure 4.15(a – d)** shows the dln(I)/dV as a function of voltage for the conductivity plots in **Figure 4.8(a – d)**, respectively. **Figure 4.15(a)** exhibits a linear voltage response below 1V and exhibits nominal temperature dependence. **Figure 4.15(b** – **d)** exhibit near-linear voltage responses, as expected from the conductivity data, and an examination of the voltage dependence above 1V (inserts) shows a slight temperature dependence as well. **Figure 4.16** plots dln(I)/dV as a function of temperature for the samples with near-linear behavior in **Figure 4.15**. **Figure 4.16(a)** compares a low conductivity and high conductivity AuNP array linked with trimer molecules. Both AuNP arrays exhibit constant temperature dependence above 150K, but the lower conductivity device exhibits a larger change in the temperature dependence compared to the more conductive device below 150K. **Figure 4.16(b)** compares dlog(I)/dV as a function of temperature for a AuNP array linked with trimer molecules and an array linked with dimer molecules. The samples had approximately the same conductance at 220K and the same bimodal distribution of AuNPs. The plot shows that the dimer linked AuNP array exhibits a larger temperature dependence change than does the trimer linked AuNP array. This phenomenon can also be seen in **Figure 4.16(c)** where a AuNP array linked with trimer molecules is compared to an array linked with monomers. The monomer linked AuNP array shows a larger change in temperature dependence below 150K than does the trimer linked array, while the dependence in the higher temperature regime remains constant. It is found, in general, that when comparing samples of similar conductivity that the observed change in temperature dependence decreases with increasing molecular linker length.

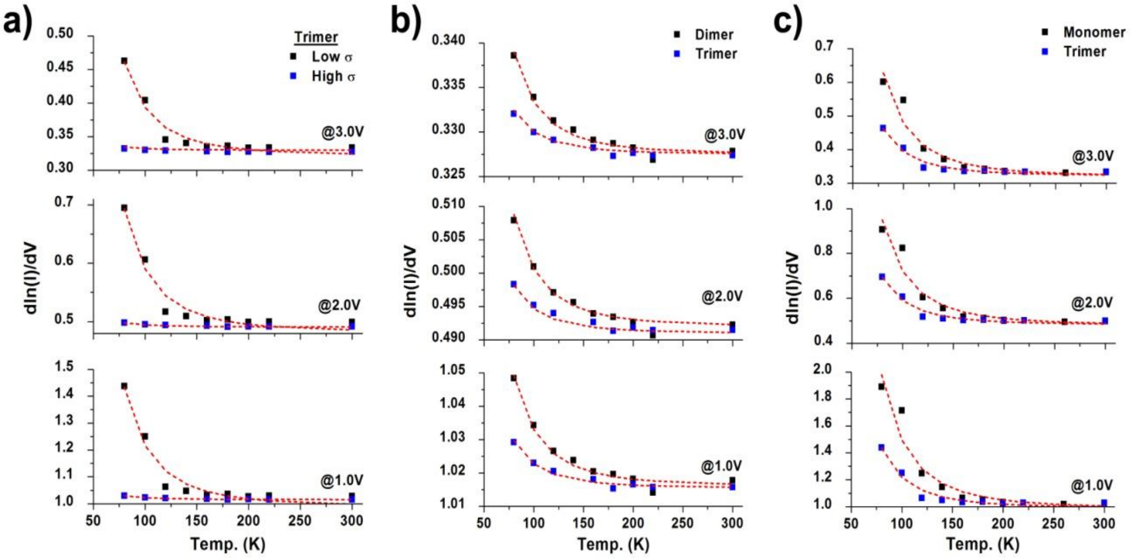

**Figure 4.16** - dln(I)/dV as a function of temperature. (a) comparison of a low conductivity and high conductivity AuNP array linked with trimer molecules. (b) comparison of a AuNP array linked with trimer molecules and an array linked with dimer molecules. (c) comparison of a AuNP array linked with trimer molecules with an array linked with monomers. (b) & (c) compare AuNP linked arrays of similar conductivity.

The observed temperature dependence in the analysis of dln(I)/dV provides insight into the possible transport mechanisms. When the barrier to transport is very thin, as is the case with our linker molecules, tunneling and thermionic emission (Schottky) are generally regarded as the two potential dominate conduction mechanisms. Clearly thermionic emission is strongly dependent on the barrier height and temperature, thus is easily distinguished from a direct tunneling mechanism. The Poole-Frenkel effect, where the electric field assists thermal ionization of trapped charge carriers, and thermionic emission (Schottky), where the electric field lowers the barrier height, results in the same functional form of the temperature dependence. The observation of a transition to Fowler-Nordheim tunneling in the non-linear case gives support to the presence of a tunneling mechanism, but the observation of the strong temperature dependence in the near-linear cases suggests various hopping models.

As discussed in Section 2.4.1, this ambiguity can be addressed with the current normalized differential conductance which simplifies the transport equations and reduces the number of fitting parameters. Comparing the equations in Section 2.1.3 and **Figure 4.16**, the non-linear dependence of dln(I)/dV on temperature discounts Poole-Frenkel and thermionic emission, since both of these models result in an inverse temperature dependence. The observed non-linear trend can be explained by fitting the data to a thermally assisted tunneling model. This model has been developed and discussed by Roberts & Polanco and an analysis of the entire emission phenomena has been performed by Murhpy & Good.[97-99] This mechanism involves tunneling through potential barriers, and the systems studied here involve tunneling through a series of potential barriers. The product of the tunneling probabilities included in the conductivity expression results in the extremely low conductivity observed in the data. Roberts and Polanco have shown that for appropriate parameters, thermally assisted tunneling can yield the current dependence on voltage with the form of thermionic emission or Poole-Frenkel effects[98]. The thermally assisted tunneling model describes the situation in which the major contribution to the tunneling integral does not come from the region of the Fermi level but from an energy level located some position above the Fermi level. At the same time, this tunneling mechanism dominates over the thermal electron transfer process that occurs at energy levels above the height of the barrier. Since the main contribution to thermally assisted tunneling comes from energies that are above the Fermi energy, this makes the effective and measured barrier height smaller than the actual barrier to transport.

The analysis by Murphy and Good is an extension of the Richardson-Schottky and the Fowler-Nordheim models.[99] With appropriate boundary conditions, an analytical solution for the functional form of thermionic emission (Schottky) and field emission (Fowler-Nordheim) for the total current density can be obtained. Within this frame work, a transition regime can be developed to describe transport when both thermionic and field emissions are present. Equation (28) is the functional form of this intermediate regime (also seen Section 2.1.3.), where $\Theta=2t(y)^{-2}-2\upsilon(y)t(y)^{-3}$ and the other arguments have been defined in Section 2.1.3.

$$I = \frac{E}{2\pi}\left(\frac{kTt(y)}{2\pi}\right)^{1/2} exp\left(-\frac{\emptyset}{kT}+\frac{E^2\Theta}{24(kT)^3}\right) \tag{28}$$

The arguments $\upsilon(y)$ and $t(y)$ are elliptic functions that are related to the applied voltage and the barrier height. The logarithmic derivative of the current with respect to voltage produces the relationship seen in Equation (29).

$$\frac{dlnI}{dE} = E^{-1} + \left(\frac{E\Theta}{12(kT)^3}\right) \tag{29}$$

The dotted red lines in **Figure 4.16** are best fit lines to the functional form in Equation (29) and are in good agreement with the data. The variation between samples is a function of Θ in Equation (29). This term is found to be a function of applied field, and the unreduced barrier height. Assuming that the analysis of logarithmic derivative provides proof that thermally assisted tunneling can describe the transport, the functional form of the current as a function of voltage should fit our data. The samples that exhibit near-linear conductivity fit very well to the functional form for thermally assisted tunneling in Equation (28).

In further prove of the robust nature of this analysis, dln(I)/dV as a function of temperature for the sample that exhibit nominal temperature dependence (non-linear conductivity response) does not fit well to the thermally assisted tunneling function (Equation (28)). This is somewhat expected since the Fowler-Nordheim plot shows a transition from direct tunneling to field emission and the conductivity data in this case can be fit to the functional form for field emission. But the conductivity data exhibit temperature dependence; therefore the conventional Fowler-Nordheim formula for field emission does not fully describe the data. This inconsistency for the case of non-linear transport can be described in the model by assuming a thin potential barrier at the interface between the molecule and the AuNP's. The voltage drop would occur across the AuNP surface and the boundary layer according to the resistance of each component.

Although the work function of the nanoparticles with chemisorbed porphyrins is not known, comparison of the extracted value of Θ from the fits in **Figure 4.16** and the activation energies as a function of conductive provide useful insight. As noted above, Θ is a function of the applied field and the barrier height. The term Θ is a function of *v* and *t*, which are mathematical definitions that depend on only the Nordheim parameter, *y*.[100] The fit of Equation (29) to our data yields Θ in the range of $1.34\text{x}10^{-8}$ to $3.69\text{x}10^{-7}$, which corresponds to the case of a small number of active junctions and barrier heights similar in magnitude to those obtained from Arrhenius analysis (10-30meV). The Θ determined from the measurements increases as a function of molecular length, which can be understood as a decrease in the local electric field due to the increased particle separation. Similarly, an observed increase in Θ as a function of decreasing conductivity is consistent with a decrease in the apparent barrier height expected for higher molecular surface coverage.

### 4.4.3. Mechanisms of charge transport

The analysis of the dark conductivity data shows that the transport results from thermally assisted tunneling at most temperature in arrays exhibiting near-linear current-voltage responses and from Fowler-Nordheim tunneling at low temperatures with multiple mechanisms at higher temperatures in arrays exhibiting non-linear current-voltage behavior. The parameters that dictate the ultimate current magnitude are the particle work function, molecular surface coverage, and particle separation. Note that the "apparent activation energy" is directly related to the work function if all other variables are considered equal. There is considerable variation in this apparent work function, but it increases monotonically with the sample conductance, saturating at a maximum value. If the conductance variations were caused by variations in the number of transport paths across arrays with the same interfacial barriers, the "apparent activation energy" would not vary with conductance. If, however, the variations were caused by variations in the porphyrin surface coverage, then the observed dependence on conductance would manifest. There is a vast amount of literature on the effects of the adsorption of organic compounds on the work function of metals and it invariably decreases the work function.[32, 101, 102] In our case, increased porphyrin coverage would lower the work function and increase the overall conductance, and furthermore, saturation would occur at complete coverage. For this reason the variation in the activation energy was attributed to the extent of the surface coverage of the molecule on the AuNP and all analyses of mechanism were carried out on samples with similar conductivities ensuring that the work functions were likewise similar.

The transport mechanisms in the hybrid nanoparticle arrays can be explained in terms of the band diagrams in **Figures 4.17**, **4.18**, & **4.19**. **Figure 4.17** shows a proposed band structure of the porphyrin linked AuNPs. Zangmeister et al have studied 4,4'-(ethynylphenyl)-1-benzenethiol (OPE) self-assembled monolayers (SAMs) on gold surfaces, which although not a dithiol, can provide insight into the barriers to transport associated with the Au-S bonds and phenyl-ethyene linker groups attaching the zinc-porphyrins on the AuNPs in this study.[101, 102]. The gold-sulfur interaction extends the binding energy from the Fermi level of the gold to 1eV below this level.[102] This bond also produces levels closer to the Fermi level, which are localized at the interface with limited extent into the molecular gap.[102] The work function of the gold surface with a OPE monolayer is 4.2eV, which is approximately 0.6eV lower than a bare gold surface.[102] The highest occupied level (HOMO) and lowest unoccupied level (LUMO) of the phenyl-ethyene bridge located 1.9eV below and 2.5eV above the Fermi level, respectively. Susumu et al have shown the band gap of conjugated (porphinato)zinc oligomers through potentiometrically determined HOMO and LUMO energy levels to be approximately 1.5eV.[103] The energy levels were also found to vary little with increasing conjugation length.[103] The band diagram in **Figure 4.17** is from estimates based on other studies of similar molecules. The range between the exciton energy and the delocalized band gives an uncertain in the actual transport band gap.

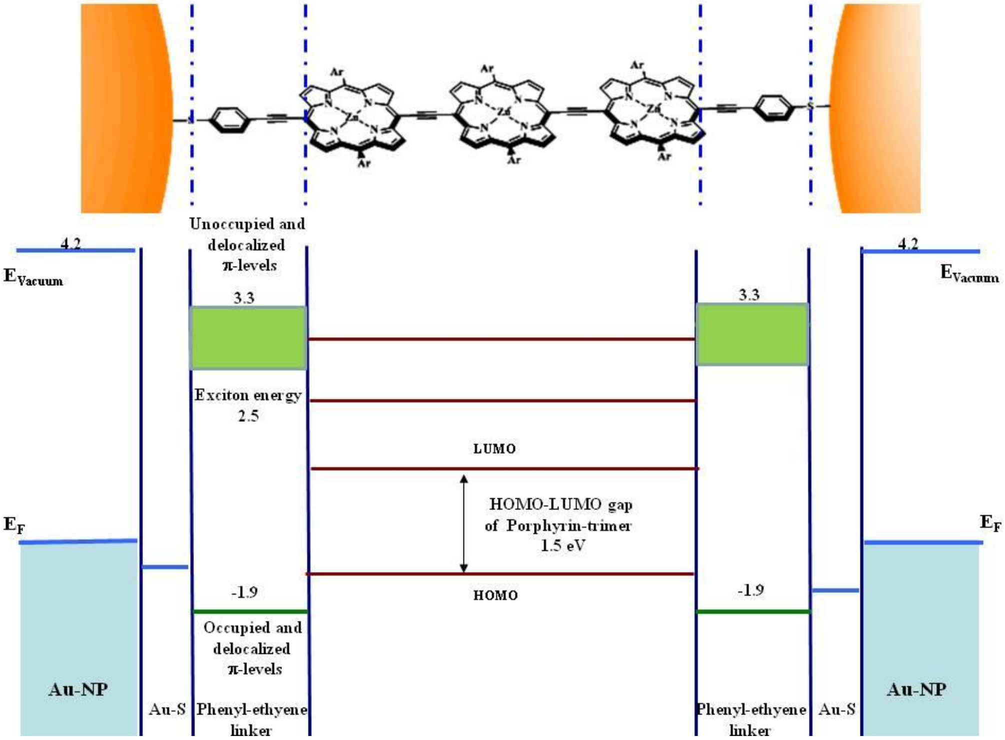

**Figure 4.17** - Proposed band structure of zinc-porphyrin linked AuNPs.

As noted above, the case of a near-linear conductivity response, where thermally assisted tunneling is the dominate transport mechanism, Θ is a function of the applied field and barrier height.[104] The increase in Θ as a function of molecular length can be understood as the decrease in the electric field as a result of an increased molecular length. The increase in Θ as a function of decreasing conductivity can be described as an increase in the apparent barrier height as a function of the extent of the surface coverage on the AuNP. These two phenomena can be examined in **Figure 4.18**, which shows an idealized band diagram as a function of molecular length. **Figure 4.18(a)** is the flat band condition, where the $E_f$ is the Fermi energy of the AuNPs in relation to the HOMO-LUMO levels of the zinc-porphyrin supermolecule. $E_a$ is the energy at some level above the Fermi level in which thermally assisted tunneling occurs. **Figure 4.18(b-d)** shows the case for the monomer, dimer, and trimer, respectively with an applied voltage across the junction. Comparing **Figure 4.18(b-d)** illustrates that as the molecular length increases, the field decreases due to the length over which the bias is applied. The variation due to the conductivity can be understood by a change in the barrier height due to degree of surface coverage, which would be reflected in the position $E_a$ related to the Fermi energy. As the molecular coverage decreases, the energy level associated with thermally assisted tunneling ($E_a$) approaches the Fermi energy. The Arrhenius plots show that when the surface coverage of the molecules on the AuNPs is saturated, and the apparent activation energy does not change with conductivity, with an apparent activation energy of 8.6meV, regardless of the attached molecule. This energy represents the energy from $E_a$ to the top of the barrier, as such; thermally assisted tunneling grossly underestimates the true barrier height.

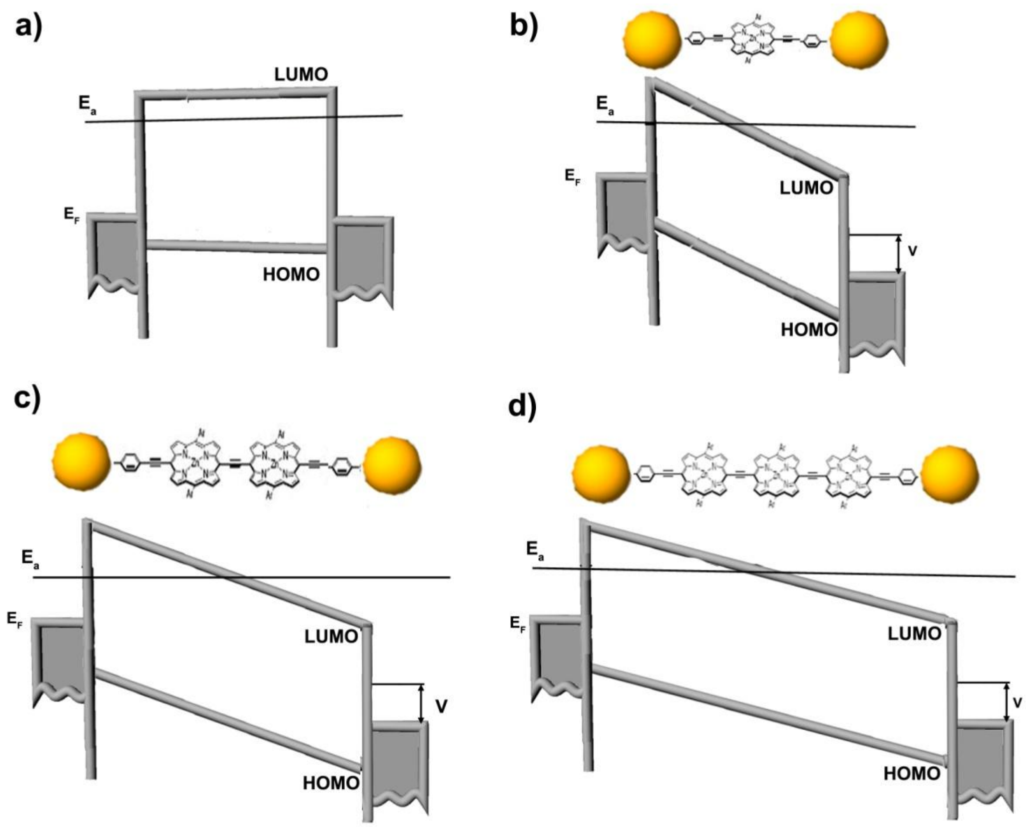

**Figure 4.18** – Idealized band diagram as a function of molecular length for AuNP arrays with near linear conductivity response. (a) shows the flat band condition, where the $E_f$ is the Fermi energy of the AuNPs in relation to the HOMO-LUMO levels of the zinc-porphyrin supermolecule. $E_a$ is the energy at some level above the Fermi level in which thermally assisted tunneling occurs. (b-d) shows the case for the monomer, dimer, and trimer, respectively with an applied voltage across the junction.

In the case of the non-linear conductivity response, the voltage dependence exhibits a clear transition from direct tunneling at low biases to field emission (Fowler-Nordheim) at higher biases. The apparent barrier height is 1.17eV across the full temperature range, but Fowler-Nordheim transport does not include temperature dependence, whereas the conductivity data does exhibits weak temperature dependence. Applying a thermionic emission model and examining an Arrhenius plot of the conductivity data indicates temperature dependence above 200K. Examining **Figure 4.10(a)** & **4.13(a)** above 200K shows that below 1.5V, that the apparent activation energy is larger and voltage dependent whereas above 1.5V exhibits smaller activation energies that are voltage independent. This indicates that field emission does not fully describe the transport mechanism.

With reference to the linear conductivity response, the transport is thermally assisted tunneling with the non-linear effects resulting from a thin potential barrier at the interface between the molecule and the AuNPs.[97] **Figure 4.19** shows an idealized band diagram for the non-linear case, where an additional barrier has been added between the molecule and the AuNPs. Assuming that thermally assisted tunneling is still present as a transport mechanism; the major contribution to the tunneling current once again comes from some level above the Fermi level.[97] Unlike the previous case though, the introduction of the additional barrier results in the transport being dominated by traditional field emission characteristics. This can be observed in **Figure 4.19**, where **(a)** is the flat band condition, while **(b)** & **(c)** are at low and high applied biases, respectively. It shows that at low biases, **Figure 4.19(b)**, that the direct tunneling through the additional barrier is the dominating the transport. At high biases, **Figure 4.19(c)**, the transport is field emission but now it is tunneling through two barriers that can be modeled as thermally assisted tunneling.

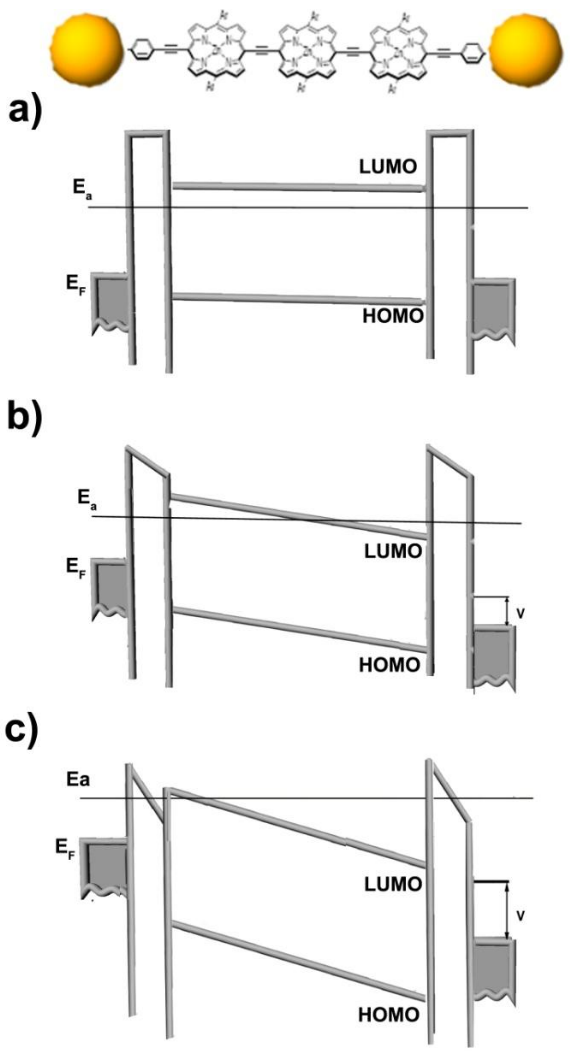

**Figure 4.19** – Idealized band diagram as a function of molecular length for AuNP arrays with non-linear conductivity response. (a) shows the flat band condition, where the $E_f$ is the Fermi energy of the AuNPs in relation to the HOMO-LUMO levels of the zinc-porphyrin supermolecule. $E_a$ is the energy at some level above the Fermi level in which thermally assisted tunneling occurs. (b) & (c) show the low and high bias regimes, respectively, with an applied voltage across the junction.

As discussed in Section 4.3, the AuNP arrays are a platform to study photocurrent in hybrid devices, therefore understanding the interaction of light with the AuNP assemblies needs to be determined to tune the opto-electrical response. The immersion time provides empirical control of the particle separation, which as discussed above, can be manipulated to produce a wide range of transport behavior. Independently, the immersion time can empirically control the particle size distribution & coupling, where the actual coupling will depend not only on the size and particle separation, but also on the degree of aggregation. As mentioned in Section 2.1.4., the absorbance due to the plasmons in AuNP arrays is dependent on the particle size & coupling and the optical absorption confirms the degree of coupling in the nanoparticle arrays. Since surface plasmons may affect opto-electronic properties, determining the effects of incident light for the various conductivity responses can result in an understanding the origins of photoconduction in these systems. The effects of incident light on the temperature and voltage dependencies can bring insight into the possible origins such as hot electrons, plasmon enhanced photoconduction, and field-induced ballistic emission.

### 4.5. Wavelength dependent photoconductivity

The temperature dependent conductance in the previous section was extended to determine the origins of photoconductivity in these systems. Current-voltage plots were obtained when no light was incident on the sample, while wavelength dependent current-voltage plots were obtained by exposing the device area with 405nm (blue), 532nm (green), and 655nm (red) light from laser diodes. Remarkable differences are observed in the photocurrent responses for the non-linear and near-linear conductivity behavior as a function of excitation wavelength. Since neither the conductivity nor photoresponse manifests in AuNP arrays in the absence of the dithiol-$PZn_x$, the photocurrent must be derived from the optical interactions with the attached molecules. If the magnitude of the photocurrent depended only upon production of the electronically excited singlet state of the AuNP-to-AuNP linker, the measured photoconductivity should track with the magnitude of the wavelength-dependent absorptive extinction coefficient. It has been shown that a thiol-to-Au bond does not substantially alter the electronic structure of a wide range of adsorbed molecules, therefore, molecular photoconductivity should be proportional to the absorption at the relevant wavelengths.[105] This implies that (in reference to the absorbance of the dithiol-$PZn_3$ in **Figure 2.15**), that there should be a low photoconductivity response with red and green light and 3-4 times higher for blue light. To understand the observed photocurrent for the illumination with various wavelengths of light, it is important to consider the effects of the incident light on the linker molecules and AuNPs to differentiate between such effects as hot electrons, plasmon enhanced photoconduction and absorption by the molecule. These mechanisms can be determined by comparing the photoconductance with variations in the transport behavior, such as changes in the barrier heights, temperature dependence, and optical response. Samples exhibited a range of photoconductance behavior. In the following section, the cases of AuNP arrays with non-linear and near-linear dark conductivity will be considered separately and the effects of molecular length, excitation wavelength, and photon flux will be considered. The effects of illumination of current transport mechanisms, and especially the factors that influence those mechanisms will be determined.

**Figure 4.20** shows the photoconductivity plot at 198K of the 32nm sample of which the dark current is shown in **Figure 4.8(a)**. The current enhancement, which is the difference in current between while exposed to light and the dark current ($\Delta I_\lambda$) is seen in **Figure 4.21(a)** & **(b)** for low and high biases, respectively. **Figures 4.20** illustrates that the current upon illumination with red light ($\Delta I_{Red}$) shows a larger increase in current than that on illumination with green or blue light ($\Delta I_{Green}$ or $\Delta I_{Blue}$). **Figure 4.21(a)** & **(b)** show that $\Delta I_{Red}$ is 2-6 times larger than $\Delta I_{Green}$ or $\Delta I_{Blue}$ at 1V & 2.5V, respectively, and over a broad range of temperatures. As discussed above, the molecular photoconductivity should be proportional to the absorption extinction coefficients at the relevant wavelengths if the photocurrent depended only upon production of the electronically excited singlet state. The anomalously large photocurrent observed for the illumination with 655nm light implies that another process is dominating the observed photocurrent enhancement. **Figure 4.21(c)** & **(d)** show current enhancements as a function of the photo flux (as described in Section 2.7.3) at 1V & 2.5V, respectively, and over a broad range of temperatures. If the photocurrent was proportional to the number of incident photons, then a linear relationship between the current enhancement and photon flux should be expected. **Figure 4.21(c)** & **(d)** does not exhibit a linear increase in photoconduction with photon flux, nor does the data show a linear increase when corrected for the absorption coefficient at the relevant wavelength (inserts in **Figure 4.21(c)** & **(d)**).

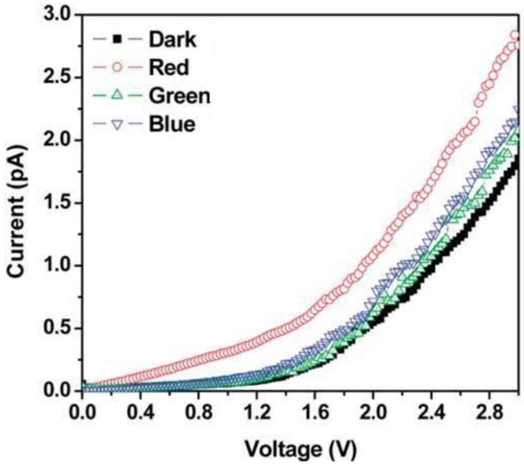

**Figure 4.20** – Wavelength dependent conduction at 198K of the 32nm AuNP array in **Figure 4.1(b)**. The sample was illuminated with red, green and blue laser diodes at 655nm, 532nm, and 405nm.

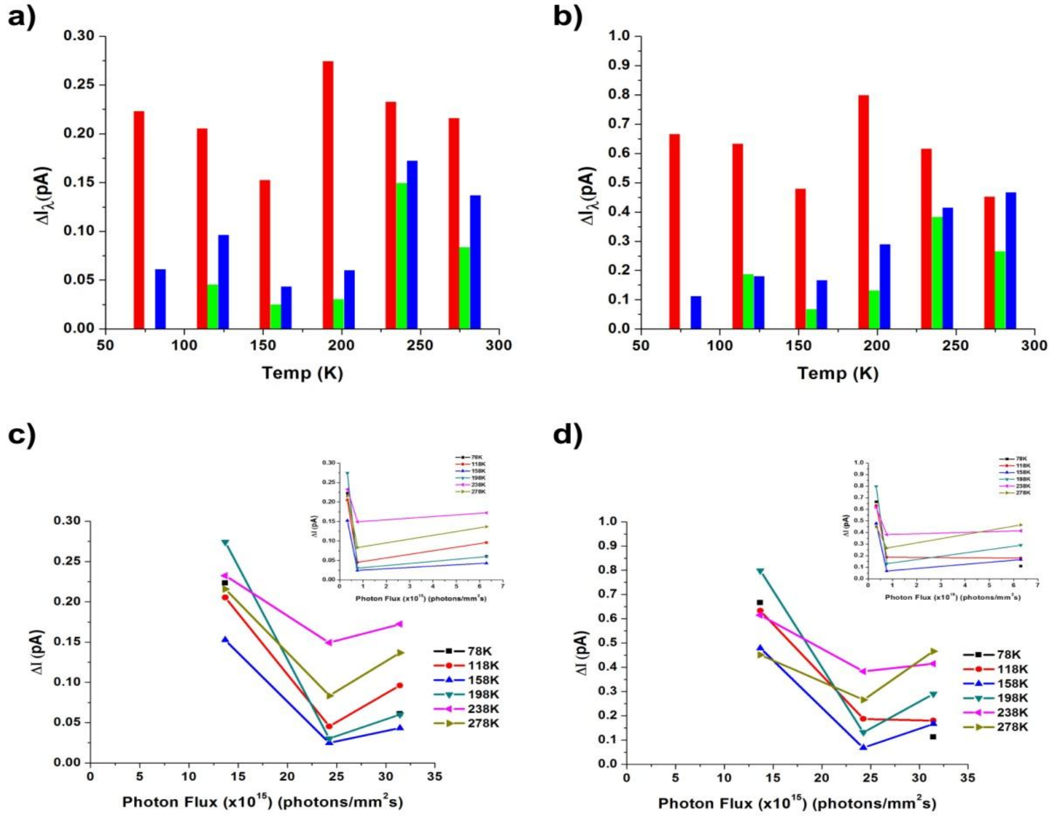

**Figure 4.21-** The current enhancement for AuNP array in **Figure 4.1(b)** linked with trimer molecules at various temperatures, in which the enhancement is the difference in current between that when exposed to light and the dark current. (a) & (b) are the temperature dependent current enhancements at 0.8V and 2.5V, respectively. Red for illumination with 655nm, green with 533nm, and blue with 405nm laser diode. (c) & (d) are re-plotted as a function of photon flux per unit area for the 405nm, 533nm, and 655nm laser diodes. The inserts are corrected for the absorption coefficients obtain from the absorption spectra of the trimer molecule in Section 2.7.3 at the relevant wavelength for the photon flux.

**Figure 4.22** shows the Fowler-Nordheim plots for the conductivity results represented in **Figure 4.21**. **Figure 4.22(a -d)** shows transition voltages for no illumination and illumination with red, green & blue light of 1.17V ±0.06V, 1.5V±0.02V, 1.26V±0.01V, and 1.26V±0.04V, respectively. This implies that illumination with red light increases the apparent barrier height by 0.33eV, while illumination with green and blue light increases the barrier height by only 0.09eV over the whole temperature range.

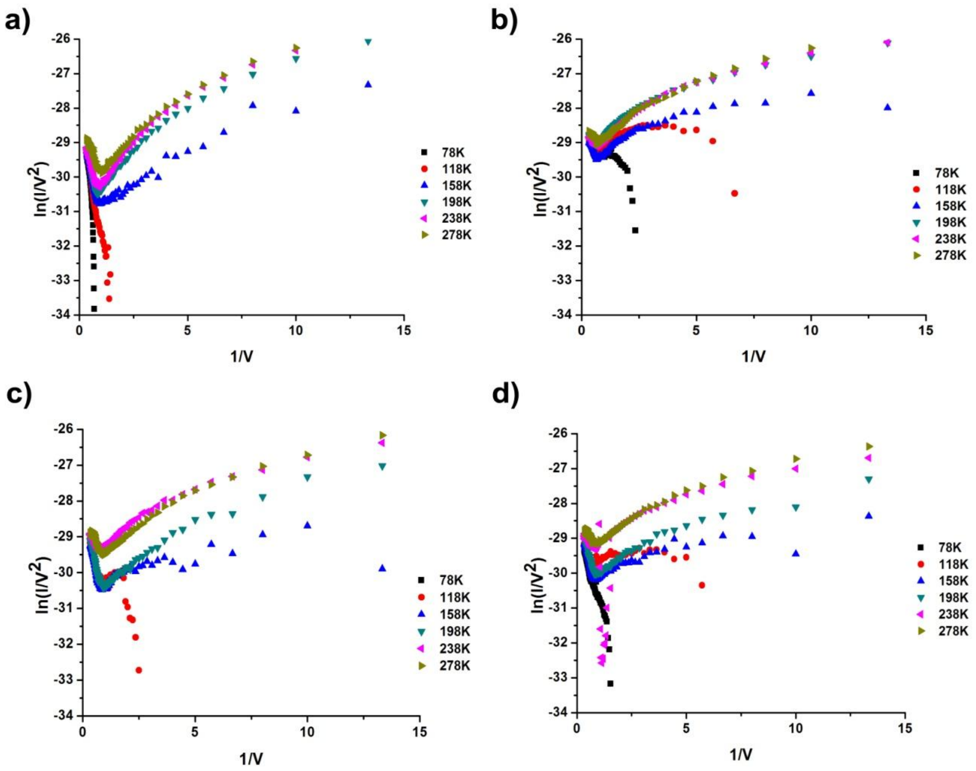

**Figure 4.22** – (a-d) Fowler-Nordheim plots of the conductivity data represented in **Figure 4.21**, for no illumination and illumination with red, green, and blue light, respectively. (a-d) exhibit transition voltages of 1.17V ±0.06V, 1.5V±0.02V, 1.26V±0.01V, and 1.26V±0.04V, respectively.

**Figure 4.23(a - d)** shows the temperature dependent dark conductivity plots for incident red, green, and blue light. **Figure 4.23(a)** & **(b)** shows the temperature dependent conductivity data re-plotted to distinguish thermionic emission by linearizing the conductivity data as ln(I/$T^2$) as a function of 1/kT at 1V and 2.5V, respectively. The figure shows that there is a transition around 250K at either applied voltage with no illumination. The transition is also observed on illumination with green or blue light, but not with illumination with red light. **Figure 4.23(c)** & **(d)** show the logarithm of the conductance as a function of inverse temperature (Arrhenius) at 1V and 2.5V, respectively. **Figure (c)** shows that the conductivity data below 200K is temperature independent, while above 200K, the apparent activation energy is 81.5meV for no illumination and a general decreasing of the activation energy with illumination with blue, green, and red light, respectively. Conduction on illumination with red light shows a nominal apparent activation energy, while illumination with blue and green light results in complex behavior. **Figure (d)** shows that the conductivity data below 200K is nearly temperature independent, while above 200K there are apparent activation energies of 40.6meV for no illumination to 23meV, 24.8meV, and 16.9meV for illumination with blue, green, and red light, respectively. Comparison of **Figure (c)** & **(d)** also shows that that the activation energy is voltage dependent with the activation energy decreasing with increasing voltage.

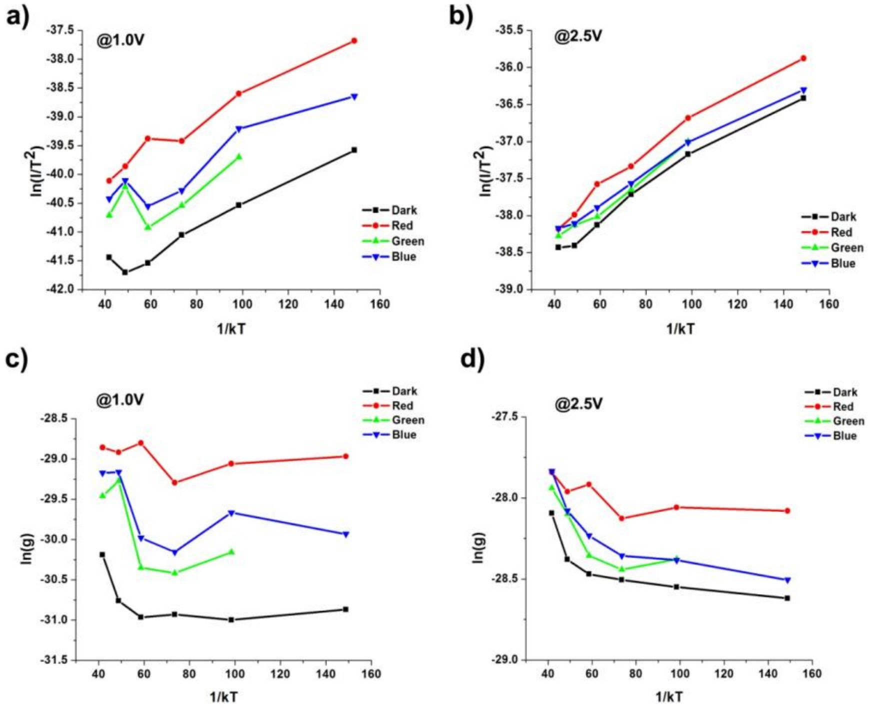

**Figure 4.23** –Temperature dependent conductivity data represented in **Figure 4.21**, for no illumination and illumination with red, green & blue light. (a) & (b) show the conductivity data linearized to a thermionic emission model at 1V and 2.5V, respectively. (c) & (d) show the logarithm of the conductance as a function of inverse temperature (Arrhenius) at 1V and 2.5V, respectively.

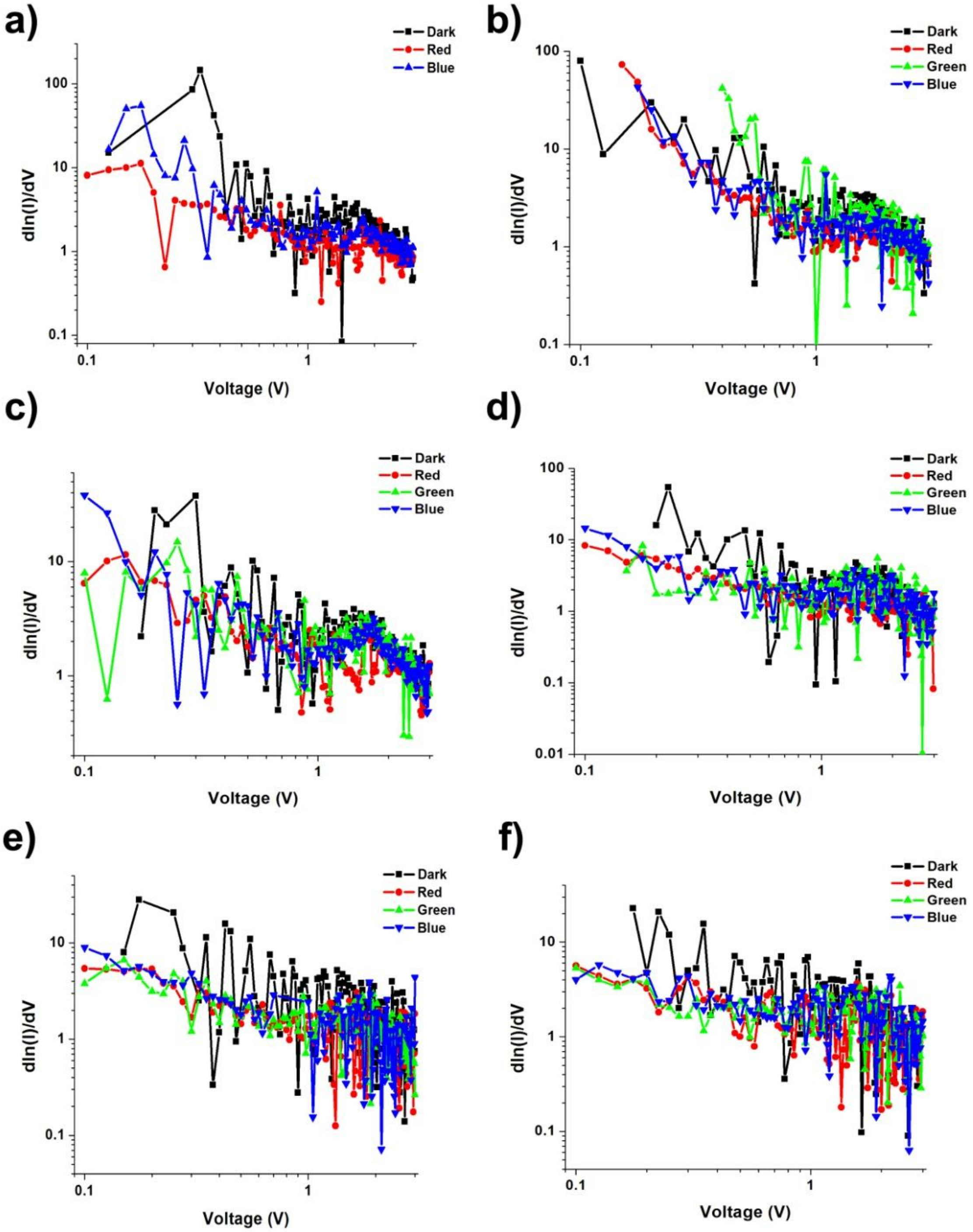

**Figure 4.24** - dln(I)/dV as a function of voltage, where **(**a – f) represent the dln(I)/dV plots at 78, 118, 158, 198, 238, and 278K, respectively.

**Figure 4.24** shows dlog(I)/dV as a function of voltage, where **Figure (a** – **f)** represent the dln(I)/dV plots at 78K, 118K, 158K, 198K, 238K, and 278K, respectively. The figure shows a transition in behavior around 1V, where below 1V the voltage dependence is linear. The incident light has no effect on the voltage or temperature dependence across the whole temperature range.

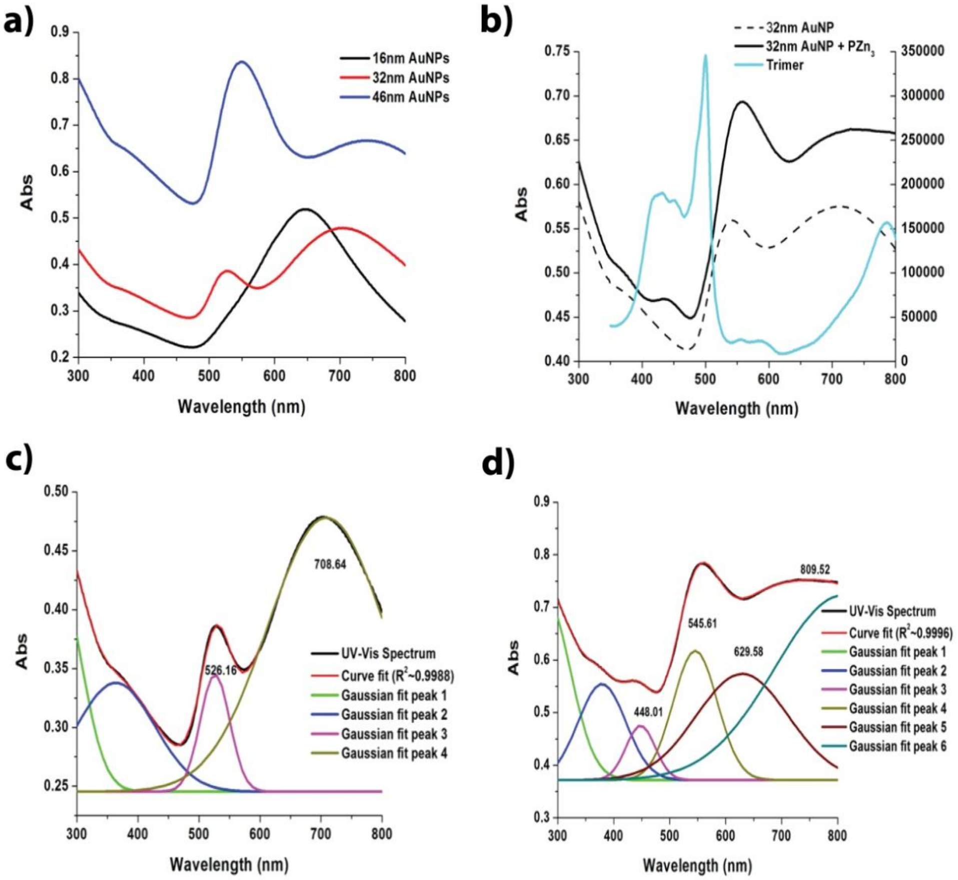

**Figure 4.25 -** Optical absorption for the AuNP arrays before and after functionalization with dithiol-PZn$_3$. (a) is the UV-Vis spectra of the 16nm, 32nm, and 46nm samples in **Figure 4.1(a-c)**, respectively. (b) is the UV-Vis spectra of only the 32nm sample, where the dotted line represents the AuNP's before attaching the dithiol-PZn$_3$ and the solid line denotes after linking the AuNP array, and the blue curve represents the absorption spectra of the dithiol-PZn$_3$ in solution. (c) & (d) are Gaussian peak fits of the 32nm sample before and after attaching the dithiol-PZn$_3$.

As reviewed in Section 2.2.4., the optical absorption due to the plasmons in gold nanoparticles depends on the particle size and the coupling between particles. **Figure 4.25** shows the optical absorption for the AuNP arrays before and after functionalization with dithiol-$PZn_3$. **Figure 4.25(a)** is the UV-Vis spectra of the 46nm, 32nm, and 16nm samples seen in **Figure 4.1(a-c)**. The primary plasmon peak near 550nm and the particle coupling absorption peak centered at 700nm both broaden and shift to longer wavelengths as the particle size increases, as expected. **Figure 4.25(b)** is the UV-Vis spectra of only the 32nm sample, where the dotted line represents the AuNP's before attaching the dithiol-$PZn_3$ and the solid line denotes after linking the AuNP array. Comparing the UV-Vis spectra in **Figure 4.25(c)** & **(d)** shows that both the primary plasmon peak and coupling peak broaden and shift to lower wavelengths with the attachment of the dithiol-$PZn_3$, and a peak located at 450 nm appears after the dithiol−$PZn_3$ is linked to the gold nanoparticles and indicates the successful attachment of the porphyrin complex to the nanoparticles. This is more easily seen by comparing the UV-Vis spectrum to the overlaid absorption spectra of the trimer molecule. For these arrays, a contribution to the conduction from a plasmon-induced interaction could thus occur for illumination with red and green light, but not with blue light.

**Figure 4.26** compares the current enhancements for 4 different AuNP arrays linked with monomers that exhibited near-linear conductivity behavior. The figure shows current enhancements at temperatures below the transition to metallic-like transport as seen in Section 4.4.2. The inserts show the current enhancements at room temperature, which exhibits metallic-like transport. **Figure (a -c)** are AuNP arrays with bi-modal distributions of 40/30nm, 40/15nm & 40nm/30nm, respectively, while **Figure (d)** is a AuNP array with 40nm nanoparticles. The figure illustrates that the current upon illumination with blue light ($\Delta I_{Blue}$) generally shows a larger increase in current than illumination with green or red light ($\Delta I_{Green}$ or $\Delta I_{Red}$). Although $\Delta I_{Blue}$ exhibits the largest increase in current, current enhancements ($\Delta I_{Green}$ or $\Delta I_{Red}$) due to illumination with green and red is found to vary from sample to sample. **Figure 4.27(a-d)** shows the current enhancements represented in **Figure 4.26(a-d)**, respectively, as a function of photon flux at various temperatures. The inserts show the photon flux corrected for the absorption coefficient at the relevant wavelengths.

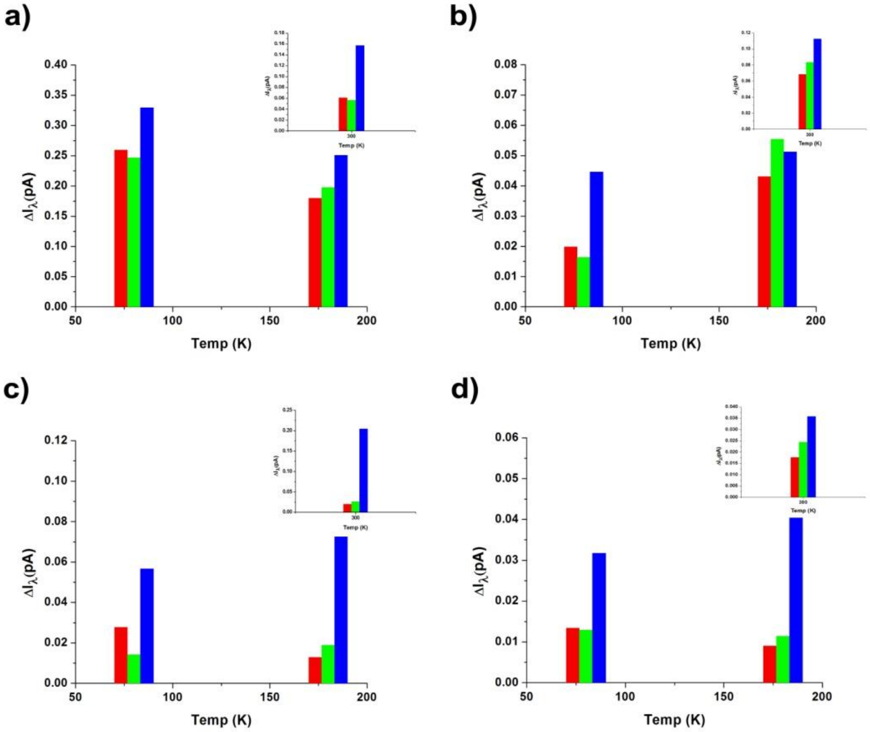

**Figure 4.26** – Comparison of current enhancement for 4 different AuNP arrays linked with monomers that exhibit near-linear conductivity behavior. The figure show current enhancements at temperatures below the transition to metallic-like transport. The inserts show the current enhancements at room temperature, which exhibits metallic-like transport.

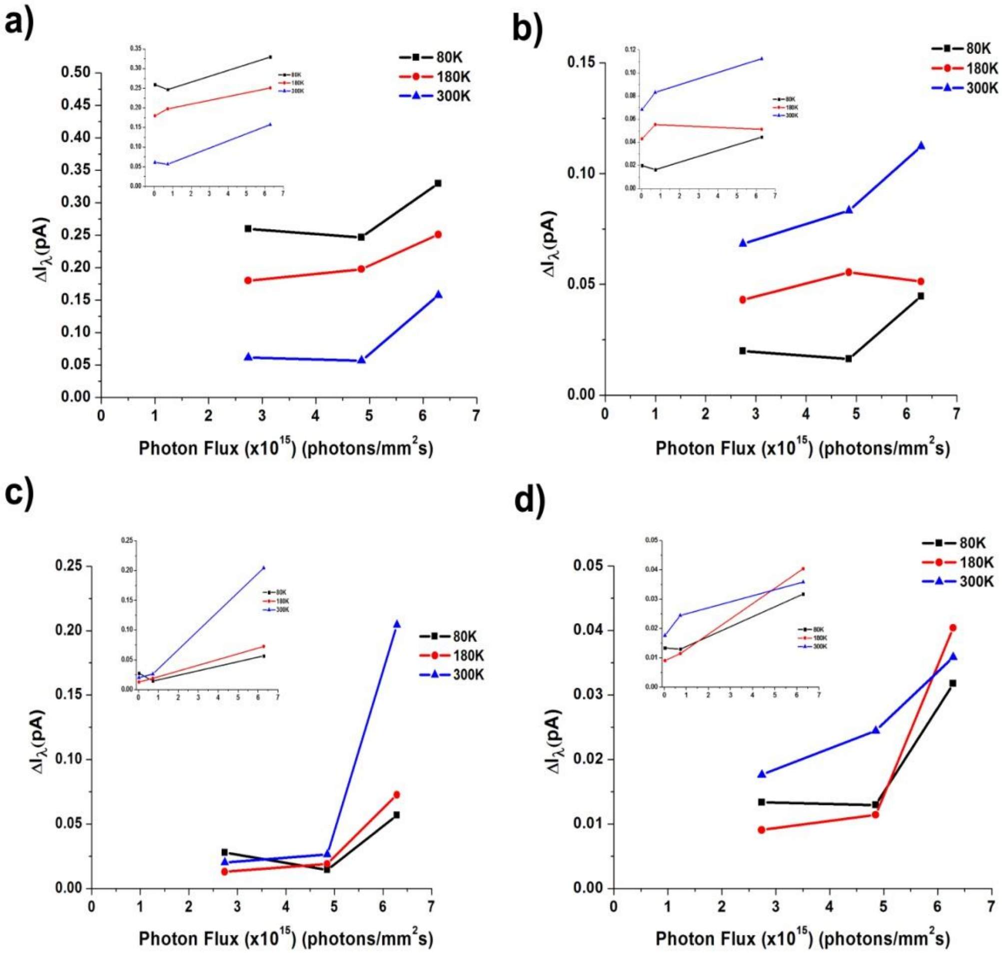

**Figure 4.27 -** Current enhancements represented in **Figure 4.26(a-d)**, respectively, as a function of photon flux at various temperatures. The inserts show the photon flux corrected for the absorption coefficient at the relevant wavelength.

**Figure 4.28 (a-d)** shows the logarithm of the conductance as a function of the inverse temperature of the data represented in **Figure 4.26(a-d)**, respectively. The Arrhenius plots show very small changes in the apparent activation energies as a result of illumination with all wavelengths of light. The inserts in **Figure 4.26(a-d)** show dln(I)/dV of the data represented in **Figure 4.26(a-d)**, respectively, as a function of temperature. The plots show that illumination with red, green, and blue light changes dln(I)/dV .

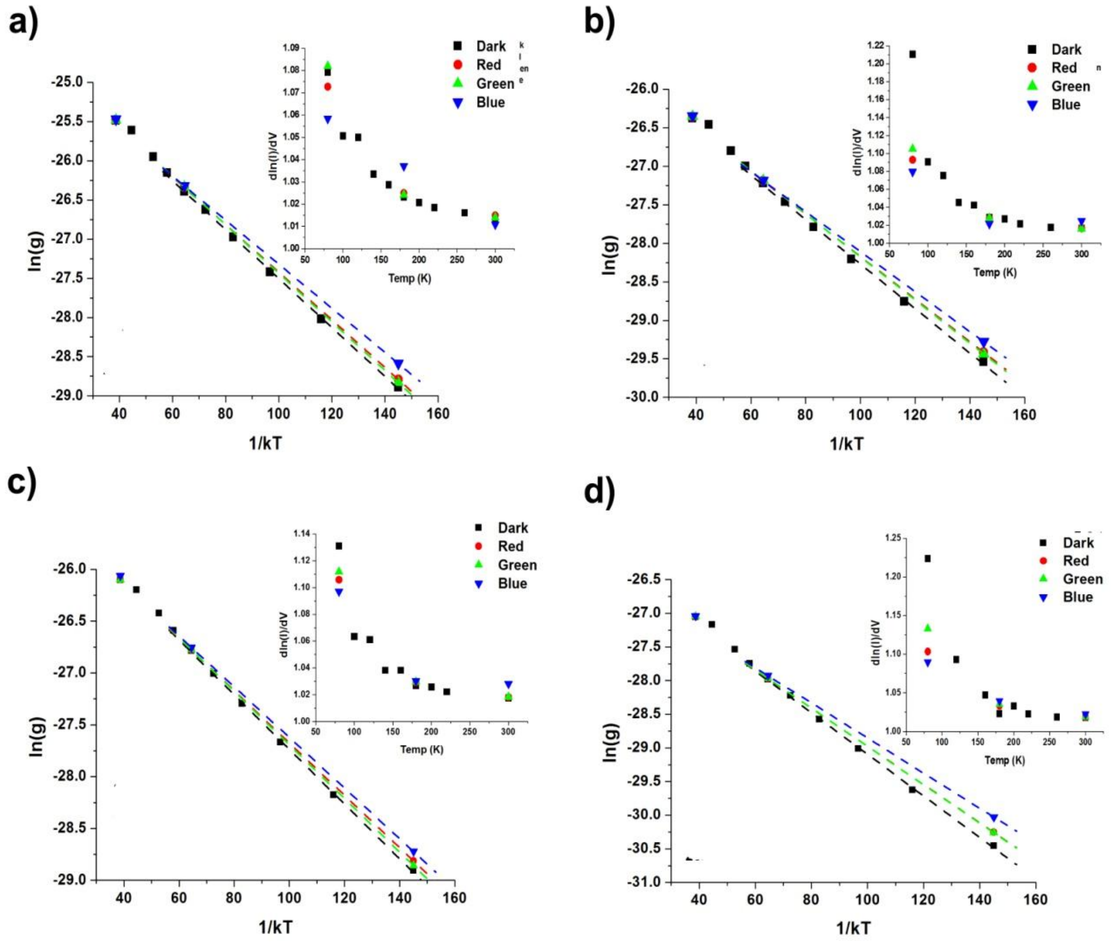

**Figure 4.28** - Logarithm of the conductance as a function of the inverse temperature of the data represented in **Figure 4.26(a-d)**, respectively. The inserts show dln(I)/dV of the data represented in **Figure 4.26(a-d)**, respectively, as a function of temperature.

**Figure 4.29** is a comparison of the UV-Vis spectra for the AuNP arrays represented in **Figure 4.26**. The blue, dark cyan, black, and red lines are the UV-Vis spectra of the samples represented in **Figure 4.26 (a -d)**, respectively. The insert in the figure shows one of the Gaussian curve fits as described in Section 3.6.2.

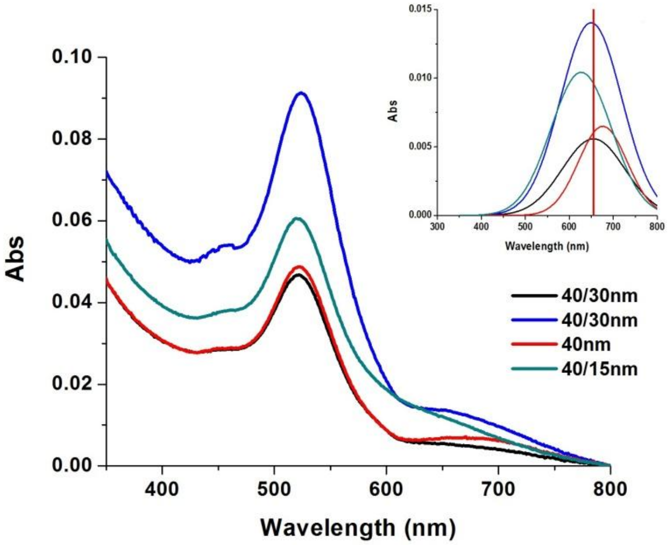

**Figure 4.29** - Comparison of the UV-Vis spectra for the AuNP arrays represented in **Figure 4.26**. The blue, dark cyan, black, and red lines are the UV-Vis spectra of the samples represented in **Figure 4.26 (a -d)**, respectively. The insert in the figure shows one of the Gaussian curve fits as described in Section 3.6.2.

**Figure 4.30(a-d)** compares the current enhancements for 4 different AuNP arrays linked with trimers (**a** & **b**), dimers, and monomers, respectively. The figure shows current enhancements at temperatures that exhibited activated transport. The inserts show the current enhancements at room temperature, which varied from sample to sample and exhibited activated to metallic-like transport. **Figure (a -d)** were AuNP arrays with bi-modal distributions of 40/15nm. The figure illustrates that the current upon illumination with blue light ($\Delta I_{Blue}$) generally shows a larger increase in current than illumination with green or red light ($\Delta I_{Green}$ or $\Delta I_{Red}$). Although $\Delta I_{Blue}$ exhibits the largest increase in current in general, an increase in current due to illumination with green and red light is found to have larger increases with AuNP arrays linked with dimers and trimer, especially at room temperature. **Figure 4.31(a-d)** shows the current enhancements represented in **Figure 4.30(a-d)**, respectively, as a function of photon flux at various temperatures. The inserts show the photon flux corrected for the absorption coefficient at the relevant wavelength.

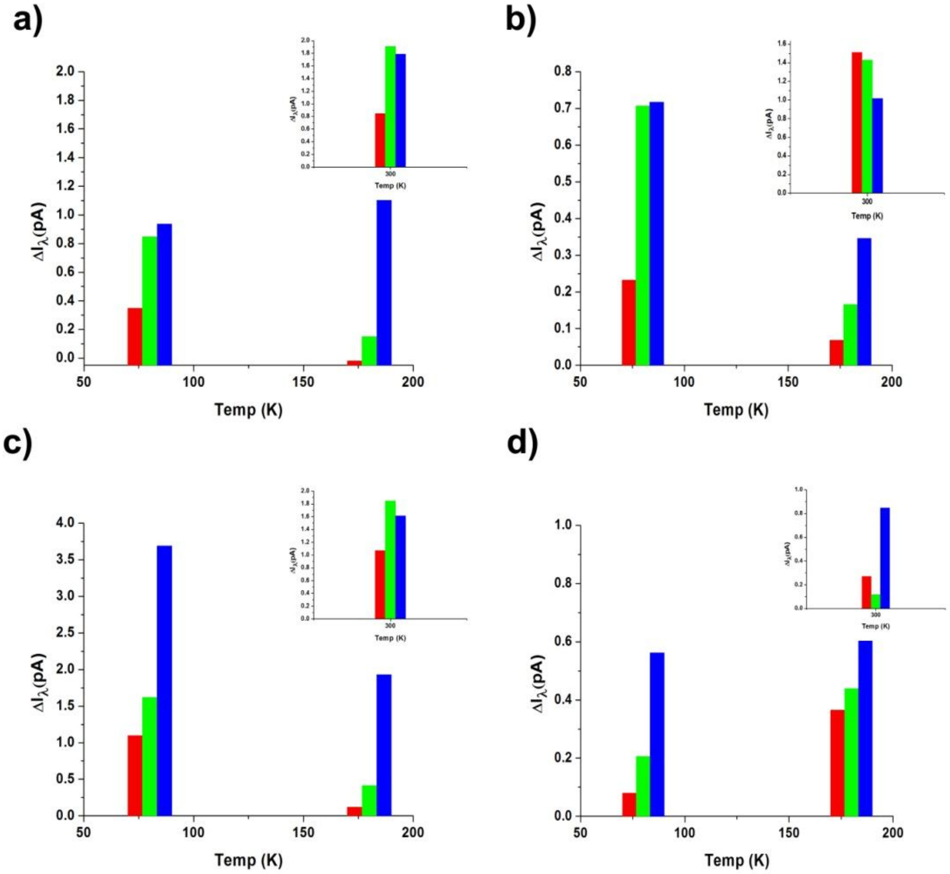

**Figure 4.30 –** Comparison of current enhancement for 4 different AuNP arrays linked with trimers (a & b), dimers (c), and monomers (d). The figure shows current enhancements at temperatures that exhibit activated transport. The inserts show the current enhancements at room temperature, which were variable from sample to sample and exhibited activated to metallic-like transport.

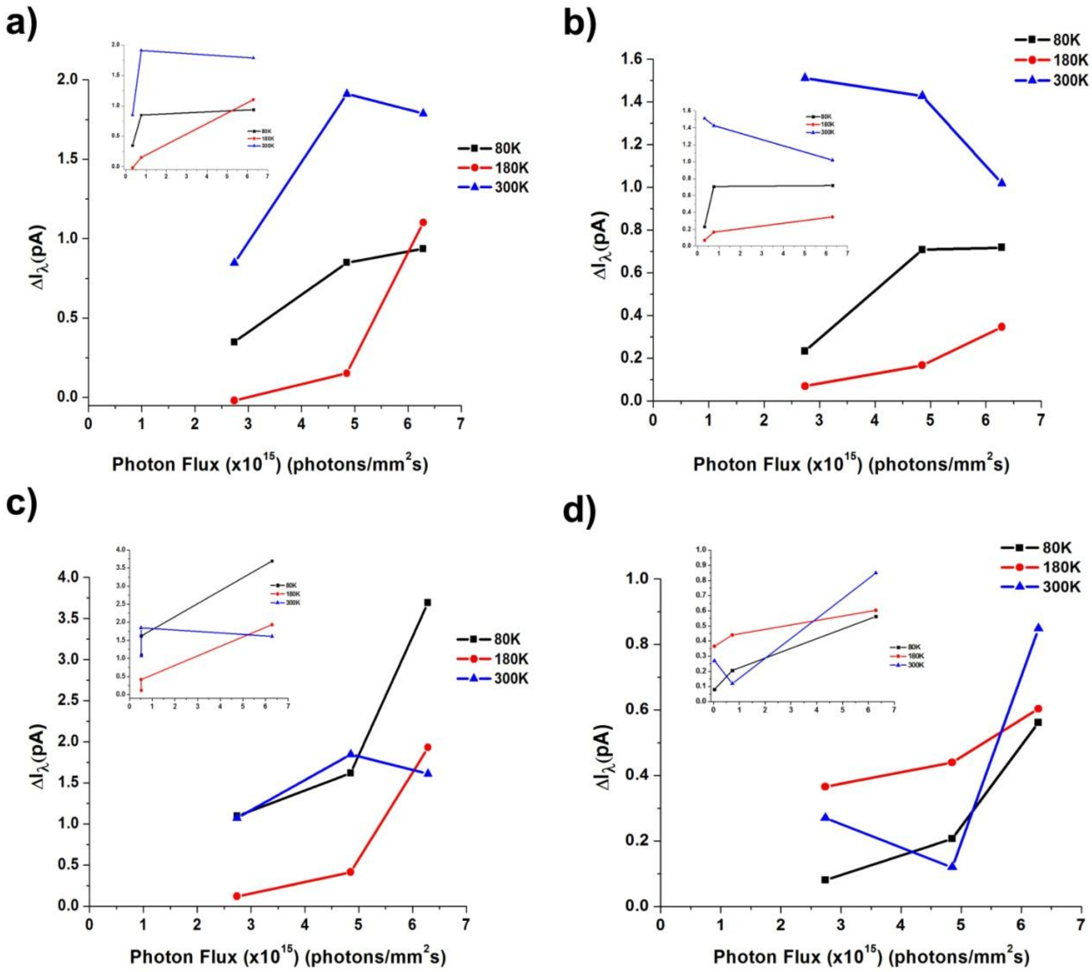

**Figure 4.31** - Current enhancements represented in **Figure 4.30(a-d)**, respectively, as a function of photon flux at various temperatures. The inserts show the photon flux corrected for the absorption coefficient at the relevant wavelength.

**Figure 4.32 (a-d)** shows the logarithm of the conductance as a function of the inverse temperature of the data represented in **Figure 4.30(a-d)**, respectively. The Arrhenius plots show very small changes in the apparent activation energies as a result of illumination with all wavelengths of light. The inserts in **Figure 4.32 (a-d)** show dln(I)/dV of the data represented in **Figure 4.30(a-d)**, respectively, as a function of temperature. The plots show that illumination with red, green, and blue light has an effect on dln(I)/dV. Unlike the case with monomers shown above, illumination with red, green and blue light on AuNP arrays linked with trimer and dimer molecules can have different effects on dln(I)/dV..

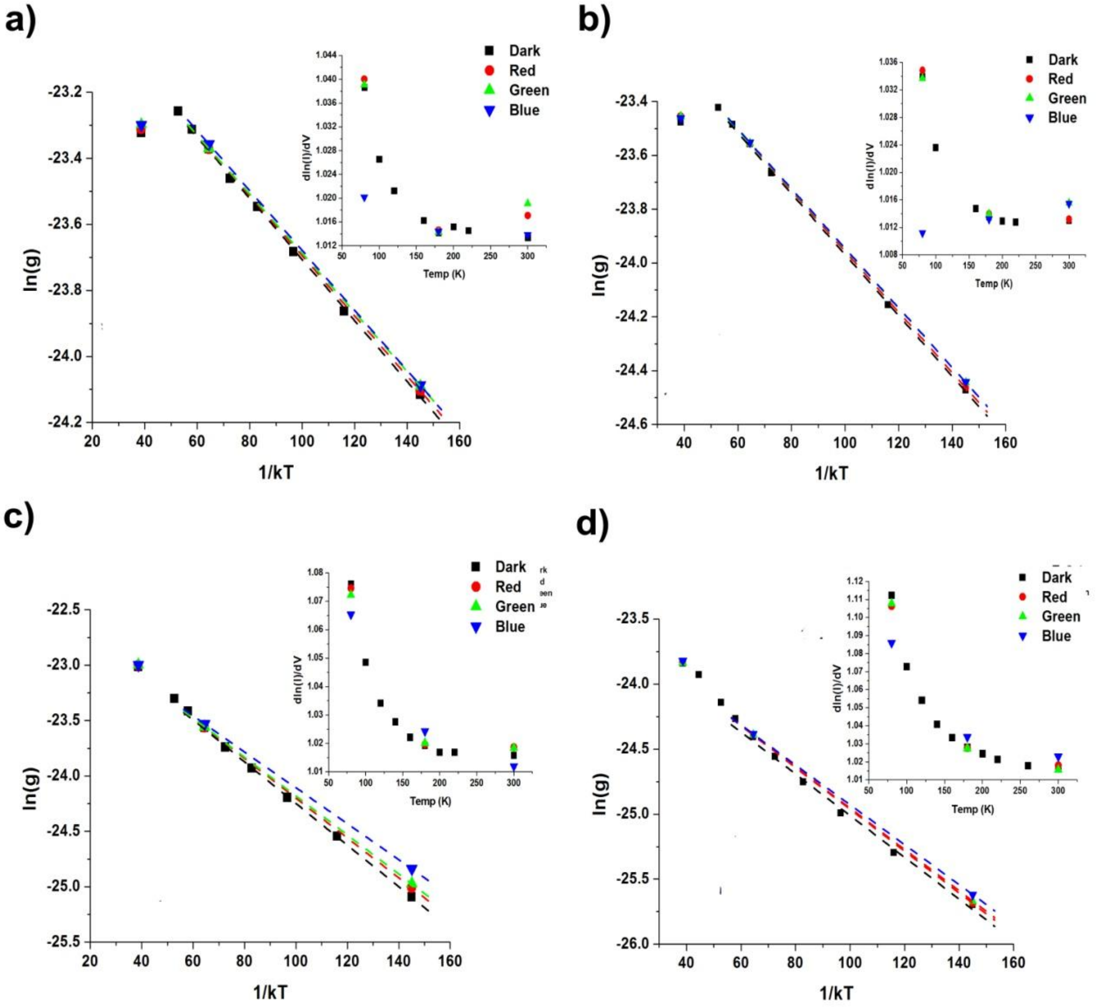

**Figure 4.32** - Logarithm of the conductance as a function of the inverse temperature of the data represented in **Figure 4.30(a-d)**, respectively. The inserts show dln(I)/dV of the data represented in **Figure 4.26(a-d)**, respectively, as a function of temperature.

**Figure 4.33** is a comparison of the UV-Vis spectra for the AuNP arrays represented in **Figure 4.30**. The red, blue, black, and dark cyan are the UV-Vis spectra of the samples represented in **Figure 4.30 (a -d)**, respectively. The insert in the figure shows one of the Gaussian curve fits as described in Section 3.6.2.

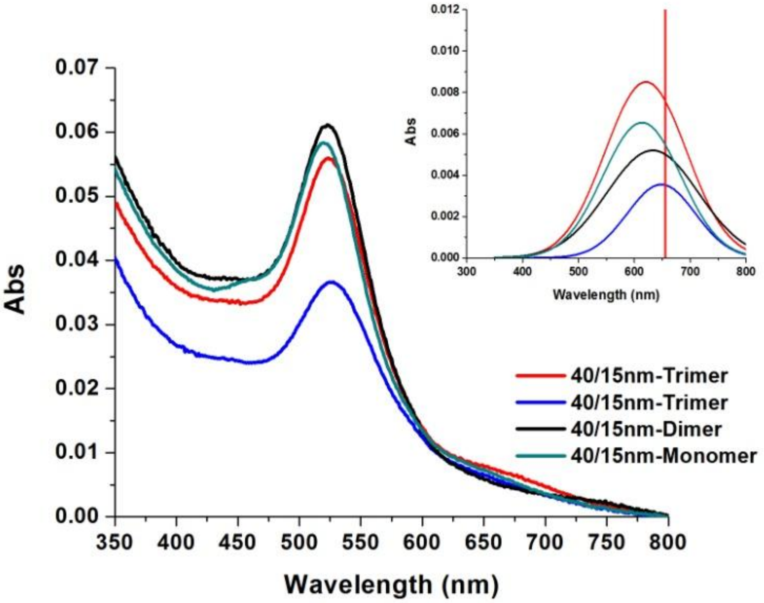

**Figure 4.33** - Comparison of the UV-Vis spectra for the AuNP arrays represented in **Figure 4.30**. The red, blue, black, and dark cyan are the UV-Vis spectra of the samples represented in **Figure 4.30 (a -d)**, respectively. The insert in the figure shows one of the Gaussian curve fits as described in Section 3.6.2.

## 4.6. Mechanisms of photoconduction

The analysis of photoconductance shows that the current enhancement results from multiple mechanisms. The parameters that dictate the ultimate magnitude of the current enhancement are the attached molecule, interfacial barriers, and optical coupling between nanoparticles. The current enhancement in some AuNP arrays exhibit anomalously high currents due to illumination with green and red light in relation to blue if the molecular photoconductivity was assumed to be proportional to the absorption extinction coefficients at the relevant wavelengths. In order to understand this discrepancy, a new phenomena referred to as plasmon enhanced photoconduction is put forth to describe the behavior. To further illustrate the interaction of light with the AuNP arrays, a parameter E, the enhancement factor, is introduced that quantifies the plasmon enhanced electrical conduction. The enhancement factor is defined as $E=\Delta I_{\lambda}/\Delta I_{blue}$, where $\Delta I_{\lambda}$ is the increase in the current as defined in Section 4.6 at wavelength λ (where λ=red, green, or blue). As an illustration, for the case of the 32 nm AuNP-based device in **Figure 4.21(a)** at 1 V and 278 K, *E* = 1 for blue light since no plasmon effect can contribute to the current based on the previous argument. Thus, an enhancement factor of 1 corresponds to conventional photocurrent, where conventional photocurrent is that occurring in the absence of any plasmon fields. A large E therefore quantifies the effect of plasmon interaction. The conventional photocurrent should therefore be directly proportional to the absorption oscillator strength at 405 nm in **Figure 2.15**. The photocurrent for red and green illumination should be smaller by a factor of approximately 4 or 8, since the absorption at those wavelengths is much less intense.

Instead, **Figure 4.21(a)** shows that the green light induced current is smaller only by a factor of 2 and the red light induced current is much larger than that induced with blue light. Over the measured temperature range, E varies from -0.2 to -2.1 for green light, and from 2.1 to 5.1 for red light. Such enhancement factors are much higher than those reported recently in alkane-linked AuNP arrays which show a bolometric enhancement of the current conduction that derives from surface plasmon excitation.[40] If Arrhenius activated processes are the dominate conduction mechanism, then based on the 5meV activation energy, an unrealistically high temperature of approximately 1875K would be required to account for the observed enhanced conductivity. Thus, these enhancements cannot be related purely to thermal effects.

The energies of relevance to transport for AuNP arrays exhibiting near-linear conductance, the highest occupied (HOMO) and the lowest unoccupied (LUMO) molecular orbitals are illustrated in **Figure 4.34**. The Fermi level of the nanoparticles is 0.415eV below the middle of the HOMO-LUMO gap of the dithiol-$PZn_3$.[102] The sulfur-gold bond at the interface plays a significant role in fixing the height of the barrier to transport, and although some electron localization at this interface is inevitable, it is assumed that the barrier height does not change appreciably. The $PZn_3$ $\pi$-system within the linker molecule is however completely delocalized and presents a near barrier less path for charge transport.[106] Upon application of a bias, hole mediated tunneling occurs as shown in **Figure 4.34(a)**. Under illumination three possible mechanisms can be proposed to explain the current enhancements. The first and most oblivious is direct exciton formation in molecule that is a function of the absorption cross-section and incident photo flux. The other two mechanisms are hot electrons from the excitation of surface plasmons and/or a field effect (optical annanna) from surface plasmons.

The schematic in **Figure 4.34** illustrates the possible mechanisms for current enhancement with trimer molecules linked to the AuNP array. Illumination with blue light results in conventional photoconductivity, as illustrated in **Figure 4.34(b)**. Optical absorption creates an exciton and the positive and negative charge carriers are separated in the electric field, contributing to the current. Absorption at 3.07eV produces an electron-hole pair; which initially is excited to a higher state that relaxes to a lower energy exciton within femtoseconds, where it can contribute to the current.[103] The increase in current is correlated with the number of carriers and consequently to the photon flux, absorption efficiencies, and the excited state lifetime. In the case where the incident radiation can excite the surface plasmons of the AuNPs, and the nanoparticles are optimally coupled, a large electromagnetic field is produced between the particles. As shown in **Figure 4.34(c)**, the surface plasmons can contribute to the current enhancement through either hot electrons or a field effect, where particles act as an optical antennae and focus the light into the small region between the particles.[107] The size, shape, and separation can be tailored to engineer the region of focused light. This focusing effect has the consequence of increasing the photon flux at the molecular junction. When the size, shape, and separation of the particles are optimized to produce a "resonant" optical antennae, enhancement factors as high as $10^4$ result.[108]

The case of AuNP arrays linked with monomer molecules provides a model system to understand the current enhancements throughout all the studied systems. This is due to the absorption characteristics of the monomer, which has a single absorption peak centered at approximately 425nm, as seen in **Figure 2.15**. This implies that if the current enhancement is due only to direct exciton formation in the molecule, then only a small band of wavelengths should result in current enhancements. Examination of the current enhancements for the near- linear conductance behavior seen in **Figures 4.26** & **4.27** reveals a range of wavelength dependent enhancement factors for the AuNP arrays linked with monomer molecules. **Figure 4.26(a)** & **(b)** exhibit larger current enhancements with blue illumination by a factor of 1.25 to 2 over red and green enhancements, while **(c)** & **(d)** exhibit larger blue current enhancements by a factor of 2.5 to 3.75 over red and green enhancements. The current enhancements as a function of photon flux shows that **(a)** & **(b)** have a more linear relationship compared to **(c)** & **(d)**. This implies that the photoconduction in **(c)** & **(d)** is the result of absorption of a photon in the molecule which creates an electron-hole pair which contributes to the conductance, whereas (a) & (b) have comparatively large red and green current enhancements.

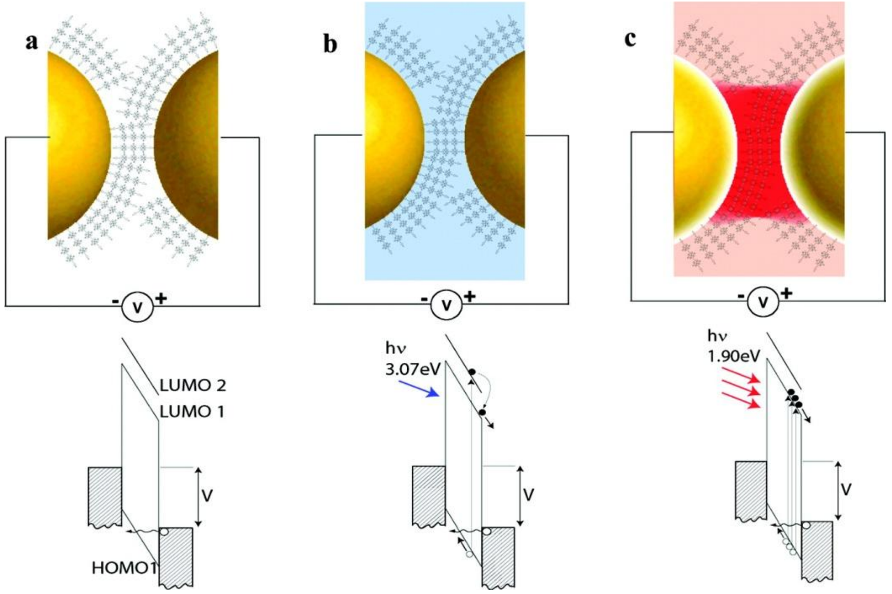

**Figure 4.34** - The highest occupied (HOMO) and the lowest unoccupied (LUMO) molecular orbitals are illustrated, where the Fermi level of the nanoparticles is 0.415eV below the middle of the HOMO-LUMO gap of the dithiol-$PZn_3$. (a) upon application of a bias, hole mediated tunneling occurs. (b) illumination with blue light results in conventional photoconductivity. (c) the incident radiation excites the surface plasmons, and the nanoparticles are optimally coupled, a large electromagnetic field is produced between the particles and the particles act as an optical antennae and focus the light into the small region between the particles.

The resulting effects of illumination on the electronic behavior, as seen in **Figure 4.28**, shows no appreciable change in the apparent barrier height to explain the differences in the current enhancements for illumination with red or green light. Comparison of the UV-Vis spectra in **Figure 4.29** provides some insight into the observed variations in the current enhancements. **Figure 4.29** shows that the arrays exhibiting the larger red and green current enhancements in **Figure 4.26(a)** & **(b)** have a larger absorption maximum centered around 650nm then the arrays that exhibit the larger comparative blue current enhancements in **Figure 4.26(c)** & **(d)**. This can be more clearly seen in the insert, where the Gaussian peak fit of the data show a clear increase in the magnitude of the peak located where the coupling peak would be for optimally coupled AuNP arrays. This indicates that the anomalously large red and green current enhancements are the result of plasmonic interactions between the AuNPs. Furthermore, due to the fact that there is minimal absorbance in the molecule at these wavelengths, the current enhancements are most likely due to hot electrons excited from surface plasmons.

The comparison of the current enhancement in **Figure 4.30**with AuNP arrays linked with trimer and dimer molecules that exhibit near-linear conductance behavior show a more complex behavior. As in the previous case, the data exhibits a wide range of wavelength dependent current enhancements. Examining the current enhancements as a function of photon flux in **Figure 4.31**, again show that the more linear the relationship, the larger the current enhancements for red and green illumination compared to that of blue light. The apparent barrier heights obtained from the Arrhenius plots in **Figure 4.32** do not show that illumination with light appreciably changes the electronic structure. Comparison of the optical spectra does not provide the same clarity as the previous example with the monomers. The variability in the current enhancements may still be due to the coupling peak observed in the UV-Vis spectra in **Figure 4.33**. The anomalous current enhancements for red and green in **Figure 4.30** do not scale with the magnitude of the coupling peak (insert of **Figure 4.33**) as in the previous case. This may be due to several factors, the first being that although the coupling peak is present in the spectra, when examining the overall UV-Vis spectra, the coupling peaks are nominal compared to the previous case. The second consideration is that the field effect (optical antenna) produced by excitation of the surface plasmons can no longer be ignored since the molecules now absorb at the excitation wavelengths. While the current enhancement due to illumination with blue light can still be attributed to direct exciton formation in the molecule, illumination with green and red light is a combination of hot electrons and the field effect as a result of the excitation of surface plasmons.

In the case of the AuNP array with non-linear conductance behavior, **Figure 4.21** shows an anomalously large current enhancement for illumination with red light across the whole temperature range. The Fowler-Nordheim plots in **Figure 4.22** show that the barrier height is increased by 0.33eV for illumination with red light, while illumination with green and blue light exhibits nominal effects on the barrier height. The temperature dependent conductivity data in **Figure 4.23** shows that at low and high biases, illumination with red light lowers the apparent barrier height more than illumination with green or blue light. The UV-Vis spectrum shows a very large coupling peak as compared to any of the samples exhibiting near-linear conductance behavior. **Figure 4.25** show the coupling peak is very broad and is located at ~700nm , which red shifts by ~100nm and broadens after attachment of the molecule. This may indicate coupling to the IR peak of the trimer molecule, which can be seen in the absorption spectrum in **Figure 4.25(b)**.

As in the case with the near-linear conductance behavior above, assuming that the particles are close enough that the light excites the plasmon resonance, then the anomalously high current enhancement should be the result of plasmonic interactions with the molecule. Unlike the case with the near-linear conductance behavior, the data indicates an extra barrier to transport at the interface and illumination with light effects the electronic structure. As in the previous case, illumination with green light exhibits higher current enhancement then would be expected if absorption only occurred through only direct exciton formation in the molecule. The current enhancement for green is similar in magnitude to the near-linear case above and the voltage and temperature dependence show that illumination with green and blue have nominal effects on the electronic structure. In contrast, illumination with red light has a large effect on the electronic structure when examining the voltage and temperature dependence. The discrepancy in the voltage and temperature dependent data may arise from the fact that two charge transport mechanisms are co-existing. The temperature dependence indicates that there is a larger decrease in the potential barrier with illumination with red light in comparison with blue or green light. The observation that the barrier increases with red illumination in the data of the Fowler-Nordheim plots may arise from the fact that the Fowler-Nordheim plots assume that the transition is from direct tunneling to field emission. With co-existing mechanisms, this assumption is no longer valid and the increase in the apparent barrier height may be a result of excitations to higher levels due to plamonic interactions between the particles and the transport being dominated by another mechanism.

The results show that the photoconduction can be controlled by varying the porphyrin molecule and through the coupling to the AuNP surface plasmons. To generalize this process, the nanoparticle arrays can be designed to sharpen and/or shift the plasmon resonance, while the molecules can be designed to control the absorption wavelength, oscillator strength, and the nature of the exciton on and polaron states.

# 5. Properties of hybrid AuNP nanostructures on PZT

## 5.1. Introduction

The previous chapter determined the transport mechanisms in hybrid porphyrin-AuNP assemblies on glass. The results demonstrated that multiple transport mechanisms occur simultaneously and a complex relationship between the plasmon resonance of the assemblies and the photoconductance occurs. This provides a basis on which to examine the properties of hybrid assembles on ferroelectric substrates. Due to the materials properties of underlying substrate, many of the assumptions for the glass case do not hold and, hence, need to be factored into the discussion of the charge transport and photoconduction. The elements of the test platform that need to be considered include the electric field created by the underlying ferroelectric domains, the substrates effect on the effective dielectric constant of the medium (and hence the plasmon resonance), and potential substrate effect on the charge transport through the nanoparticles themselves.

Although the previous section employed the use of a bimodal distribution of AuNP to understand the effects on transport and in hopes of manipulating the plasmon resonance, the understanding of the effects of a distribution of particles sizes will be very useful when it comes to understanding the transport through the AuNP on PZT. Unlike depositing colloidal AuNP (in which size and distribution can be controlled to the angstrom scale through processing variables and centrifugation), the size and distribution that result from nucleation and growth of metal nanoparticles on a ferroelectric substrate is unknown. Understanding how to control the deposition on ferroelectric surfaces and characterizing the particle size and distribution to then compare charge transport and photoconduction in similar model systems on glass will provide a basis to discuss the possible effects of the ferroelectric substrate on the photo response. In this chapter will determine the parameters that control the nucleation and growth of AuNPs on a ferroelectric surface. The size, density, and distribution will be characterized through which the growth mechanisms were determined. It will further be shown that utilizing FNL to selectively deposit AuNP arrays, that hybrid device structures can be realized.

### 5.2. Kinetics of photoreduction reactions on PZT

Domain specific photo-reduction on ferroelectric surfaces has been demonstrated by Bonnell and others[57, 61, 66, 109] but the control of the size, density and spacing for device applications has yet to be shown. In order to isolate the relevant factors, the photo reduction reaction of two different gold chloride metal salts on $P(Zr_{0.3}Ti_{0.7})O_3$ are studied. The effect of polarization orientation was determined by comparison of reactions on regions that were upwardly and downwardly poled with respect to the surface. The effect of polarization magnitude was determined by comparison of substrates with two textures: (100) and (111), where the PZT texture was a result of the orientation of the underlying Pt layer. Band pass and short pass filters were used to control the wavelength and exposure time was used to vary the incident photon flux.

150nm lead zirconate titanate (PZT) film with an underlying platinum (Pt) layer were used with a grain size of approximately100-150nm, and minimum domain size of 100nm. Polarization hysteresis curves determined a coercive voltage of ±1.7V for the Zr/Ti ratio of 30/70. A conductive AFM tip was biased with ±10V with respect to the grounded Pt layer to reorient the dipoles upwardly or downwardly with respect to the surface. **Figure 5.1** compares the topographic structure (left image) and the resulting surface potential after ferroelectric domains have been selectively reoriented (right image). The topographic structure consists of 100-200nm sized grains with 4.5nm RMS roughness. The contrast in the surface potential image ranges from 166mV to -112mV and is essentially bimodal with the width of the dark contrast lines of approximately 400nm. **Figure 5.2** relates the surface potential image, shown in **Figure 5.1**, with the underlying polarization vector direction. In addition to emphasizing the patterning aspect of the process, the simultaneous analysis of two adjacent orientations hold variables such as oxygen vacancies, atomic termination, and chemical environment constant.

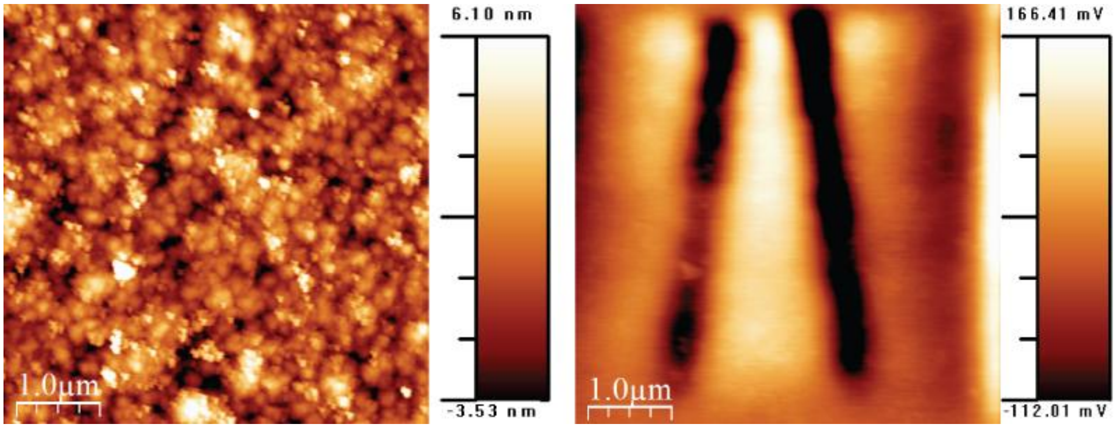

**Figure 5.1** – Comparison of the topographic structure (left image) and the resulting surface potential after ferroelectric domains have been selectively reoriented (right image). The topographic structure consists of 100-200nm sized grains with 4.5nm RMS roughness. The contrast in the surface potential image ranges from 166mV to -112mV and is essentially bimodal with the width of the dark contrast lines of approximately 400nm.

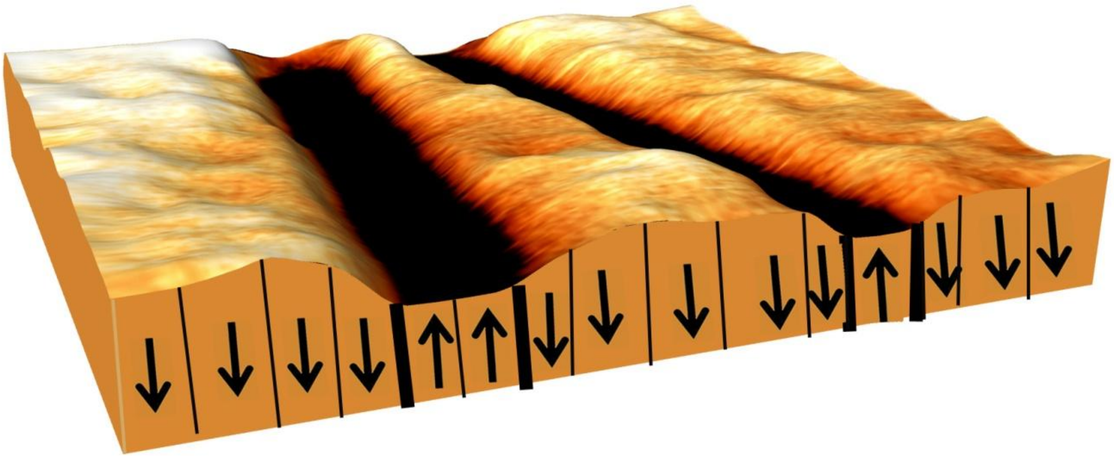

**Figure 5.2** – Relationship between the domain orientation direction and the surface potential image seen in **Figure 5.1**.

**Figure 5.3** compares the topographic structure (left image) and the piezo-force microscopy (PFM) image (right image), in which the contrast in the piezo-force phase image directly measures the direction of the out-of-plane vector component. The contrast in the piezo-force image is basically bimodal with a $180^o$ difference in the contrast. PFM is used to confirm that the difference in the surface potential image is the result of the reorientation of the underlying domains, and not the modification of the surface due to injection of charge and/or oxidation of the surface. Note that the surface topography exhibits a RMS roughness on the order of 3-5nm but is not reflected in the surface potential or piezo-force variations. This indicts that neither image (SSPM & PFM) is a topographic artifact, and an accurate measure of both the surface potential and piezo-force variations.

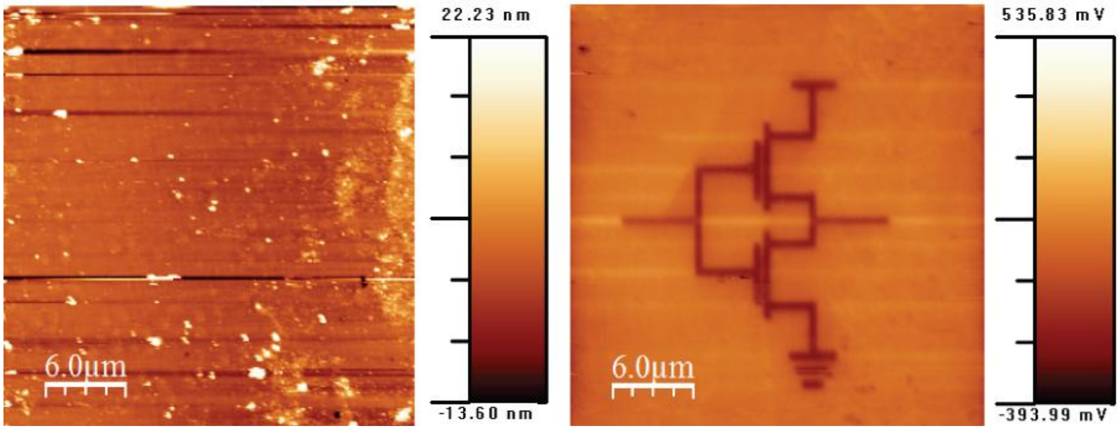

**Figure 5.3** – Comparison of the topographic structure (left image) and the piezo-force microscopy (PFM) image (right image) after polarization patterning. The contrast in the piezo-force phase image directly measures the direction of the out-of-plane vector component.

When the patterned substrates are immersed in an aqueous gold salt solution and exposed to sub-UV light, photoreduction occurs. The following three metal-salts; $AgNO_3$, $HAuCl_4$, and $NH_4AuCl_4$, will be compared to determine the growth mechanisms on PZT and to fabricate hybrid device structures. The reactants in the photo-reduction reaction are as follows:

$$Ag^{+} + NO_3^{-} + e \overset{hv}{\rightarrow} Ag(s) + NO_3^{-}$$

$$NH_4^{+} + AuCl_4^{-} + 3e \overset{hv}{\rightarrow} Au + NH_4^{+} + 4Cl^{-}$$

$$H^{+} + AuCl_4^{-} + 3e \overset{hv}{\rightarrow} Au + H^{+} + 4Cl^{-}$$

The reduction potentials of these metal salts in relation to the SHE and the band structure of PZT can be seen in **Figure 2.24**. Note that for the gold salts that the metal is reduced from a negative ion, while silver is reduced from a positive ion. This means that the gold ions can participate in the Stern layer (as described in Section 1.4.5.), while electrons will need to tunnel through the Stern layer to interact with the silver ions.[70, 110] The reduction reaction occurs over the positively poled domains, at which the electrons face no energy barrier from the conduction band. The reaction kinetics then depend on the electrolyte solution (metal salt and concentration), ferroelectric substrate (composition, vector orientation, and surface termination), and incident light (energy, photon flux). This study will focus on the deposition of gold nanoparticles on PZT.

### 5.2.1. PZT (111) textured substrates

The concentration of $AuCl_4^-$ was varied from 1µM to 10mM and the incident power was varied from 0.6mW to 77W. At high concentration (10mM-100mM) and short exposure times (1-15min), the reaction on the positive domains is much faster than that on the negative domains. In this regime, as seen in **Figure 5.4**, the domain shows excellent selectively. **Figure 5.4(a)** shows gold nanoparticles deposited on (111) textured $P(Zr_{0.3}Ti_{0.7})O_3$ immersed in a 9mM $HAuCl_4$ solution. The substrate was then illuminated with broad band light from an arc lamp filtered through a 270nm band pass filter for 5 min., while **Figure 5.4(b)** was illuminated with broad band light filtered through a 450nm short pass filter for 10min.

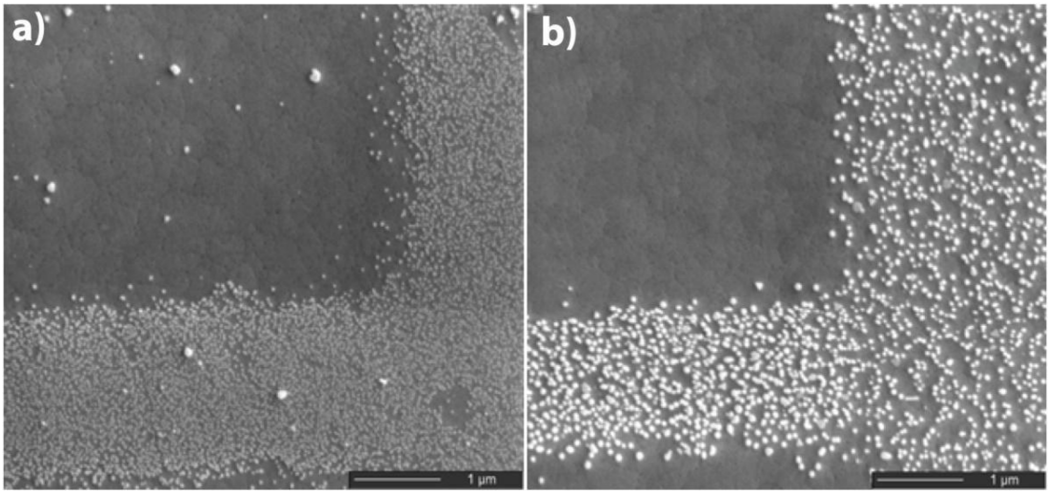

**Figure 5.4** – (a) & (b) show gold nanoparticle deposition structures on (111) textured $Pb(Zr_{0.3}Ti_{0.7})O_3$ substrates which were immersed in a 9mM $HAuCl_4$ solution. (a) was exposed for 5 minutes through a 270nm band pass filter, (b) was exposed through a 450nm short pass filter for 10 minutes.

The SEM micrographs demonstrate the ability to empirically control the size and density of the metal nanoparticles. The conditions used for the sample in **Figure 5.4(a)** exhibits much smaller particles and spacing than those used for the sample in **Figure 5.4(b)**, the difference was achieved by varying only two deposition parameters (time and photon flux). The difference in particle density due to the larger photon flux is evident in a comparison of **Figure (a)** & **(b)**. These initial results demonstrate the ability to create similar AuNP assemblies to the systems on glass, which means that the electrical and optical responses of the system can be manipulated to tune the photoconduction. It is difficult to access an extended reaction coordinate from deposition conditions seen in **Figure 5.4** but low concentrations (1μM-10mM) and long exposure times (30-120min) allow the reaction rates to be quantified. **Table 5.3** is a summary of all the deposition parameters that were varied to determine the growth mechanisms.

| **Substrate** | **Metal salt** | **Arc lamp with 200W Hg(Xe) bulb** | | | | |
|---|---|---|---|---|---|---|
| | | No filter | 450nm short pass | 270nm band pass | 250nm band pass | 214nm band pass |
| **PZT (111)** | $HAuCl_4$ | 5-30min | 30-60min | 30-60min | 30-60min | 30-60min |
| | $NH_3AuCl_4$ | 5-30min | 30-60min | 30-60min | 30-60min | 30-60min |
| **PZT (100)** | $HAuCl_4$ | 5-30min | 30-60min | 30-60min | 30-60min | 30-60min |
| | $NH_3AuCl_4$ | 5-30min | 30-60min | 30-60min | 30-60min | 30-60min |

**Table 5.1** –Deposition parameters varied to determine the growth mechanism.

The following section will compare the dependence of particle size and coverage on polarization orientation and metal salt on (111) textured PZT. **Figure 5.5** shows SEM micrographs of four different deposition conditions. **Figure 5.5(a)** & **(b)** compares the deposition of AuNPs from a 0.7mM solution of $HAuCl_4$ employing a 270nm band pass filter for 30 and 60 minutes, respectively. **Figure 5.5(c)** & **(d)** compares the deposition of AuNPs from a 0.7mM solution of $NH_3AuCl_4$ employing a 270nm bandpass filter for 30 and 60 minutes, respectively. **Figures 5.6** and **5.7** compare the dependence of particle morphology and distribution on polarization orientation and metal salt. The figures compare the coverage of gold nanoparticles deposited on (111) textured PZT, holding concentration constant for both the $HAuCl_4$ (**Figure 5.6**) and $NH_4AuCl_4$ (**Figure 5.7**) solution at 0.7mM and constant optical intensity of $1.5*10^{15}$photons/sec.

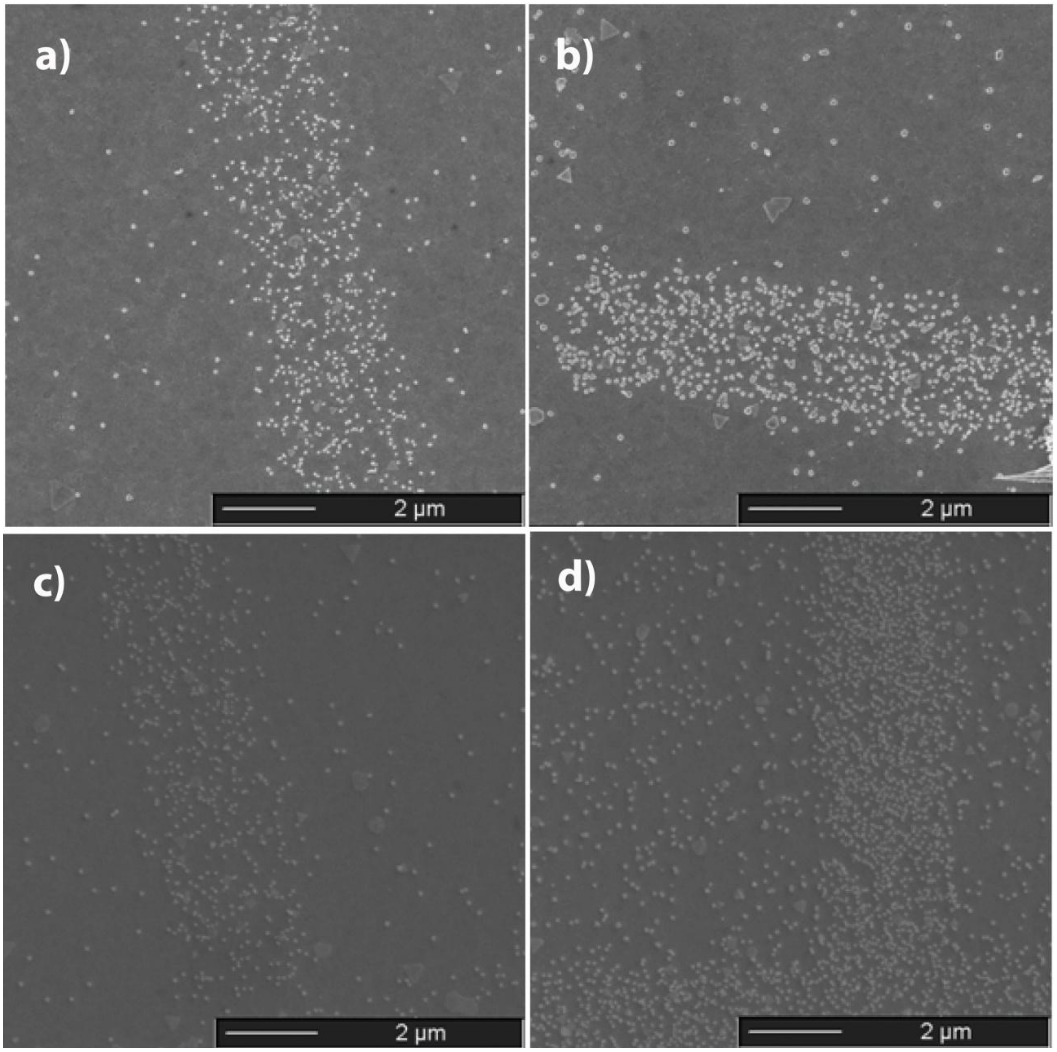

**Figure 5.5**- (a - d) show gold nanoparticle deposition structures on (111) textured Pb($Zr_{0.3}Ti_{0.7}$)$O_3$ substrates. (a) & (b) were immersed in a 0.7mM $HAuCl_4$ solution, while c) and d) were immersed in a 0.7mM $NH_3AuCl_4$ solution. (a) & (c) were exposed for 30 minutes through a 270nm band pass filter, while (b) & (d) were exposed through a 270nm band pass filter for 60 minutes.

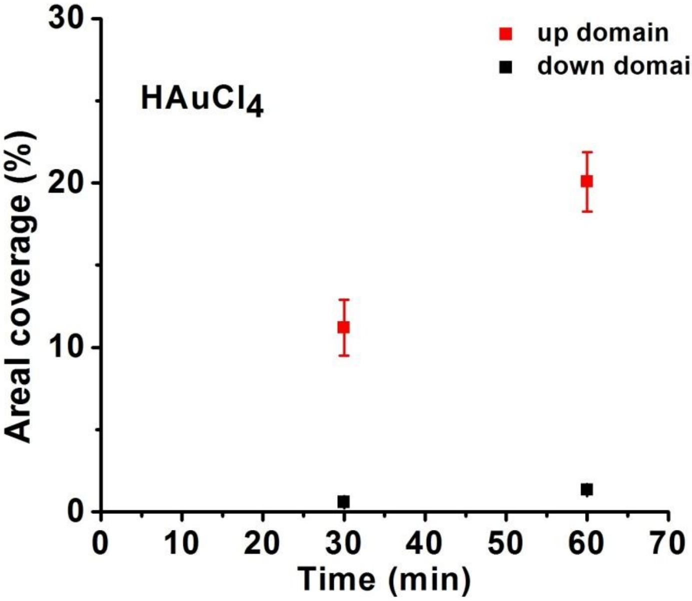

**Figure 5.6** – Comparison of the areal coverage on positive (up) and negative (down) domains at 30 and 60 minutes for 0.7mM solutions of $HAuCl_4$ exposed through a 270nm band pass filter on (111) textured PZT.

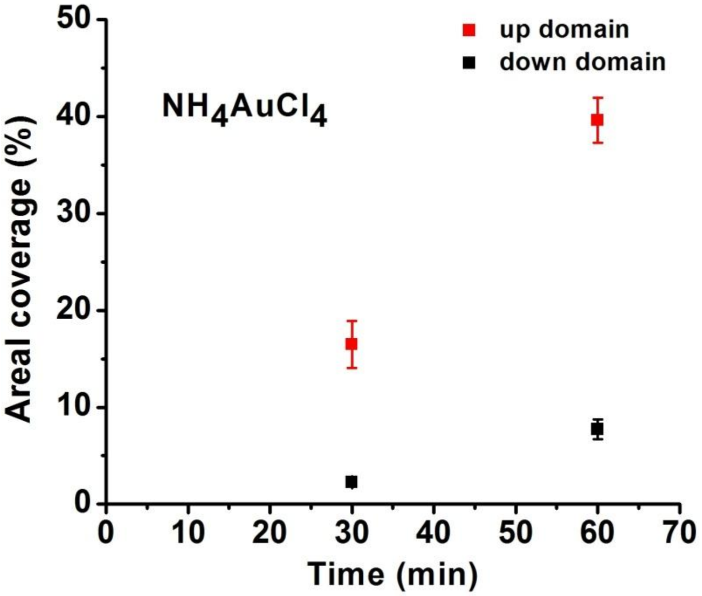

**Figure 5.7** – Comparison of the areal coverage on positive (up) and negative (down) domains at 30 and 60 minutes for 0.7mM solutions of $NH_3AuCl_4$ exposed through a 270nm band pass filter on (111) textured PZT.

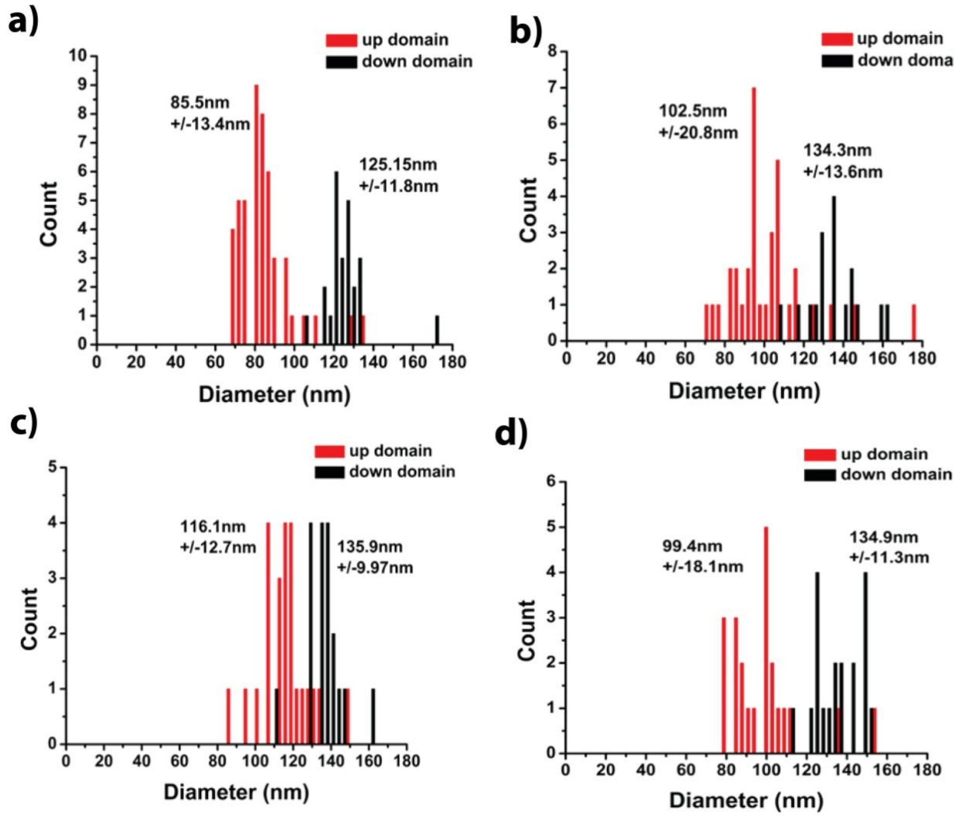

**Figure 5.8** – Sizes and distributions of gold nanoparticles deposited under various conditions. (a) & (b) are histograms of particle sizes on up and down domains form the 30 and 60 minute deposition conditions corresponding to **Figure 5.6**. (c) & (d) are histograms of particle sizes for the 30 and 60 minute deposition conditions in **Figure 5.7**.

The most notable result is that the coverage is much lower on the negative domains than on the positive domains. The areal coverage is close to 0% in most cases and does not exceed 7%. Also as expected, the coverage increases with increasing incident photon flux for both the up and down domains and for all metal salts. Interestingly, the reduction from the $NH_4AuCl_4$ has a higher coverage than that from the $HAuCl_4$. **Figure 5.8(a – d)** quantifies the size distributions of gold nanoparticles that result on up and down domains seen in **Figure 5.5(a – d)**, respectively. Particles on the up domains are consistently smaller compared to particles on the down domains. As seen in **Figure 5.8(a)** & **(b)**, particle reduced from $HAuCl_4$ on the up domains produce 85nm and 102nm diameter particles, respectively, while the down domains produce 125nm and 134nm diameter particles, respectively. The size of the particles does not change consistently with the degree of the reaction. In other words, the particle size remains the same, within the distribution, as the reaction continues. Examining **Figure 5.8(c)** & **(d)** shows that this trend is observed for AuNPs reduced from $NH_3AuCl_4$. Another result from **Figures 5.6**, **5.7**, & **5.8** is that the size of the nanoparticles does not appear to be dependent on which metal salt the nanoparticles are reduced from. This means that the increase in surface coverages seen in **Figures 5.6** & **5.7** are only the result of an increase in particle density on the surface.

### 5.2.2. PZT (100) textured substrates

The effect of the magnitude of the underlying ferroelectric domain was examined utilizing a (100) textured PZT substrate. The SEM micrographs in **Figure 5.9** illustrate the same four different deposition conditions as those seen in **Figure 5.5**, except the substrate was (100) textured PZT. **Figure 5.9(a)** & **(b)** compare the deposition of AuNPs from a 0.7mM solution of $HAuCl_4$ employing a 270nm band pass filter for 30 and 60 minutes, respectively. **Figure 5.9(c)** & **(d)** compare the deposition of AuNPs from a 0.7mM solution of $NH_3AuCl_4$ employing a 270nm band pass filter for 30 and 60 minutes, respectively. **Figures 5.10 and 5.11** compare the dependence of particle morphology and distribution on polarization orientation and holding concentration constant for both the $HAuCl_4$ (**Figure 5.10**) and $NH_4AuCl_4$ (**Figure 5.11**) solution at 0.7mM and constant optical intensity of $1.5*10^{15}$photons/sec. The results exhibit similar trends as the prior case with (111) textured PZT. The coverage is much lower on the negative domains than on the positive domains with the areal coverage is close to 0% in most cases and does not exceed 12%. Once again, the coverage increases with increasing incident photon flux for both the up and down domains and for all metal salts, and the reduction from the $NH_4AuCl_4$ has a higher coverage than that from the $HAuCl_4$

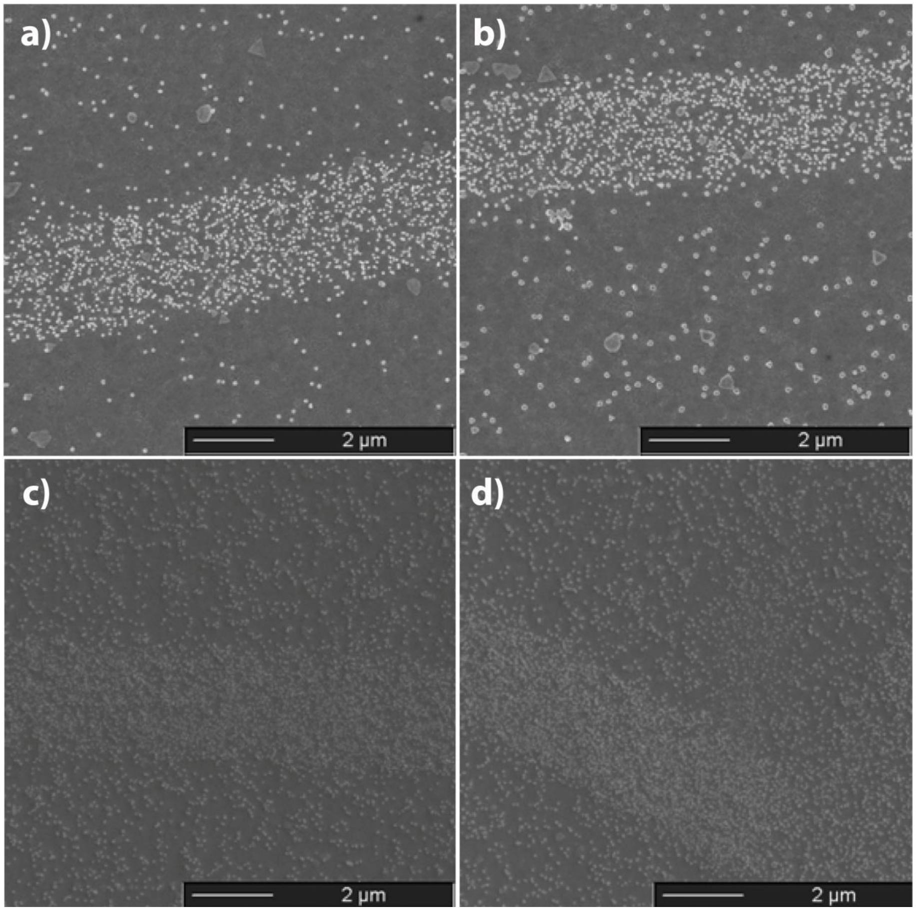

**Figure 5.9** – (a - d) show gold nanoparticle deposition structures on (100) textured $Pb(Zr_{0.3}Ti_{0.7})O_3$ substrates. (a) & (b) were immersed in a 0.7mM $HAuCl_4$ solution, while c) and d) were immersed in a 0.7mM $NH_3AuCl_4$ solution. (a) & (c) were exposed for 30 minutes through a 270nm band pass filter, while (b) & (d) were exposed through a 270nm band pass filter for 60 minutes.

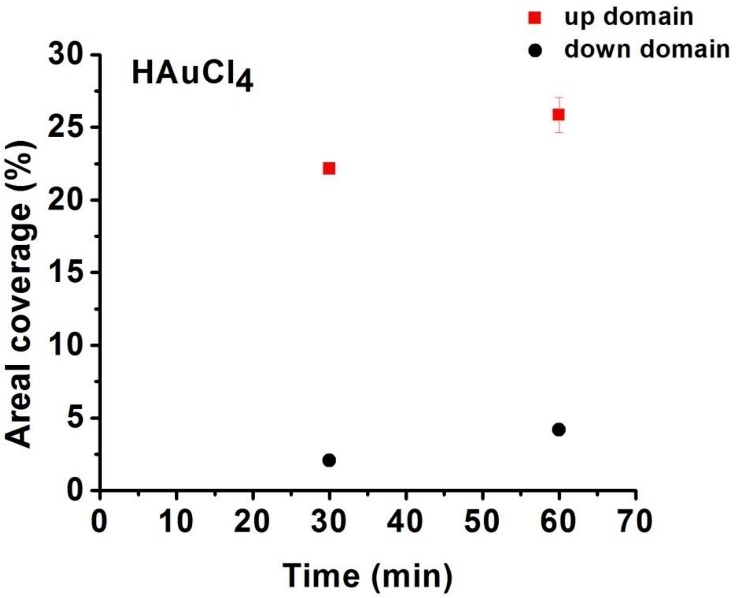

**Figure 5.10** – Comparison of the areal coverage on positive (up) and negative (down) domains at 30 and 60 minutes for 0.7mM solutions of $HAuCl_4$ exposed through a 270nm band pass filter on (100) textured PZT.

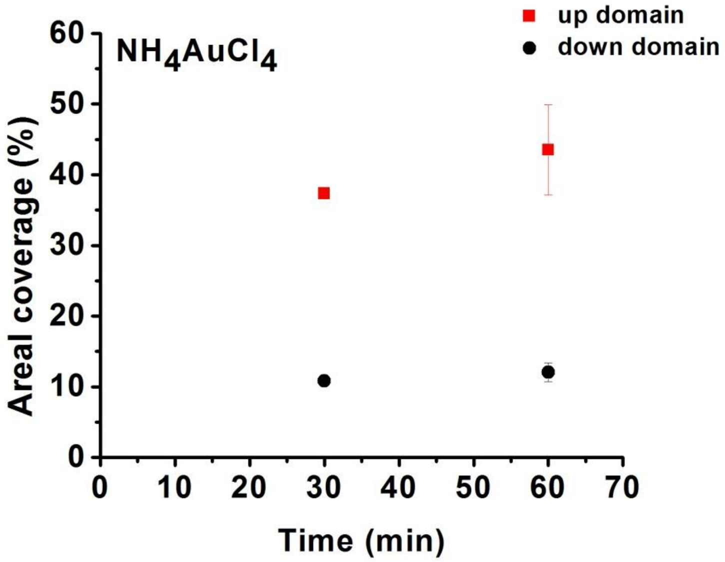

**Figure 5.11**- Comparison of the areal coverage on positive (up) and negative (down) domains at 30 and 60 minutes for 0.7mM solutions of $NH_3AuCl_4$ exposed through a 270nm band pass filter on (100) textured PZT.

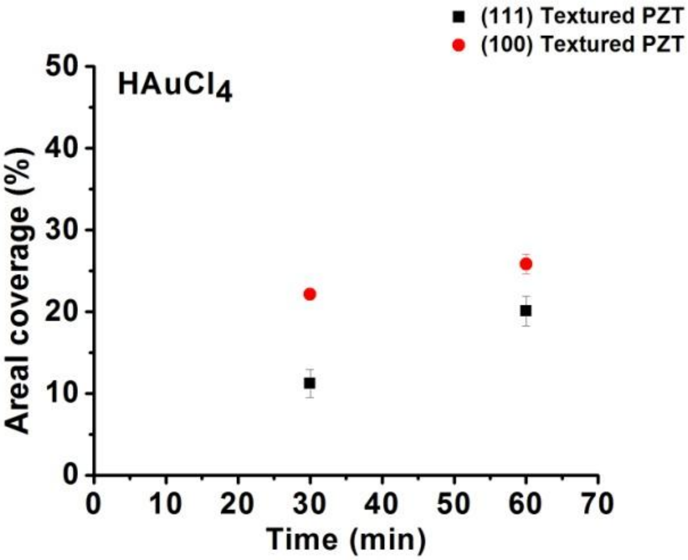

**Figure 5.12** – Comparison of the areal coverage on positive (up) domains for (111) and (100) textured PZT at 30 and 60 minutes for 0.7mM solutions of $HAuCl_4$ exposed through a 270nm band pass filter.

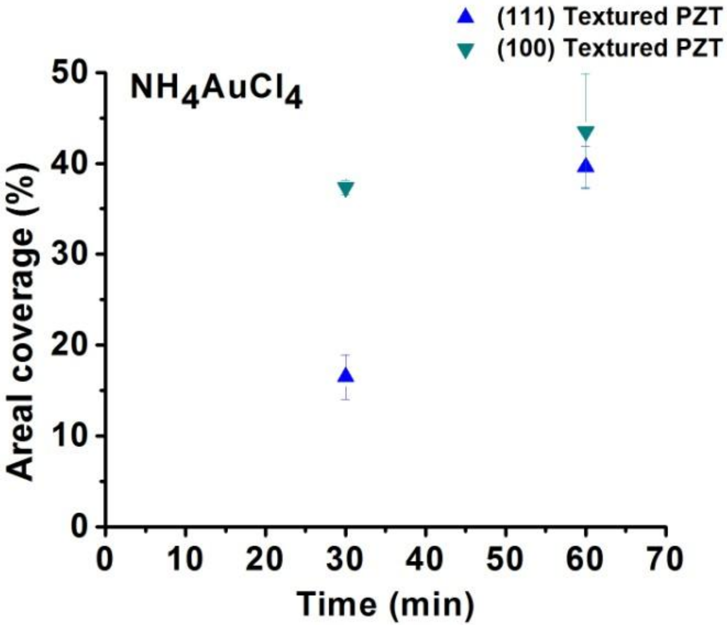

**Figure 5.13** – Comparison of the areal coverage on positive (up) domains for (111) and (100) textured PZT at 30 and 60 minutes for 0.7mM solutions of $NH_3AuCl_4$ exposed through a 270nm band pass filter.

**Figures 5.12** & **5.13** compare the areal coverage on the up domains for both metal salts on the (111) and (100) textured PZT. **Figure 5.12** shows that the deposition reaction for $HAuCl_4$ is faster on the (100) textured surface compared to the (111) textured surface, and **Figure 5.13** shows similar trends for $NH_3AuCl_4$.

## 5.3. Effects of optical power on photoreduction

The nucleation and growth of the metal nanoparticles is not dependent only on the surface interactions. With the exposure to broad band light from an arc lamp source, the deposition can result in the various structures illustrated in **Figure 5.14**, which compares the dependence of particle morphology and distribution on polarization orientation on (111) textured $Pb(Zr_{0.3}Ti_{0.7})O_3$ substrates. **Figure 5.14(a)**, **(c)** & **(e)** were immersed in a 0.7mM $HAuCl_4$ solution, while **Figure 5.14(b)**, **(d)** & **(f)** were immersed in a 0.7mM $NH_3AuCl_4$ solution. **(a)**, **(c)** & **(e)** were exposed for 10, 20 and 30 minutes, respectively, by an arc lamp with no optical filter, while **(b)**, **(d)** & **(f)** were exposed for 10, 20 and 30 minutes, respectively, by an arc lamp with no optical filter. As with the previous examples, the coverage is much lower on the negative domains than on the positive domains. The coverage increases with increasing photon flux but the particle size grows as well. Increasing photon flux, as seen in comparing **Figure 5.14(a)**, **(c)** & **(e)**, results in an increase in particle density followed by an agglomeration and increase in particle size. The resulting particles can greatly deviate from the spherical particles that dominate the deposition in previous examples.

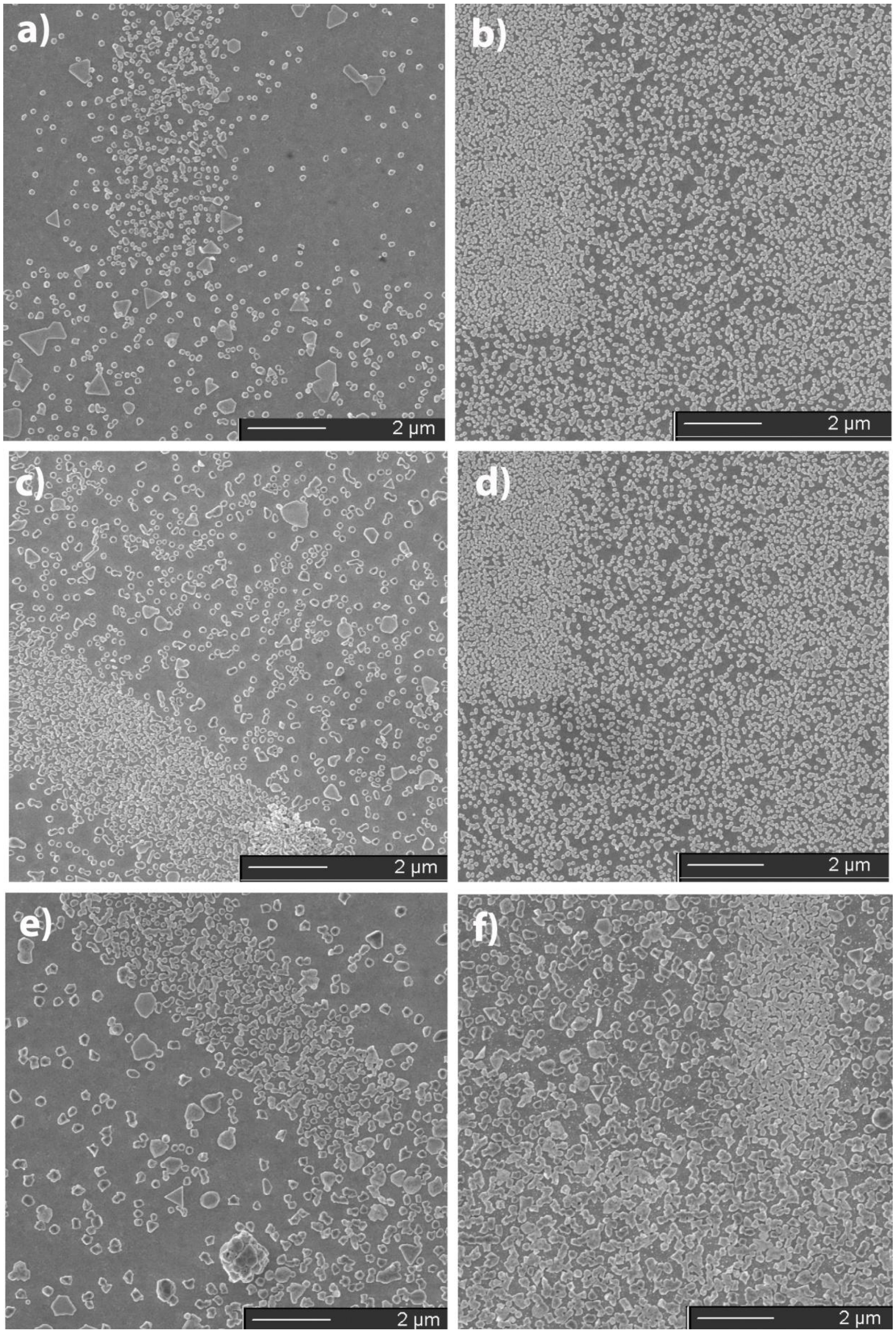

**Figure 5.14** – (a - f) show gold nanoparticle deposition structures on (111) textured Pb($Zr_{0.3}Ti_{0.7}$)$O_3$ substrates. (a), (c) & (e) were immersed in a 0.7mM $HAuCl_4$ solution, while (b), (d) & (f) were immersed in a 0.7mM $NH_3AuCl_4$ solution. (a), (c) & (e) were exposed for 10, 20 and 30 minutes, respectively, by an arc lamp with no optical filter, while (b), (d) and (f) were exposed for 10, 20 and 30 minutes, respectively, by an arc lamp with no optical filter.

In the following section, the discussion of growth mechanisms will be confined to the nucleation limited case. Although understanding that the growth of nanoparticles can be manipulated to fabricate various shapes and densities would be useful for possible AuNP arrays in hybrid device structures.

## 5.4. Deposition mechanism

The effects of the integrated photon flux on the density and areal density are illustrated in **Figures 5.15** and **5.16**, which compares reactions with 4 different exposure conditions at 30min and 60min with band pass filters of 250nm ±1nm and 270nm ±1nm which correspond to energies of 4.96eV and 4.59eV, respectively. Even with variations due to processing conditions and other factors, the bandgap of PZT is generally accepted to be between 3.2-3.7eV. This means that the incident energies are at least 0.9eV greater than the bandgap and provide the super band gap energy that has been shown to be required to drive photo-reduction at the surface.[75, 111] **Figures 4.15** and **4.16** show that both the density and coverage increase continuously with total photon flux and that $NH_4AuCl_4$ exhibits a 2-3 fold faster reaction rate than does the $HAuCl_4$ on the (111) textured surface, consistent with the data in **Figures 5.6 and 5.7**.

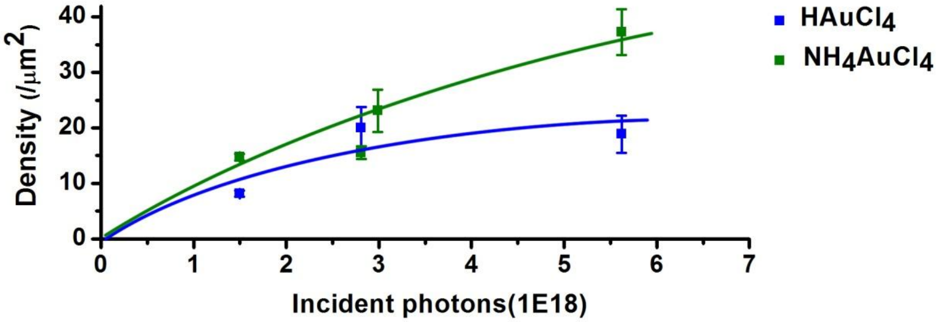

**Figure 5.15** – Comparison of the number density of $HAuCl_4$ and $NH_3AuCl_4$ based reactions on (111) textured PZT. The lines represent fitting to a simple nucleation theory.

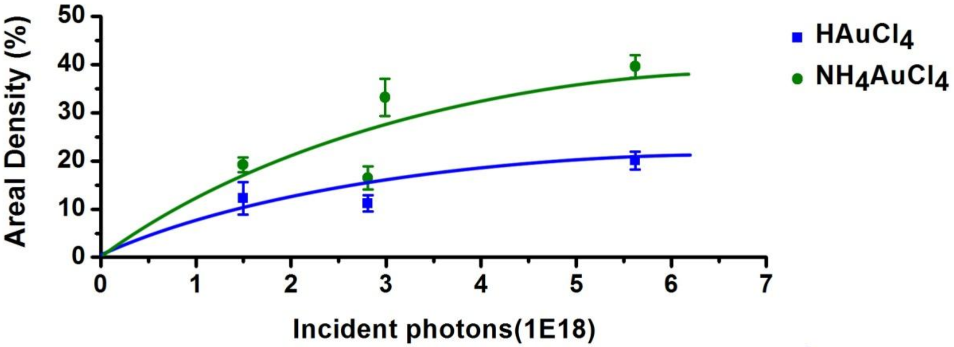

**Figure 5.16** – Comparison of the areal density of $HAuCl_4$ and $NH_3AuCl_4$ based reactions on (111) textured PZT. The lines represent fitting to a simple nucleation theory.

**Figure 5.17** shows that the deposition rate on the (100) textured surface is faster than on the (111) textured surface. The compositional ratio of Zr to Ti in the PZT is (30/70) so both surfaces are tetragonal and the substrate orientation dependence can be understood with reference to **Figure 5.16**. On the (100) surface, the polarization vector is perpendicular to the surface, while the vector direction for the (111) surface is inclined with respect to the surface. The resulting component of the vector normal to the surface on the (111) surface is approximately 70% of that of the (100) surface. This variation in the polarization magnitude affects the related charge at the surface and hence the band bending is less for the (111) surface compared to the (100) surface.

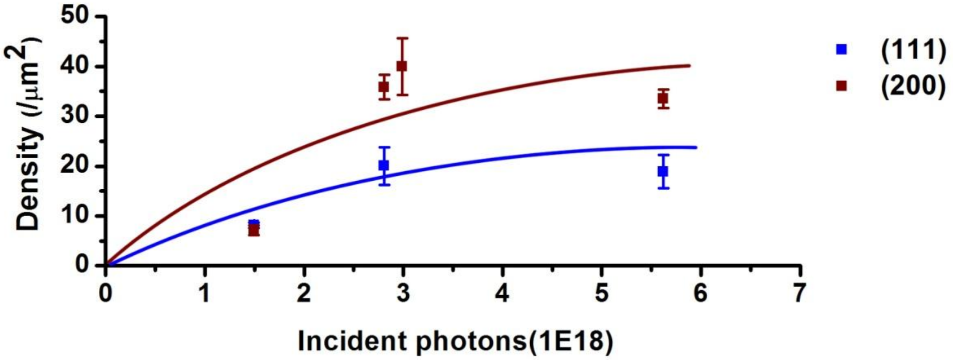

**Figure 5.17** - Comparison the number density of gold nanoparticles deposited from a solution of $HAuCl_4$ through a 270nm band pass filter on (111) and (100) textured PZT substrates. The lines represent fitting to a simple nucleation theory.

The lines in **Figures 5.15 - 5.17** represent fitting to a simple nucleation theory[112], where the density is of the form seen in Equation (29), where $d_o$ is the total density of particles, and α is the first order nucleation rate constant. This description assumes that the particles do not interact and the density is only a function of the ratio of unoccupied to occupied sites on the surface.

$$d = d_0 * (1 - \exp(-\propto (number\ of\ photons))) \qquad (29)$$

In the low concentration regime, the metal particle coverage increases while the particle size does not change systematically with reaction time. Furthermore, the particle size varies over a relatively small range (85nm-110nm) with narrow size distribution

(±10nm); whereas, the coverage increases from 0 to 40% over the measured illumination period. This implies that the growth rate of the particles is high, there is a limit on the size of the particles, and the increasing coverage reflects the nucleation rate. The reaction processes are illustrated schematically in **Figure 5.18**. The substrate with positive polarization has the electronic structure favorable for photo-reduction. The surface terminates with a positive charge, so a compensating Stern layer is present in the solution adjacent to the surface. Negatively charged tetrachlorauate $\{AuCl_4^-\}$ can participate in the Stern layer, rather than be a barrier as would occur with a positive ion.[70, 110] With initial illumination, the electrons migrate to the surface, react with the gold ions and produce a small metal cluster. When the cluster becomes sufficiently large to exhibit the continuum properties of the metal, an interface is formed and an interfacial barrier develops. Subsequent reaction requires that an electron from the bulk tunnel across the depletion region caused by the interfacial barrier. As the particle grows, the barrier increases until it reaches the value of a macroscopic interface. Liang et al has shown that the interface barrier at a metal-oxide interface is size dependent over the range of 1nm to 100nm, depending on the properties of the constituents.[113] As some point during the particle growth, the interfacial barrier and associated depletion width are too large to allow the electron tunneling and the reaction stops locally. Continued reduction requires a new nucleation site.

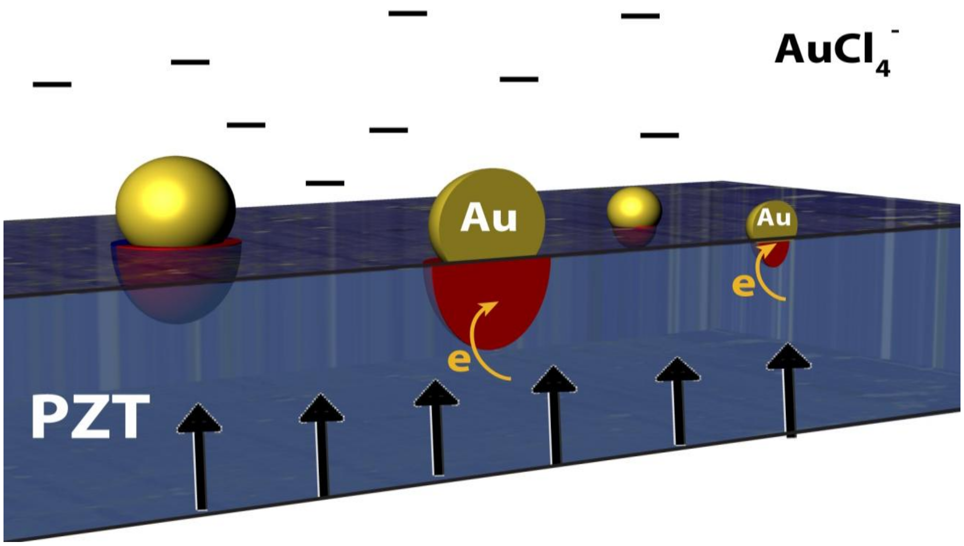

**Figure 5.18** - The reaction process on the surface is illustrated schematically. The substrate is polarized positively as indicated by the black arrows and results in a positive surface charge. A compensating cloud of negative ions forms in the solution near the surface and the $AuCl_4^-$ can contribute to the compensation. Initial reduction occurs in the absence of a barrier for electron transfer. As the nanoparticles increase in size, an interface barrier forms and causes an electron depletion region below the particle, indicated by the shaded region. The reaction will stop (the nanoparticle will stop growing) once the interfacial barrier is large enough that the depletion depth is larger than the tunneling distance.

In a simple model, the interfacial barrier is a function of the work function difference and the carrier concentration. These two variables are related to the depletion depth, $\chi_d$ that the electron must navigate as seen in Equation (30), where $\varepsilon_s$ is the permittivity, $\varphi_i$ is the built-in voltage, q is the charge, and $N_d$ is the carrier concentration.[114]

$$X_d = \sqrt{\frac{2\epsilon_s\varphi_i}{qN_d}} \tag{30}$$

The work function difference between gold and PZT is approximately 1eV, which corresponds to a large interfacial barrier at the macroscopic scale but the barrier would be smaller for small particles.  In this case, the carriers result from the optical absorption by the substrate, so the number is a function of the photon flux and absorption cross section. In our reactions, the photon flux is a constant, so when the particle reaches a size at which the interfacial barrier height and therefore, $\varphi_i$, is such that the depletion depth is larger than the tunneling distance, the particle stops growing.  This suggests that on any particular substrate, that the particle size can be controlled by changing the photon flux and the coverage controlled with the time and integrated photon flux.  The particle sizes in the range of 85nm here suggest that the growth stopped before the maximum interfacial barrier was reached.

Although the dipole induced band bending creates the states that allow photo-chemistry to occur, it is well known that the pH of the electrolyte solution can affect a semiconductor surface potential due either to surface adsorption or interaction with the Stern layers in solution.  The redox potential of the electrolyte will line up with the Fermi level of the ferroelectric.  In the case of metals such as Au, Ag or Pt, the redox potential is negative in relation to the standard hydrogen electrode (SHE), so there is no barrier to electrons from the ferroelectric into the solution.  However, typical potential shifts are in the range of 0.055V/pH unit[70].  The pH of the $HAuCl_4$ is approximately 0.1pH lower than that of the $NH_4AuCl_4$ at 1.1mM, which is too small to account for the difference in deposition rate.  Furthermore, the fact that the number density and areal coverage rates are fit well by first order nucleation theory, and the differences between the prefactors are consistent with the observed constant particle size suggests that differences are associated with the nucleation process.  Since the anion is the same for both systems, the coordination of the cations and the consequence to the interaction with the negative compensation layer in the liquid is the much more likely cause.

## 5.5. Wavelength dependent photoconductivity

The control of the size and density of metal nanoparticles now gives us a platform to create hybrid devices on a ferroelectric substrate by means of linking the deposited metal nanoparticles with novel molecules with unique optical and electrical properties. This platform also allows the study of the effects of a different substrate on the optical and electrical response of the assembly. The particle arrays are once again linked with photo-active dithiol-terminated *meso*-to-*meso* ethyne-bridged tris{porphyrinatoZn(II)} complex (dithiol-PZn$_3$). The structure of the dithiol-PZn$_3$ linked AuNP assemblies are shown in the SEM images in **Figure 5.19(a)** & **(b)** (Samples 1 and 2).

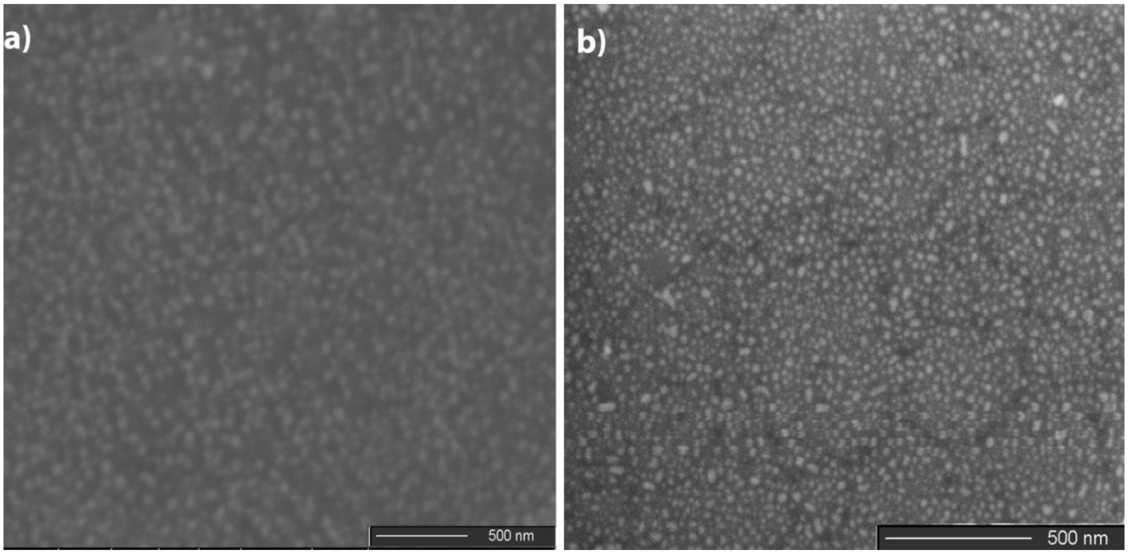

**Figure 5.19 –** (a) SEM image of 52nm AuNPs deposited on a PZT surface (b) SEM image of 25nm AuNPs deposited on a PZT surface.

Transport measurements confirm molecular connectivity between Au NPs, as devices sustain no current before reaction with dithiol-PZn$_3$but are conductive subsequent to the reaction. **Figure 5.20(a)** & **(b)** shows the wavelength dependent conductivities at 300K of the two PZn$_3$ linked AuNP hybrid assemblies seen in **Figure 5.19(a)** & **(b)**, respectively. Illumination with 655nm (red) and 533nm (green) wavelengths of light result in the differences in the photocurrent in **Figure 5.22(c)**; the green light induced photo current, $\Delta I_{green}$, is 6-14 times higher than the red light induced current $\Delta I_{red}$,.

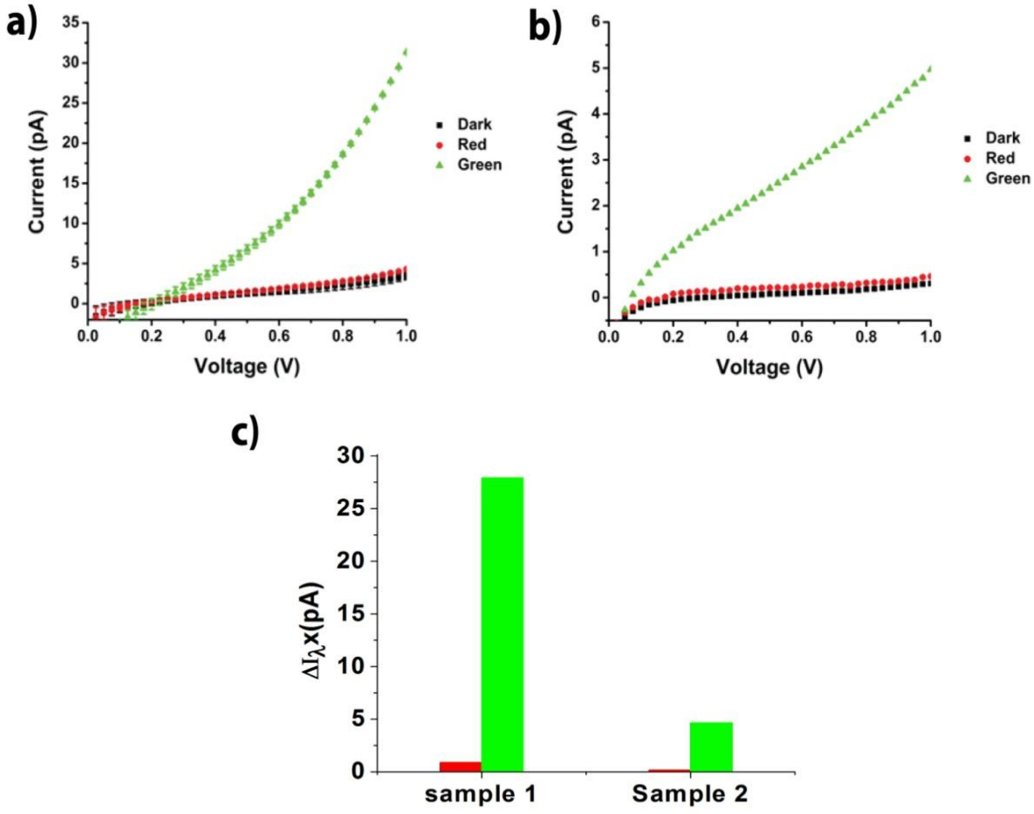

**Figure 5.20 –** (a) & (b) show the wavelength dependent conductivities at 300K of the two PZn$_3$ linked AuNP hybrid assemblies seen in **Figure 5.19(a)** & **(b)**, respectively. (c) shows the current enhancements for illumination with 655nm (red) and 533nm (green) light.

**Figure 5.21** compares the Fowler-Nordheim and dln(I)/dV as a function of voltage for Sample 1 and 2. **Figure 5.21(a)** & **(c)** are Fowler-Nordheim plots and **(b)** & **(d)** show dln(I)/dV as a function of voltage for the data in **Figure 5.20(a)** & **(b)**, respectively. The Fowler-Nordheim plots show a transition voltage of approximately 0.9V for Sample 1 & 2. Illumination with red light does not appear to affect the transition voltage, while illumination with green light results in no apparent transition voltage. The dln(I)/dV as a function of voltage exhibits no appreciable voltage dependence difference when illuminated with red or green light.

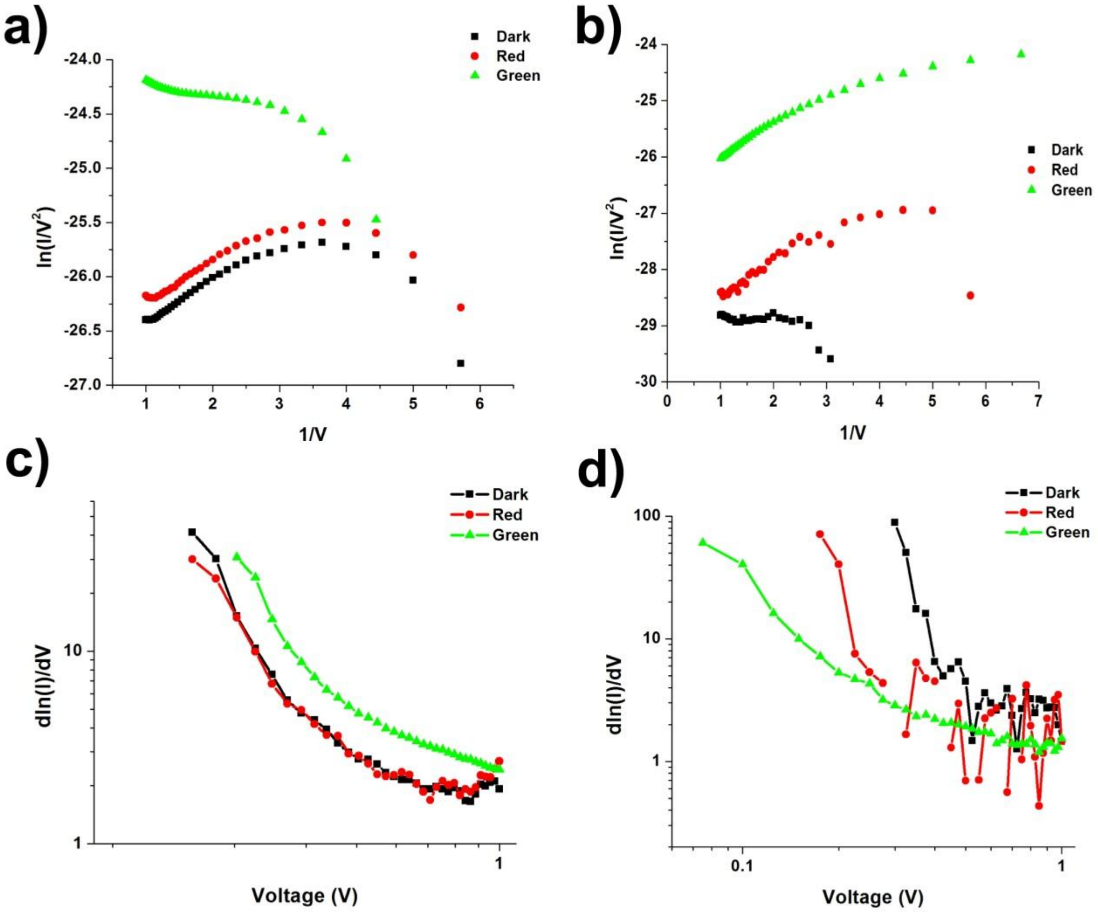

**Figure 5.21-** Fowler-Nordheim plots and dln(I)/dV as a function of voltage for Sample 1 and 2. (a) & (c) are Fowler-Nordheim plots and (b) & (d) show dln(I)/dV as a function of voltage for the data in **Figure 5.20(a)** & **(b)**, respectively

As can be seen in the SEM micrographs, the hybrid nanostructure can be realized only if the nanoparticle separation is a multiple of the length of the molecule, which is 4.6nm for the trimer. This wavelength dependence in photoconductivity is not expected from the optical properties of the porphyrin; however, nanoparticle arrays often exhibit plasmonic properties that are dependent on the material, shape and coupling of the particles and the dielectric constant of the environment. The AuNP arrays on glass in Chapter 4 showed that the AuNP's can enhance photocurrent at wavelengths associated with plasmon resonances.[115] The effect was attributed to field focusing and increased photon flux at the junctions. In that case, the photoconduction was significantly enhanced at both red and green wavelengths.

The differences in these results can be understood in terms of the factors that affect the plasmon spectrum. The primary (transverse) peak for non-coupled gold nanoparticles is in the range of 520-580nm.[35] Upon deposition of the particles on glass slides the peak is red shifted and broadened. When the particle-particle separation is on the order of 1-4 nm (depending on the particle size) the particles are coupled and a second peak (longitudinal) at 580-670nm develops.[35] One difference between the two studies is that the dielectric constant of PZT is 2.5 times that of glass. Recently, Ringe et al reported that an increase in the dielectric of the substrate by a factor of 2 could red shift the proximal plasmon peaks by ~20 nm[116]. While this effect might alter the magnitude of the green enhancement, it cannot explain the lack of red enhancement. We note that both the size and shapes of particles are similar in both cases. The particle sizes in **Figure 5.19(a)** & **(b)** are 52 nm and 25 nm, for samples 1 and 2, respectively; while those in

**Figure 4.1(b)** are 32nm and the micrographs in both cases show roughly spherical particles. Therefore the difference in enhancement, i.e. the absence of the red enhancement in **Figure 5.20**, is not due to differences in particle size or shape. Since the red absorption is associated with the longitudinal peak, the absence of red enhancement implies a lack of coupling between the particles. The lack of coupling indicates that the particles are separated by more than a single trimer molecular bridge. It has been found theoretically and experimentally that a separation between particles of (9nm), the length of a double trimer bridge, is sufficient to reduce or preclude coupling.[35] Therefore, the photocurrent in this device arises predominantly from the interaction of the transverse plasmon induced current, further illustrating the potential to create devices with a range of function.

### 5.6. Temperature dependent conductivity

The voltage and temperature dependence was further explored for a sample similar to the AuNP array seen in **Figure 5.19(a)**. Once again, the transport measurements confirm molecular connectivity between Au NPs, as devices sustain no current before reaction with dithiol-PZn$_3$but are conductive subsequent to the reaction. **Figure 5.22(a)** shows that conductivity response at 238K and the insert shows that illumination with green light exhibits a larger current enhancement than illumination with red light at 1V. The Fowler-Nordheim plot in **Figure 5.22(b)** shows that the dark current and illumination with red light have a transition voltage of 2.5eV and illumination with green light shows no transition voltage. The thermionic emission and Arrhenius plots, **Figure 5.22(c)** & **(d)**, respectively, both show that the barrier is unaffected by illumination with red light and illumination with green light reduces the barrier to basically zero. The Arrhenius plots show a reduction in the activation energy from 186meV to 15.6meV for dark & illumination with red light to illumination with green light, respectively.

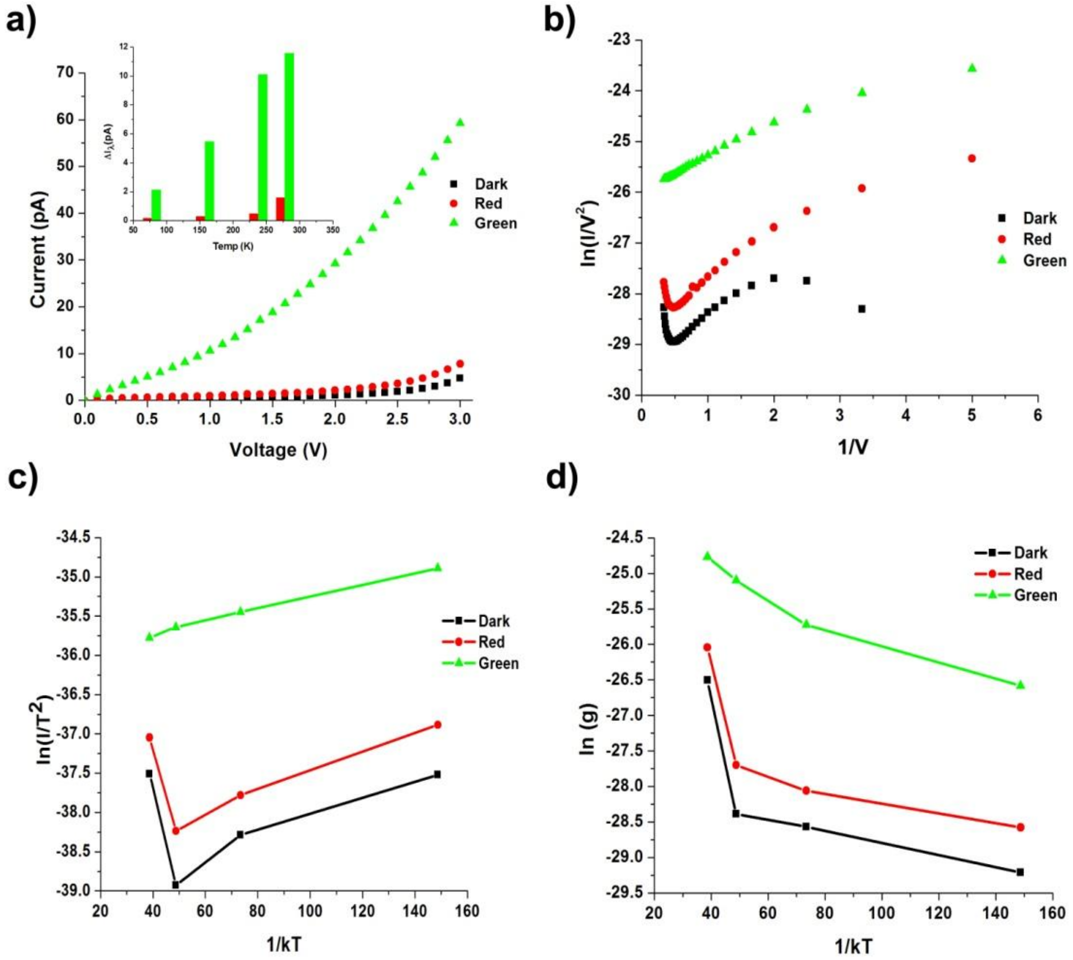

**Figure 5.22** - (a) wavelength dependent conductivity response and the insert shows that illumination with green light exhibits a larger current enhancement than illumination with red light. (b) Fowler-Nordheim plot which shows that the dark current and illumination with red light have a transition voltage of 2.5V and illumination with green light shows no transition voltage. (c) & (d) show the data in (a) linearized as ln(I/T$^2$) as a function of 1/kT to distinguish thermionic emission and logarithm of the conductance as a function of 1/kT, respectively.

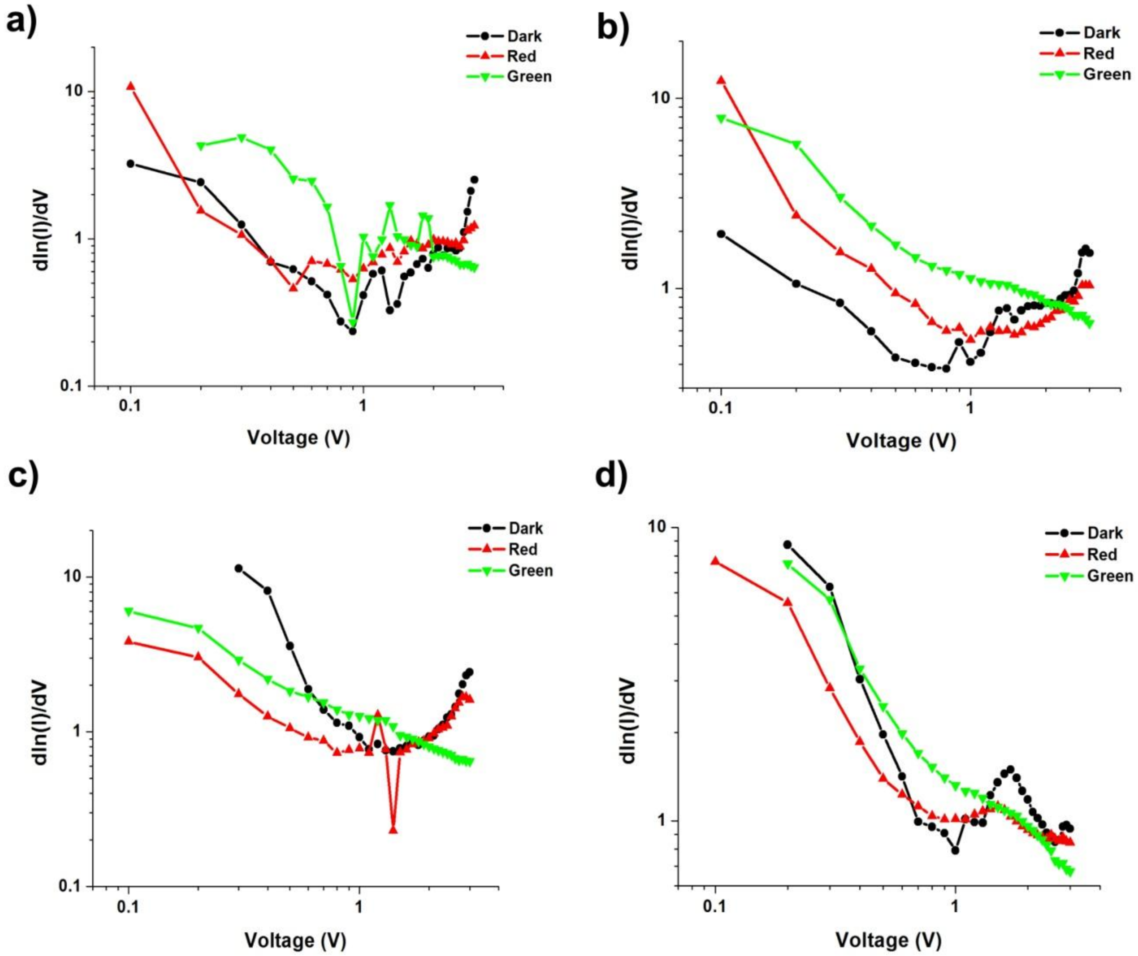

**Figure 5.23 -** dln(I)/dV as a function of voltage, where **(**a – d) represent the dln(I)/dV plots at 78K, 158K, 238K, and 278K, respectively.

**Figure 5.23(a-d)** shows the dln(I)/dV as a function of voltage for the conductivity data represented in the insert of **Figure 5.22(a)**. The data shows that illumination with red light does not appreciable change in the voltage dependence, while illumination with green light shows a change in the voltage dependence above 1V. Analysis of conductivity shows similar behavior to that of the non-linear case in Chapter 4. As in that case, the voltage and temperature dependencies indicate multiple charge transport mechanism are present and the effect of light that excites surface plasmons is reflected in the effect on the barrier height. Both the Fowler-Nordheim and thermionic emission model indicate a larger apparent barrier height with the ferroelectric substrate. As in the cases above, the current enhancement in this device arises predominantly from the interaction of the transverse plasmon induced current. The variation in the magnitudes of the current enhancements across the samples is due to the variation in the particle size, spacing, and dielectric constant of the substrate.

# 6. Conclusions and Future Work

## 6.1. Conclusions

One of the major contribution of this work has been the development of a technique to provide an avenue to overcome the challenges of combining the self-assembly of dissimilar components with unique properties with lithographic patterning. Ferroelectric Nanolithography (FNL) offers the potential to assemble dissimilar components but until now, the process had not demonstrated the ability to create multi-functional hybrid devices. The development of these hybrid devices with multiple components led to the determination of transport and photoconduction mechanisms that dominate the device performance. Understanding the transport mechanisms on glass, develop a similar deposition technique, then understanding the mechanisms of the growth mechanisms on ferroelectric surfaces has provided a template to develop devices with a wide range of opto-electrical behavior.

AuNP assemblies on glass substrates were synthesis to isolate the particle spacing and size distribution to quantify the charge transport mechanisms and isolate the roll of the optical absorption spectra on the opto-electrical response of the hybrid device structure. Employing amino-silane functionalized glass substrates and citrate-reduced AuNPs, this work demonstrated the ability to create reproducible AuNP structures with empirical control of the surface coverage and conductivity. The AuNP arrays were systematically varied by size, distribution, and attached zinc-porphyrin molecules, which exhibited a wide range of conductance responses. The analysis of the dark conductivity data showed that the transport results from thermally assisted tunneling in arrays exhibiting near-linear current-voltage behavior and from tunneling at low temperatures with multiple mechanisms at higher temperatures in arrays exhibiting non-linear current-voltage behavior. It was found that the parameters that dictated the ultimate current magnitude were the particle work function, molecular surface coverage, and particle separation. Photoconduction in these systems was found to result from multiple mechanisms. The parameters that dictate the ultimate magnitude of the current enhancement are the attached molecule, interfacial barriers, and optical coupling between nanoparticles. Control of the interfacial barrier and coupling between nanoparticles can result in anomalously high red and green current enhancements, which were found to be the result of either direct exciton formation in the molecule, hot electron and field effect (optical antenna) from surface plasmon interaction between the AuNPs and the molecules.

The results on hybrid porphyrin-AuNP assemblies on glass demonstrated that multiple transport mechanisms occur simultaneously and a complex relationship between the plasmon resonance of the assemblies and the photoconductance occurs. This provided a basis on which to examine the properties of hybrid assembles on ferroelectric substrates. Unlike the deposition of the AuNPs on glass, in which size and surface coverage were controlled by citrate reduction and immersion time, the size and surface coverage are controlled by the nucleation and growth of metal nanoparticles on the ferroelectric substrate. In order to isolate the relevant parameters that control the size, spacing, and distribution, systematic variation of the domain orientation, crystal orientation, photon flux, optical power and electrolyte solution were used to determine the nucleation and growth mechanism of nanoparticles. The deposition was much faster on upwardly poled domains compared to downwardly poled domain. The (100) textured surface produced higher density AuNP arrays under the same deposition conditions as compared to the (111) textured surface due to difference in the magnitude of the polarization vector. Analysis of the particle growth and surface coverage found that over the time scale in which the deposition process occur, that a small particle size range was produced but a large increase in the surface coverage was observed. This implies that the growth rate of the particles is high, there is a limit on the size of the particles, and the increasing coverage reflects the nucleation rate. The carriers result from the optical absorption by the substrate, so the number was a function of the photon flux and absorption cross section. In these experiments, the photon flux was a constant, so when the particle reached a size at which the interfacial barrier height was such that the depletion depth was larger than the tunneling distance, the particle stopped growing. This suggests that on any particular substrate, that the particle size can be controlled by changing the photon flux and the coverage controlled with the time and integrated photon flux.

The determination of the growth mechanisms of AuNP on ferroelectric surfaces allowed FNL to be utilized to selectively deposit AuNP arrays and realize a hybrid device structure. The hybrid devices on PZT showed a very large green current enhancement compared to illumination with red light. The SEM micrographs indicate that the particles must be linked by more than a single trimer molecular bridge. The length of this double trimer bridge is sufficient to reduce or preclude coupling. Therefore, the photocurrent in this device arises predominantly from the interaction of the transverse plasmon induced current, further illustrating the potential to create devices with a range of function.

These results define a pathway for FNL to be used to pattern a wide range of mulit-component structures with applications ranging from optoelectronics to energy harvesting. The size and separation of the AuNPs can be easily used to tune the coupling of the surface plasmons and the resulting plasmonic properties. Since molecular compounds exhibit a wide range of optical and electrical properties, the possibilities as a multi-functional device platform can be realized.

## 6.2. Suggestions for future work

Future studies of the deposition process and transport mechanisms would provide more insight into creating hybrid device structures. One of the determine factors in the deposition mechanisms on ferroelectric surfaces is the domain size of the substrate. The study of the growth mechanisms as a function of the domain size would allow the relationship between the interfacial barrier height, depletion depth, and particle size to be more clearly understood. Employing thin films or single crystals with precise control of the grain and domain size would also provide an avenue to develop AuNP arrays with more control over the size and spacing of the nanoparticles. This control would allow the tunability of the surface plasmons to be further studied and provide greater control over the wavelength dependent current enhancements.

The transition from transport that shows near-linear and non-linear conductivity responses needs to be explored further. Understanding the origins of the extra barrier at the interface would provide better understanding of the dominate transport mechanisms.

To further investigate the role of hot electrons versus the field effect, the current enhancements as a function of optical power would provide an understanding of the exciton formation and the relationship to incited photons. Coupled with the power study, the role of the coupling peak as an indication of the coupling between AuNPs needs to be determined. Continuing to increase the size, density, and distribution of the nanoparticle arrays would provide a pathway to vary the amplitude and peak position from the visible into the IR. This would allow the interaction with the IR peak of the zinc-porphyrin molecules to be determined. This would also provide a basis to add to the understanding from the power dependency by manipulating the absorption peaks to not overlap with the molecules absorption maximum and determine the contributions from hot electrons and field effect on the photocurrent. This work explored only three wavelengths of light, but studying the current enhancements as a function of the full spectrum would provide insight into the actual absorption characteristics of the AuNP linked with the various molecules.

Finally, this approach can now be generalized to an extensive array of device configurations utilizing organic as well as inorganic compounds, on thin films, single crystals, and polycrystalline substrates, producing a variety of molecule-nanoparticle combinations with unique and novel properties. The extension of this work with other optical active molecules, chemistries, and surfaces provides an unlimited number of variables to create varied hybrid device structures with diverse property sets.

1. Hoppe, H. and N.S. Sariciftci, *Organic solar cells: An overview.* Journal of Materials Research, 2004. **19**(7): p. 1924-1945.

2. Coakley, K.M. and M.D. McGehee, *Conjugated polymer photovoltaic cells.* Chemistry of Materials, 2004. **16**(23): p. 4533-4542.

3. Hirsch, L.R., et al., *Nanoshell-mediated near-infrared thermal therapy of tumors under magnetic resonance guidance.* Proceedings of the National Academy of Sciences of the United States of America, 2003. **100**(23): p. 13549-13554.

4. Geim, A.K. and K.S. Novoselov, *The rise of graphene.* Nature Materials, 2007. **6**(3): p. 183-191.

5. Robertson, J., *High dielectric constant gate oxides for metal oxide Si transistors.* Reports on Progress in Physics, 2006. **69**(2): p. 327-396.

6. Rand, B.P., P. Peumans, and S.R. Forrest, *Long-range absorption enhancement in organic tandem thin-film solar cells containing silver nanoclusters.* Journal of Applied Physics, 2004. **96**(12): p. 7519-7526.

7. Matyjaszewski, K. and N.V. Tsarevsky, *Nanostructured functional materials prepared by atom transfer radical polymerization.* Nature Chemistry, 2009. **1**(4): p. 276-288.

8. Dulcey, C.S., et al., *DEEP UV PHOTOCHEMISTRY OF CHEMISORBED MONOLAYERS - PATTERNED COPLANAR MOLECULAR ASSEMBLIES.* Science, 1991. **252**(5005): p. 551-554.

9. Whitesides, G.M. and B. Grzybowski, *Self-assembly at all scales.* Science, 2002. **295**(5564): p. 2418-2421.

10. Reed, M.A., et al., *Conductance of a molecular junction.* Science, 1997. **278**(5336): p. 252-254.

11. Mirkin, C.A., et al., *A DNA-based method for rationally assembling nanoparticles into macroscopic materials.* Nature, 1996. **382**(6592): p. 607-609.

12. Mirkin, C.A. and M.A. Ratner, *MOLECULAR ELECTRONICS.* Annual Review of Physical Chemistry, 1992. **43**: p. 719-754.

13. Yao, Z., et al., *Carbon nanotube intramolecular junctions.* Nature, 1999. **402**(6759): p. 273-276.

14. Mantooth, B.A. and P.S. Weiss, *Fabrication, assembly, and characterization of molecular electronic components.* Proceedings of the Ieee, 2003. **91**(11): p. 1785-1802.

15. Strachan, D.R., et al., *Clean electromigrated nanogaps imaged by transmission electron microscopy.* Nano Letters, 2006. **6**(3): p. 441-444.

16. Velegol, D., *Assembling colloidal devices by controlling interparticle forces.* Journal of Nanophotonics, 2007. **1**: p. 25.

17. Vanmaekelbergh, D. and P. Liljeroth, *Electron-conducting quantum dot solids: novel materials based on colloidal semiconductor nanocrystals.* Chemical Society Reviews, 2005. **34**(4): p. 299-312.

18. Zabet-Khosousi, A. and A.A. Dhirani, *Charge transport in nanoparticle assemblies.* Chemical Reviews, 2008. **108**(10): p. 4072-4124.

19. Beloborodov, I.S., et al., *Granular electronic systems.* Reviews of Modern Physics, 2007. **79**(2): p. 469-518.

20. Mermin, A.a., *Solid State Physics*. 1976.

21. Schmid, G. and U. Simon, *Gold nanoparticles: assembly and electrical properties in 1-3 dimensions.* Chemical Communications, 2005(6): p. 697-710.

22. Franke, M.E., T.J. Koplin, and U. Simon, *Metal and Metal Oxide Nanoparticles in Chemiresistors: Does the Nanoscale Matter?* Small, 2006. **2**(1): p. 36-50.

23. Herrmann, J., et al., *Tuning the Coulomb charging energy in cross-linked nanoparticle films.* Physical Review B, 2007. **76**(21): p. 212201.

24. Zabet-Khosousi, A., et al., *Metal to insulator transition in films of molecularly linked gold nanoparticles.* Physical Review Letters, 2006. **96**(15).

25. Dunford, J.L., et al., *Quasilocalized hopping in molecularly linked Au nanoparticle arrays near the metal-insulator transition.* Physical Review B, 2005. **72**(7).

26. Escorcia, A. and A.A. Dhirani, *Electrochemical properties of ferrocenylalkane dithiol-gold nanoparticle films prepared by layer-by-layer self-assembly.* Journal of Electroanalytical Chemistry, 2007. **601**(1-2): p. 260-268.

27. Trudeau, P.E., A. Escorcia, and A.A. Dhirani, *Variable single electron charging energies and percolation effects in molecularly linked nanoparticle films.* Journal of Chemical Physics, 2003. **119**(10): p. 5267-5273.

28. Trudeau, P.E., et al., *Competitive transport and percolation in disordered arrays of molecularly-linked Au nanoparticles.* Journal of Chemical Physics, 2002. **117**(8): p. 3978-3981.

29. Zabet-Khosousi, A. and A.A. Dhirani, *Shadow mask fabrication of micron-wide break-junctions and their application in single-nanoparticle devices.* Nanotechnology, 2007. **18**(45).

30. Zabet-Khosousi, A., et al., *Influence of linker molecules on charge transport through self-assembled single-nanoparticle devices.* Physical Review Letters, 2005. **94**(9).

31. Simmons, J.G., *Generalized Formula for the Electric Tunnel Effect between Similar Electrodes Separated by a Thin Insulating Film.* Journal of Applied Physics, 1963. **34**(6): p. 1793-1803.

32. Beebe, J.M., et al., *Measuring relative barrier heights in molecular electronic junctions with transition voltage spectroscopy.* ACS Nano, 2008. **2**(5): p. 827-32.

33. Maksymovych, P., et al., *Scaling and disorder analysis of local I-V curves from ferroelectric thin films of lead zirconate titanate.* Nanotechnology, 2011. **22**(25).

34. Creighton, J.A., C.G. Blatchford, and M.G. Albrecht, *Plasma resonance enhancement of Raman scattering by pyridine adsorbed on silver or gold sol particles of size comparable to the excitation wavelength.* Journal of the Chemical Society, Faraday Transactions 2: Molecular and Chemical Physics, 1979. **75**: p. 790-798.

35. Ghosh, S.K. and T. Pal, *Interparticle coupling effect on the surface plasmon resonance of gold nanoparticles: From theory to applications.* Chemical Reviews, 2007. **107**(11): p. 4797-4862.

36. Hentschel, M., et al., *Plasmonic Oligomers: The Role of Individual Particles in Collective Behavior.* ACS Nano, 2011. **5**(3): p. 2042-2050.

37. Noguez, C., *Surface plasmons on metal nanoparticles: The influence of shpae and physical environment.* Journal of Physical Chemistry C, 2007. **111**(10): p. 3806-3819.

38. Baletto, F. and R. Ferrando, *Structural properties of nanoclusters: Energetic, thermodynamic, and kinetic effects.* Reviews of Modern Physics, 2005. **77**(1): p. 371-423.

39. Kushmerick, J.G., et al., *Effect of bond-length alternation in molecular wires.* Journal of the American Chemical Society, 2002. **124**(36): p. 10654-5.

40. Mangold, M.A., et al., *Surface plasmon enhanced photoconductance of gold nanoparticle arrays with incorporated alkane linkers.* Applied Physics Letters, 2009. **94**(16): p. -.

41. Wang, W., T. Lee, and M.A. Reed, *Mechanism of electron conduction in self-assembled alkanethiol monolayer devices.* Physical Review B, 2003. **68**(3): p. 035416.

42. Selzer, Y., et al., *Thermally Activated Conduction in Molecular Junctions.* Journal of the American Chemical Society, 2004. **126**(13): p. 4052-4053.

43. O'Neill, L. and H.J. Byrne, *Structure-property relationships for electron-vibrational coupling in conjugated organic oligomeric systems.* Journal of Physical Chemistry B, 2005. **109**(26): p. 12685-12690.

44. Wu, S.W., N. Ogawa, and W. Ho, *Atomic-scale coupling of photons to single-molecule junctions.* Science, 2006. **312**(5778): p. 1362-5.

45. Nakanishi, H., et al., *Photoconductance and inverse photoconductance in films of functionalized metal nanoparticles.* Nature, 2009. **460**(7253): p. 371-375.

46. Park, T.-H., *Synthesis and applications of carbodithioate-terminated aryleneethynylenes,* in *Chemistry*. 2008, University of Pennsylvania: Philadelphia.

47. Kocherzhenko, A.A., et al., *Mechanism of charge transport along zinc porphyrin-based molecular wires.* Journal of the American Chemical Society, 2009. **131**(15): p. 5522-9.

48. Park, T.H. and M.J. Therien, *Carbodithioate-terminated oligo(phenyleneethynylene)s: Synthesis and surface functionalization of gold nanoparticles.* Organic Letters, 2007. **9**(15): p. 2779-2782.

49. Duncan, T.V., et al., *Exceptional Near-Infrared Fluorescence Quantum Yields and Excited-State Absorptivity of Highly Conjugated Porphyrin Arrays.* Journal of the American Chemical Society, 2006. **128**(28): p. 9000-9001.

50. Lin, V.S.Y., S.G. DiMagno, and M.J. Therien, *Highly conjugated, acetylenyl bridged porphyrins: New models for light- harvesting antenna systems.* Science, 1994. **264**(5162): p. 1105-1111.

51. Lin, V.S.Y. and M.J. Therien, *The Role of Porphyrin-to-Porphyrin Linkage Topology in the Extensive Modulation of the Absorptive and Emissive Properties of a Series of Ethynyl- and Butadiynyl-Bridged Bis- and Tris(porphinato)zinc Chromophores.* Chemistry – A European Journal, 1995. **1**(9): p. 645-651.

52. Rubtsov, I.V., et al., *Ultrafast Singlet Excited-State Polarization in Electronically Asymmetric Ethyne-Bridged Bis[(porphinato)zinc(II)] Complexes.* Journal of the American Chemical Society, 2003. **125**(9): p. 2687-2696.

53. Susumu, K., et al., *Conjugated Chromophore Arrays with Unusually Large Hole Polaron Delocalization Lengths.* Journal of the American Chemical Society, 2006. **128**(26): p. 8380-8381.

54. Lin, V.S.Y., S.G. DiMagno, and M.J. Therien, *Highly Conjugated, Acetylenyl Bridged Porphyrins: New Models for Light-Harvesting Antenna Systems.* Science, 1994. **264**(5162): p. 1105-1111.

55. Park, B.H., et al., *Lanthanum-substituted bismuth titanate for use in non-volatile memories.* Nature, 1999. **401**(6754): p. 682-684.

56. Yuan, Y., et al., *Efficiency enhancement in organic solar cells with ferroelectric polymers.* Nat Mater, 2011. **10**(4): p. 296-302.

57. Setter, N., et al., *Publisher's Note: ``Ferroelectric thin films: Review of materials, properties, and applications'' [J. Appl. Phys. [bold 100], 051606 (2006)].* Journal of Applied Physics, 2006. **100**(10): p. 109901-1.

58. Tadigadapa, S. and K. Mateti, *Piezoelectric MEMS sensors: state-of-the-art and perspectives.* Measurement Science & Technology, 2009. **20**(9): p. -.

59. Watson, B., J. Friend, and L. Yeo, *Piezoelectric ultrasonic micro/milli-scale actuators.* Sensors and Actuators a-Physical, 2009. **152**(2): p. 219-233.

60. Balke, N., et al., *Electromechanical Imaging and Spectroscopy of Ferroelectric and Piezoelectric Materials: State of the Art and Prospects for the Future.* Journal of the American Ceramic Society, 2009. **92**(8): p. 1629-1647.

61. Kalinin, S.V., et al., *Ferroelectric Lithography of Multicomponent Nanostructures.* Advanced Materials, 2004. **16**(9-10): p. 795-799.

62. Li, D.B., et al., *Polarization reorientation in ferroelectric lead zirconate titanate thin films with electron beams.* Journal of Materials Research, 2006. **21**(04): p. 935-940.

63. Kholkin, A.L., S.O. Iakovlev, and J.L. Baptista. *Polarization control and domain manipulation in ferroelectric films with UV light*. 2001.

64. Wu, A., et al., *Domain populations in lead zirconate titanate thin films of different compositions via piezoresponse force microscopy.* Nanotechnology, 2005. **16**(11): p. 2587-2595.

65. Khaenamkaew, P., et al., *Effect of Zr/Ti ratio on the microstructure and ferroelectric properties of lead zirconate titanate thin films.* Materials Chemistry and Physics, 2007. **102**(2-3): p. 159-164.

66. Gruverman, A. and A. Kholkin, *Nanoscale ferroelectrics: processing, characterization and future trends.* Reports on Progress in Physics, 2006. **69**(8): p. 2443-2474.

67. Kalinin, S.V. and D.A. Bonnell, *Local potential and polarization screening on ferroelectric surfaces.* Physical Review B, 2001. **63**(12).

68. Gruverman, A. and S.V. Kalinin, *Piezoresponse force microscopy and recent advances in nanoscale studies of ferroelectrics.* Journal of Materials Science, 2006. **41**(1): p. 107-116.

69. Yang, W.C., et al., *Photo electron emission microscopy of polarity-patterned materials.* Journal of Physics-Condensed Matter, 2005. **17**(16): p. S1415-S1426.

70. Tiwari, D. and S. Dunn, *Photochemistry on a polarisable semi-conductor: what do we understand today?* Journal of Materials Science, 2009. **44**(19): p. 5063-5079.

71. Tybell, T., C.H. Ahn, and J.M. Triscone, *Control and imaging of ferroelectric domains over large areas with nanometer resolution in atomically smooth epitaxial Pb(Zr0.2Ti0.8)O-3 thin films.* Applied Physics Letters, 1998. **72**(12): p. 1454-1456.

72. S. V. Kalinin, D.A.B.T.A.X.L.Z.H.R.S.J.H.F., *Ferroelectric Lithography of Multicomponent Nanostructures.* Advanced Materials, 2004. **16**(9-10): p. 795-799.

73. Burbure, N.V., P.A. Salvador, and G.S. Rohrer, *Influence of Dipolar Fields on the Photochemical Reactivity of Thin Titania Films on BaTiO3 Substrates.* Journal of the American Ceramic Society, 2006. **89**(9): p. 2943-2945.

74. Lei, X., et al., *In situ deposition/positioning of magnetic nanoparticles with ferroelectric nanolithography.* Journal of Materials Research, 2005. **20**(03): p. 712-718.

75. Shao, R., M.P. Nikiforov, and D.A. Bonnell, *Photoinduced charge dynamics on BaTiO3(001) surface characterized by scanning probe microscopy.* Applied Physics Letters, 2006. **89**(11): p. 3.

76. Zhao, M.H., D.A. Bonnell, and J.M. Vohs, *Effect of ferroelectric polarization on the adsorption and reaction of ethanol on BaTiO3.* Surface Science, 2008. **602**(17): p. 2849-2855.

77. Zhao, M.H., D.A. Bonnell, and J.M. Vohs, *Ferroelectric polarization dependent interactions at Pd--LiNbO[sub 3](0001) interfaces.* Journal of Vacuum Science & Technology A: Vacuum, Surfaces, and Films, 2009. **27**(6): p. 1337-1342.

78. Altman, E.I. and U.D. Schwarz, *Mechanisms, Kinetics, and Dynamics of Oxidation and Reactions on Oxide Surfaces Investigated by Scanning Probe Microscopy.* Advanced Materials, 2010. **22**(26-27): p. 2854-2869.

79. Garra, J., J.M. Vohs, and D.A. Bonnell, *Defect-mediated adsorption of methanol and carbon dioxide on BaTiO[sub 3](001).* Journal of Vacuum Science & Technology A: Vacuum, Surfaces, and Films, 2009. **27**(5): p. L13-L17.

80. Li, D.B., et al., *Direct in situ determination of the polarization dependence of physisorption on ferroelectric surfaces.* Nature Materials, 2008. **7**(6): p. 473-477.

81. Zhao, M.H., D.A. Bonnell, and J.M. Vohs, *Influence of ferroelectric polarization on the energetics of the reaction of 2-fluoroethanol on BaTiO3.* Surface Science, 2009. **603**(2): p. 284-290.

82. Rankin, C., et al., *Polarization and Local Reactivity on Organic Ferroelectric Surfaces: Ferroelectric Nanolithography Using Poly(vinylidene fluoride).* ACS Nano, 2007. **1**(3): p. 234-238.

83. Li, D. and D.A. Bonnell, *Ferroelectric lithography.* Ceramics International, 2008. **34**(1): p. 157-164.

84. Giocondi, J.L., P.A. Salvador, and G.S. Rohrer. *The origin of photochemical anisotropy in SrTiO3*. 2007.

85. Hanson, J.N., et al., *Fabrication of metallic nanowires on a ferroelectric template via photochemical reaction.* Nanotechnology, 2006. **17**(19): p. 4946-4949.

86. Dunn, S., P.M. Jones, and D.E. Gallardo, *Photochemical growth of silver nanoparticles on c(-) and c(+) domains on lead zirconate titanate thin films.* Journal of the American Chemical Society, 2007. **129**(28): p. 8724-8728.

87. Li, D. and D.A. Bonnell, *Controlled Patterning of Ferroelectric Domains: Fundamental Concepts and Applications.* Annual Review of Materials Research, 2008. **38**(1): p. 351-368.

88. Kalinin, S.V., et al., *Atomic polarization and local reactivity on ferroelectric surfaces: A new route toward complex nanostructures.* Nano Letters, 2002. **2**(6): p. 589-593.

89. Giocondi, J.L. and G.S. Rohrer, *Structure sensitivity of photochemical oxidation and reduction reactions on SrTiO3 surfaces.* Journal of the American Ceramic Society, 2003. **86**(7): p. 1182-1189.

90. Turkevich, J., P.C. Stevenson, and J. Hillier, *A study of the nucleation and growth processes in the synthesis of colloidal gold.* Discussions of the Faraday Society, 1951. **11**: p. 55-75.

91. Beverly, K.C., J.F. Sampaio, and J.R. Heath, *Effects of Size Dispersion Disorder on the Charge Transport in Self-Assembled 2-D Ag Nanoparticle Arrays.* The Journal of Physical Chemistry B, 2002. **106**(9): p. 2131-2135.

92. Remacle, F., et al., *Conductivity of 2-D Ag Quantum Dot Arrays: Computational Study of the Role of Size and Packing Disorder at Low Temperatures.* The Journal of Physical Chemistry B, 2002. **106**(16): p. 4116-4126.

93. Black, C.T., et al., *Spin-Dependent Tunneling in Self-Assembled Cobalt-Nanocrystal Superlattices.* Science, 2000. **290**(5494): p. 1131-1134.

94. Wuelfing, W.P. and R.W. Murray, *Electron Hopping through Films of Arenethiolate Monolayer-Protected Gold Clusters.* The Journal of Physical Chemistry B, 2002. **106**(12): p. 3139-3145.

95. Kemeny, G. and Rosenber.B, *Small Polarons in Organic and Biological Semiconductors.* Journal of Chemical Physics, 1970. **53**(9): p. 3549-&.

96. Kemeny, G. and Rosenber.B, *Throry of Pre-Exponential Factor in Organic Semiconductors.* Journal of Chemical Physics, 1970. **52**(8): p. 4151-&.

97. Roberts, G.G., *Thermally Assisted Tunnelling and Pseudointrinsic Conduction - 2 Mechanisms to Explain Meyer-Neldel Rule.* Journal of Physics Part C Solid State Physics, 1971. **4**(18): p. 3167-&.

98. Polanco, J.I. and G.G. Roberts, *Thermally Assisted Tunnelling in Dielectric Films (Ii).* Physica Status Solidi a-Applied Research, 1972. **13**(2): p. 603-&.

99. Murphy, E.L. and R.H. Good, *Thermionic Emission, Field Emission, and the Transition Region.* Physical Review, 1956. **102**(6): p. 1464-1473.

100. Forbes, R.G., *Simple good approximations for the special elliptic functions in standard Fowler-Nordheim tunneling theory for a Schottky-Nordheim barrier.* Applied Physics Letters, 2006. **89**(11).

101. Zangmeister, C.D., et al., *Fermi level alignment in self-assembled molecular layers: The effect of coupling chemistry.* Journal of Physical Chemistry B, 2006. **110**(34): p. 17138-17144.

102. Zangmeister, C.D., et al., *Fermi level alignment and electronic levels in "molecular wire" self-assembled monolayers on au.* Journal of Physical Chemistry B, 2004. **108**(41): p. 16187-16193.

103. Susumu, K. and M.J. Therien, *Decoupling optical and potentiometric band gaps in pi-conjugated materials.* Journal of the American Chemical Society, 2002. **124**(29): p. 8550-8552.

104. Binh, V.T., et al., *Low work-function cathodes from Schottky to field-induced ballistic electron emission: Self-consistent numerical approach.* Physical Review B, 2007. **75**(4).

105. Xue, Y., S. Datta, and M.A. Ratner, *Charge transfer and ``band lineup'' in molecular electronic devices: A chemical and numerical interpretation.* The Journal of Chemical Physics, 2001. **115**(9): p. 4292-4299.

106. Frail, P.R., et al., *Modulation of dark conductivity over a 1 x 10(-12) to 1 x 10(-5) S/cm range through ancillary group modification in amorphous solids of ethyne-bridged (porphinato)zinc(II) oligomers.* Chemistry of Materials, 2007. **19**(25): p. 6062-6064.

107. Novotny, L., *Nano-optics - Optical antennas tuned to pitch.* Nature, 2008. **455**(7215): p. 887-887.

108. Muhlschlegel, P., et al., *Resonant optical antennas.* Science, 2005. **308**(5728): p. 1607-1609.

109. Dawber, M., K.M. Rabe, and J.F. Scott, *Physics of thin-film ferroelectric oxides.* Reviews of Modern Physics, 2005. **77**(4): p. 1083.

110. Jones, P.M. and S. Dunn, *Photo-reduction of silver salts on highly heterogeneous lead zirconate titanate.* Nanotechnology, 2007. **18**(18).

111. Scott, J.F., *Device Physics of Ferroelectric Thin-Film Memories.* Jpn. J. Appl. Phys., 1999. **38**: p. 2272.

112. Masel, R.I., *Principles of adsorption and reaction on solid surfaces*. Wiley series in chemical engineering. 1996, New York: Wiley. xiv, 804 p.

113. Bonnell, D.A., et al., *Effect of size dependent interface properties on stability of metal clusters on ceramic substrates.* Acta Materialia, 1998. **46**(7): p. 2263-2270.

114. Sze, S.M. and K.K. Ng, *Physics of semiconductor devices*. 3rd ed. 2007, Hoboken, N.J.: Wiley-Interscience. x, 815 p.

115. Banerjee, P., et al., *Plasmon-Induced Electrical Conduction in Molecular Devices.* ACS Nano, 2010. **4**(2): p. 1019-1025.

116. Ringe, E., et al., *Unraveling the Effects of Size, Composition, and Substrate on the Localized Surface Plasmon Resonance Frequencies of Gold and Silver Nanocubes: A Systematic Single-Particle Approach.* The Journal of Physical Chemistry C, 2010. **114**(29): p. 12511-12516.